DESIGN, FABRICATION, AND MODELING OF FREEFORM OPTICS GENERATED BY DIAMOND TURNING MACHINE

by

Chih-Yu Huang

A Dissertation Submitted to the Faculty of the

COLLEGE OF OPTICAL SCIENCES

In Partial Fulfillment of the Requirements

For the Degree of

DOCTOR OF PHILOSOPHY

In the Graduate College

THE UNIVERSITY OF ARIZONA

2017

THE UNIVERSITY OF ARIZONA
GRADUATE COLLEGE

As members of the Dissertation Committee, we certify that we have read the dissertation prepared by Chih-Yu Huang, titled Design, Fabrication, and Modeling of Freeform Optics Generated by Diamond Turning Machine, and recommend that it be accepted as fulfilling the dissertation requirement for the Degree of Doctor of Philosophy.

_____ Date: 4/11/2017
Rongguang Liang

_____ Date: 4/11/2017
James T Schwiegerling

_____ Date: 4/11/2017
Dae Wook Kim

Final approval and acceptance of this dissertation is contingent upon the candidate's submission of the final copies of the dissertation to the Graduate College.

I hereby certify that I have read this dissertation prepared under my direction and recommend that it be accepted as fulfilling the dissertation requirement.

_____ Date: 4/11/2017
Dissertation Director: Rongguang Liang

STATEMENT BY AUTHOR

This dissertation has been submitted in partial fulfillment of the requirements for an advanced degree at the University of Arizona and is deposited in the University Library to be made available to borrowers under rules of the Library.

Brief quotations from this dissertation are allowable without special permission, provided that an accurate acknowledgement of the source is made. Requests for permission for extended quotation from or reproduction of this manuscript in whole or in part may be granted by the head of the major department or the Dean of the Graduate College when in his or her judgment the proposed use of the material is in the interests of scholarship. In all other instances, however, permission must be obtained from the author.

SIGNED: Chih-Yu Huang

ACKNOWLEDGEMENTS

I would like to express my sincere gratitude to my advisor, Dr. Rongguang Liang, for all his guidance and support during my Ph.D. study. He always provided me with valuable hands-on experiences and opportunities. To me, he is not only a mentor, but also a good friend. I would also like to thank my dissertation committee members Dr. James T Schwiegerling and Dr. Dae Wook Kim for their insightful suggestions and discussion on the dissertation.

Thanks to all the colleagues in the Applied Optics Lab for the discussions on the research projects and help in doing experiments. I would also like to thank Mitch, Chris, and John from Moore Nanotechnology Systems for their useful suggestions and discussions about the challenging programs.

Finally, I would like to express my deepest appreciation to my wife, Kuei-Fan Lin, my parents, Li-Chun Huang and Ho-Ching Lu for their constant support and endless love.

DEDICATION

To my parents, Li-Chun Huang, and Ho-Ching Lu

To my better half, Kuei-Fan Lin

To O-One

I love you all.

TABLE OF CONTENTS

LIST OF FIGURES

LIST OF TABLES

ABSTRACT

Ultra-precision single point diamond turning machine is capable of generating aspherical and freeform surfaces that traditional optical fabrication methods are difficult or impossible to achieve. Having sub-micrometric form accuracy and with surface roughness of only several nanometers, diamond turning fabrication process has become one of the most promising methods for more efficient and high quality optical fabrication of the modern freeform lenses.

Despite its versatility of fabricating freeform surfaces, the characteristic spiral-shape tool marks due to the diamond turning process can cause scattering as well as surface form error, and therefore degrades the optical performance of the surfaces. As a result, a comprehensive study on the diamond turning tool marks is presented and a surface topography model to simulate the diamond turned lens surfaces including flat, spherical, and freeform surfaces is proposed. This model provides a better understanding of the surface topography, and suggests an optimized combination of the cutting parameters to achieve the best surface quality and minimum surface roughness.

In this dissertation, a new technique is proposed with the integration of mechanical mounts onto the lens element to achieve a compact, lightweight, low cost, easy to assemble system that has high imaging quality. Besides, a new fixture design that can help to minimize lens decenter during the diamond turning process is developed and demonstrated. With the utilization of interferometry, surface tilt between the two surfaces of the lens element is corrected and minimized. The design, fabrication, and testing of an ultra-compact endoscope as well as a microscope objective will be presented as a proof of concept. The preliminary assembly and testing results of the two systems conclude that the proposed technique is promising in getting a self-aligned and self-assembled lens system with high imaging quality.

Finally, a thorough analysis on the tool path generation, fabrication method, and modeling of a diamond turned circular blazed grating will be presented. A model on the diamond turned blazed grating profile has been developed with the consideration of basic cutting parameters as well as diamond tool tilt. The diffraction efficiency calculation with respect to diamond tool tilt will also be provided, and a guidance will be given on the optimal fabrication method for blazed gratings with highest diffraction efficiency.

CHAPTER 1 INTRODUCTION

The rapid development of advanced optical design techniques and software has led to requests for more efficient and versatile optical fabrication methods. Single point diamond turning machine is one of the solutions to fabricate spherical and freeform surfaces with sub-micrometric form accuracy and only several nanometers surface roughness [1]. It is capable of generating complex surfaces to an optical quality without post-polishing process. Besides, with the high resolution and straightness of the machine axes, we can also have a very accurate control of the other specifications of the lens such as lens thickness, lens diameter, lens decenter and tilt. It is therefore advantageous to utilize these ultra-precision characteristics of the diamond turning machine to fabricate complex lens systems for high imaging quality and fast prototyping. In addition, using diamond turning machine to fabricate metallic mold for glass or plastics molding is favorable when direct diamond-turning of lenses is not possible or mass production is needed.

1.1 Introduction to diamond turning fabrication process

Diamond turning is a fabrication process that uses diamond with controlled radius as the cutting tool to cut the workpiece that is held on the spindle. Figure 1.1 shows the four-axis diamond turning machine 350 FG from Moore Nanotechnology Systems. These four axes consist of the translation stages X, Y, and Z axis, and the rotational axis C axis. The schematic representation of the four-axis diamond turning machine 350 FG is shown in Figure 1.2 [2]. Figure 1.3 gives the detailed specifications of the 350 FG [2]. By the precise computer numerical control (CNC) of the translation stages, diamond turning machine is able to generate rotationally symmetric surfaces including spherical, aspheric, and circular gratings. If we further allow the simultaneous control of the translation stages and the spindle C axis, we can fabricate freeform surfaces. This is done by

giving the diamond turning machine a series of input that includes the X, Z, and C coordinates. The diamond tool will move in and out in Z direction in accordance with the freeform surface profile at each C coordinate in each spindle revolution while the translation stage moves steadily in X direction according to the input feed rate.

Figure 1.1 Four-axis diamond turning machine 350 FG from Moore Nanotechnology Systems.

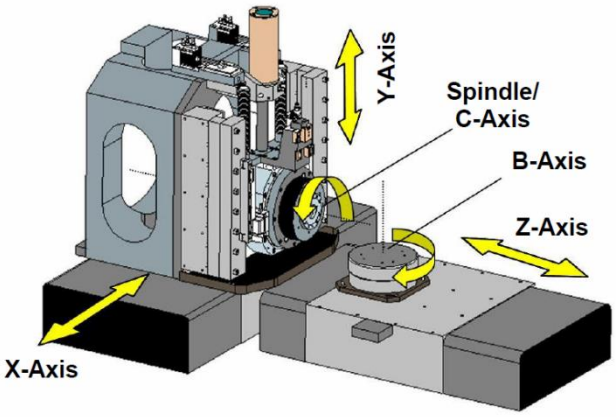

Figure 1.2 Schematic representation of the four-axis diamond turning machine 350 FG [2].

Linear Axes	X	Z	Y (Vertical)
Type	Fully constrained oil hydrostatic, box way slide	Fully constrained oil hydrostatic, box way slide	Fully constrained oil hydrostatic box way slide with adaptively controlled air bearing counterbalance to negate gravitational forces & varying workpiece loads.
Travel	350mm (14")	300mm (12")	150mm (6")
Drive System	Brushless DC Linear Motor	Brushless DC Linear Motor	Dual Brushless DC Linear Motor
Feedback Type	Laser holographic linear scale (athermally mounted)	Laser holographic linear scale (athermally mounted)	Laser holographic linear scale (athermally mounted)
Feedback Resolution	0.034 nanometer	0.034 nanometer	0.034 nanometer
Feed Rate (maximum)	2000mm/min	2000mm/min	2000mm/min
Straightness in critical direction	0.3µm (12µ") over full travel	0.3µm (12µ") over full travel	0.5µm (20µ") over full travel / 0.3µm (central 100mm)
Hydrostatic Oil Supply	Compact, low flow, low pressure system with closed loop servo control and pressure accumulator to minimize pump pulsation.		

Optional Rotational Axes	B	C
Type	Oil Hydrostatic	Groove Compensated Air Bearing (liquid cooled)
Travel	360° (Bi-directional)	360° (Bi-directional)
Drive System	Brushless DC motor	Brushless DC motor
Axial Stiffness	875 N/µm (5,000,000 lbs./in.)	See **Workholding Spindle** Specifications Listed Above
Radial Stiffness (at nose)	260 N/µm (1,500,000 lbs./in.)	See **Workholding Spindle** Specifications Listed Above
Positioning Accuracy	± 1.0 arc seconds (compensated)	± 1.0 arc seconds (compensated)
Feedback Resolution	0.02 arc seconds	0.07 arc seconds
Maximum Speed (Positioning Mode)	50 rpm	3,000 rpm
Motion Accuracy	Axial: ≤ 0.1µm (4µ") Radial: ≤ 0.1µm (4µ")	Axial: ≤ 12.5 nm (0.5µ") Radial: ≤ 12.5 nm (0.5µ")

Figure 1.3 Specifications of the diamond turning machine 350 FG from Nanotech [2].

Before we can fabricate a high quality lens surface with minimum form error, it is important that we align the diamond tool to the center of the spindle. The complete flow chart for the alignment process of the diamond tool is shown in Figure 1.4. First, we need to choose a diamond tool with proper radius of curvature that is appropriate to the specific application. Then we use the camera hung on the Y axis of the diamond turning machine to roughly align the diamond tool. This is done by finding at least three points on the diamond tool profile and do the curve fitting to find the center of curvature of the diamond tool. Once we finish the rough alignment, we conduct a test cut of a spherical surface on a high precision copper standard stud. Then we measure the surface by the interferometer and calculate the surface form error. If the form error is not within the tolerance, we need to fine adjust the diamond tool position and re-cut the spherical surface. This procedure is done iteratively until the surface form error is within tolerance. Then the diamond tool is well-aligned.

In reality, this alignment is only good for cutting a surface with the same spherical surface and the same height as the standard stud because the axes are not perfectly straight and perfectly perpendicular to each other. As a result, this alignment serves as a starting point, and we need to repeat this procedure for every lens surface to make sure their form errors are all within tolerance.

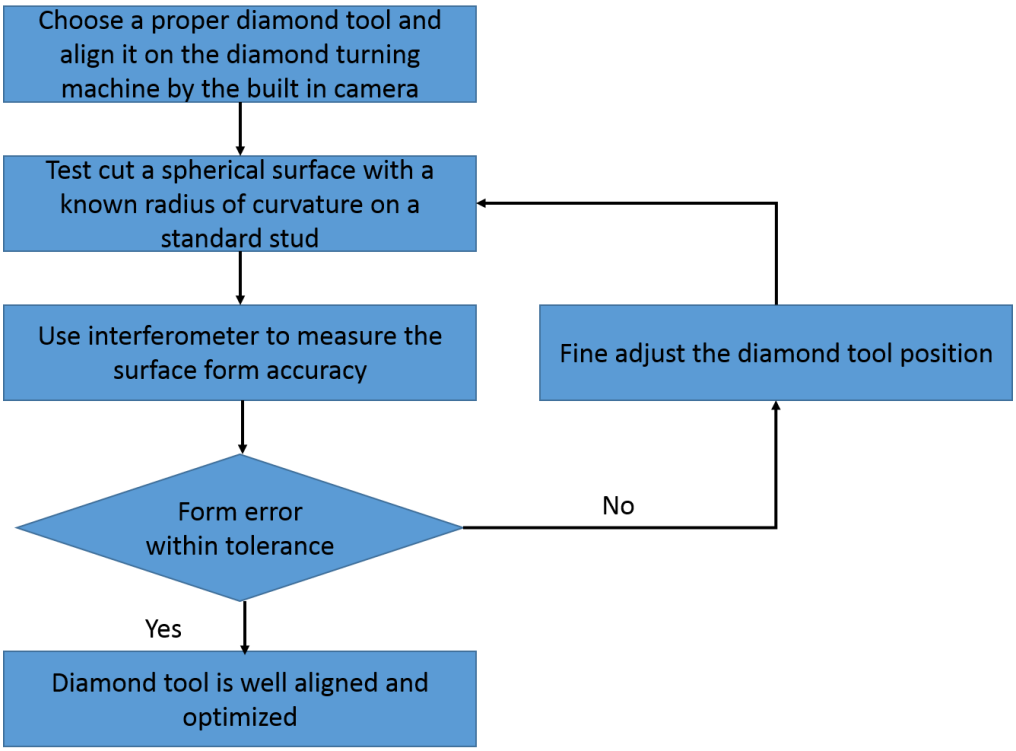

Figure 1.4 Flow chart for the alignment process of the diamond tool.

1.2 Applications of diamond turning fabrication

In this section, we will give some examples of the optical systems that are particularly generated by the diamond turning process. These systems have the characteristic of compact, lightweight, and having complicated lens surfaces or structures, such as having freeform surfaces or combining multiple lens surfaces on one lens element.

Freeform surface is any non-rotationally symmetric surface. It has several advantages over the traditional rotationally symmetric surfaces. First, freeform surfaces can provide more degrees of freedom and allow optical designers to have more flexibility for innovate optical design. Second, it can greatly enhance the optical system performance. For instance, freeform optics enable optical performance otherwise impossible, such as simultaneously correcting aberrations, increasing depth of field, and expanding field of view. Third, freeform optics can simplify system structure with fewer surfaces, lower mass, lower cost, smaller package size and less stray light. Finally, it can realize system integration easily, and reduce the difficulty in assembly. For example, multiple optical surfaces can be made on one freeform element.

As the first example, we designed and fabricated a triangular beam shaper with a large depth of field by employing two freeform lenses [3]. The sketch of the double freeform lens pair and the completed freeform lenses by the diamond turning fabrication process are shown in Figure 1.5. Figure 1.6 presents the experimental results of the propagation of the beam profile from the Gaussian input to the triangular flattop output at different distance. By the combination of two freeform lenses, it is possible to design a flattop generator with nontraditional geometry.

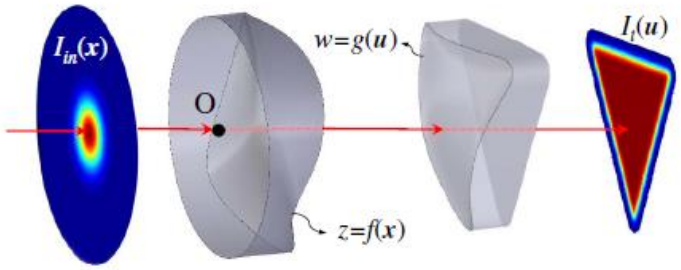

(a)

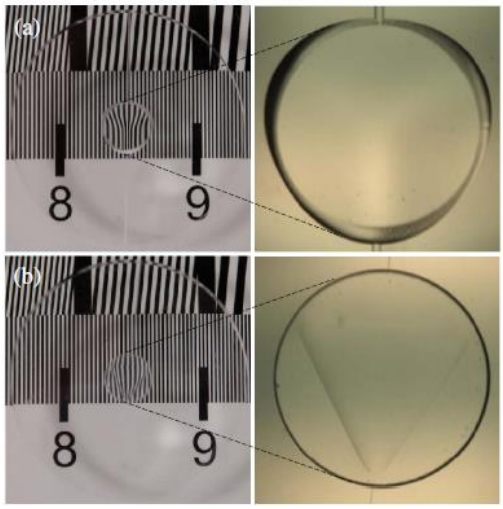

(b)

Figure 1.5 (a) Sketch of the double freeform lens pair for triangular beam shaping, and (b) diamond turned double freeform lens pair [3].

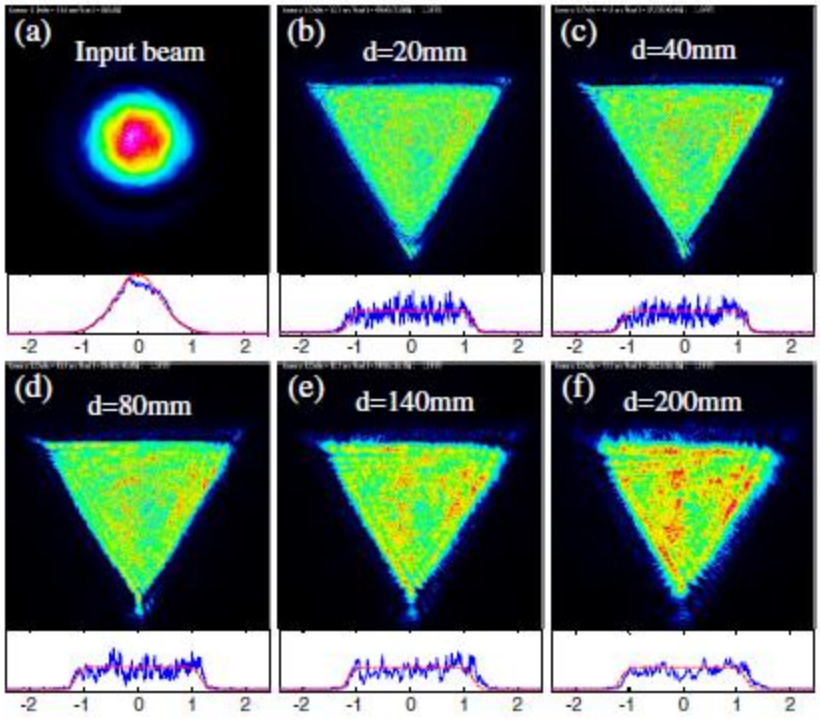

Figure 1.6 Experimental results of the propagation of the beam profile from the Gaussian input to the triangular flattop output at different distance [3].

For the second example, we designed, fabricated, and tested a dual-view endoscope for colon inspection [4]. This endoscope has a forward view and a backward view without field obscuration. Figure 1.7 shows the dual-view endoscope that can illuminate and image both the forward and backward views. Figure 1.8 shows the system configuration of the endoscope. We can see that forward view and backward view share the same lens components, and the freeform lens 1 is the only lens used to combine both forward and backward views. This can greatly reduce the weight and size of the endoscope, which is very crucial in making compact biomedical optics.

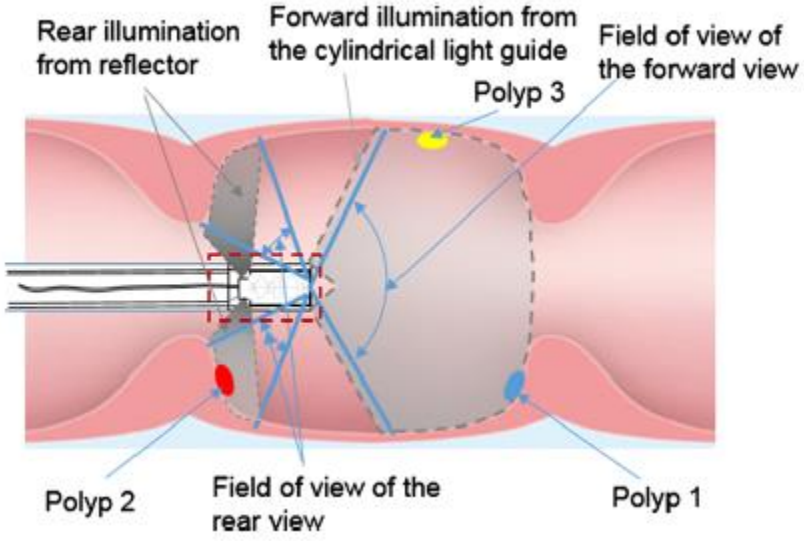

Figure 1.7 Endoscope that has both forward and backward views [4].

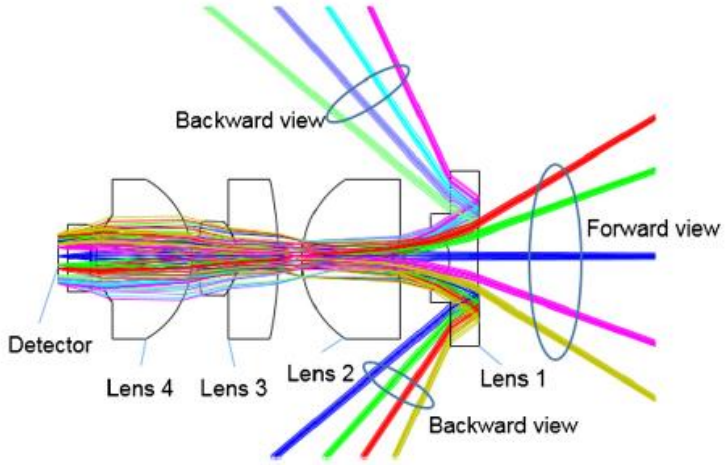

(a)

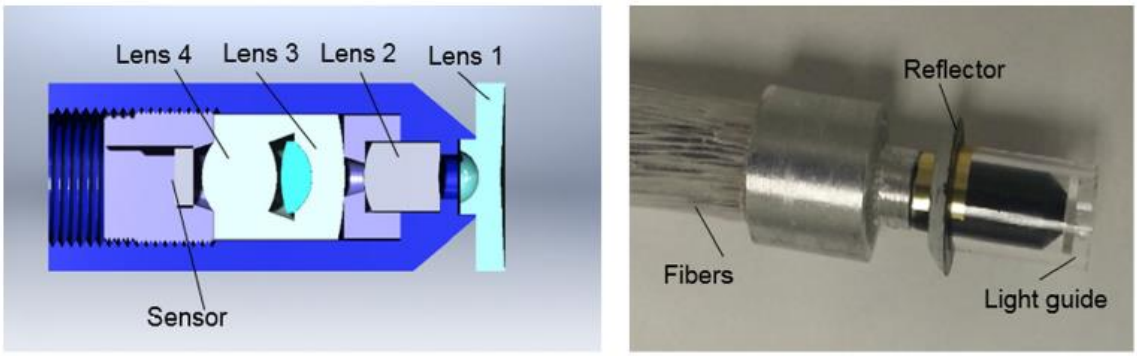

(b)

Figure 1.8 (a) System configuration of the dual-view endoscope, and (b) prototype of the dual-view endoscope [4].

1.3 Disadvantages of diamond turning fabrication

Although the diamond turning process can generate high-precision optical quality surfaces, there are always inevitable spiral shape tool marks on the finished surface. Figure 1.9 gives an example of the tool marks on a flat surface generated by the diamond turning process. These mid-spatial frequency components can cause scattering on the surface and degrade optical performance

of the system [5, 6]. Several physical models have been proposed to study the factors that influence surface roughness of the diamond turned flat surfaces [7-9]. Most of their models are based on the Fourier decomposition. In this dissertation, however, we propose a more realistic model by considering the inherent spiral-shape tool marks from the diamond turning process and the relative tool-workpiece vibrations.

Since most of the models are limited to describing a diamond turned flat surface, and there is a lack of a more general model on the surface topography of curved or freeform surfaces, we extend the proposed model to simulate surface topography of diamond turned spherical and freeform surfaces by considering the basic cutting parameters, relative vibrations between the workpiece and diamond tool, and also the constant changing contact point of the diamond tool and the local workpiece surface which is specific to a curved surface.

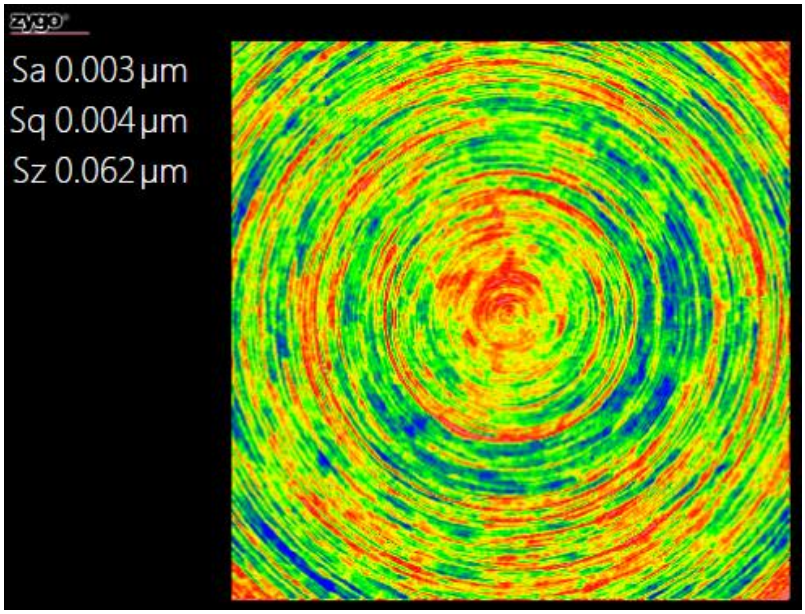

Figure 1.9 Tool marks on a flat surface generated by the diamond turning process.

1.4 Dissertation overview

This dissertation provides a detailed discussion about the design, fabrication, and modeling of freeform optics generated by diamond turning machine. In Chapter 2, we describe and propose a model for diamond turned flat surfaces. In Chapter 3, we further expand the model to analyze diamond turned spherical as well as freeform surfaces. Chapter 4 presents a technique which integrates mechanical mounts onto the lens surfaces to provide a self-aligned and self-assembled lens system. In Chapter 5, we have a detailed discussion about the fabrication method for circular blazed gratings, which includes tool path generation, grating surface profile modeling, and diffraction efficiency calculation and analysis. Finally, the conclusion and future work are given in Chapter 6.

CHAPTER 2 MODELING OF SURFACE TOPOGRAPHY ON DIAMOND TURNED FLAT SURFACES

Surface roughness is an important factor in characterizing the performance of high precision optical surfaces. In this chapter, we propose a model to estimate the surface roughness generated by single point diamond turning machine. In the model, we take into consideration the basic tool cutting parameters as well as the relative vibration between the tool and the workpiece in both infeed and feeding directions. Current models focus on the relative tool-workpiece vibration in the infeed direction. However, based on our experimental measurements, the contribution of relative tool-workpiece vibration in the feeding direction is significant and cannot be ignored in the model. The proposed model is able to describe the surface topography for flat surface as well as cylindrical surface of the workpiece. Our experimental study with metal materials shows good correlation between the model and the diamond-turned surfaces.

2.1 Three-dimensional surface topography model for flat surface

Under ideal condition, the two-dimensional surface profile of the diamond-turned surface along the radial direction can be viewed as repeated tool profiles at intervals of feed distance per spindle revolution (mm/rev). Thus the three-dimensional surface topography can be modeled based on the azimuthal progression of the two-dimensional surface profile. Figures 2.1(a) and (b) show the ideal two-dimensional and three-dimensional surface topography of a diamond-turned flat surface, respectively. In Figure 2.1(a), red curves represent diamond tool profile, and black curves show the resulting surface topography on the surface. With this ideal assumption, we can derive the maximum peak-to-valley height R_t as [10]

$$R_t = \frac{f^2}{8R} \qquad (2.1)$$

and the arithmetic roughness R_a is

$$R_a \approx \frac{0.032 f^2}{R} \qquad (2.2)$$

where f is feed rate (mm/rev) and R is the tool radius (mm).

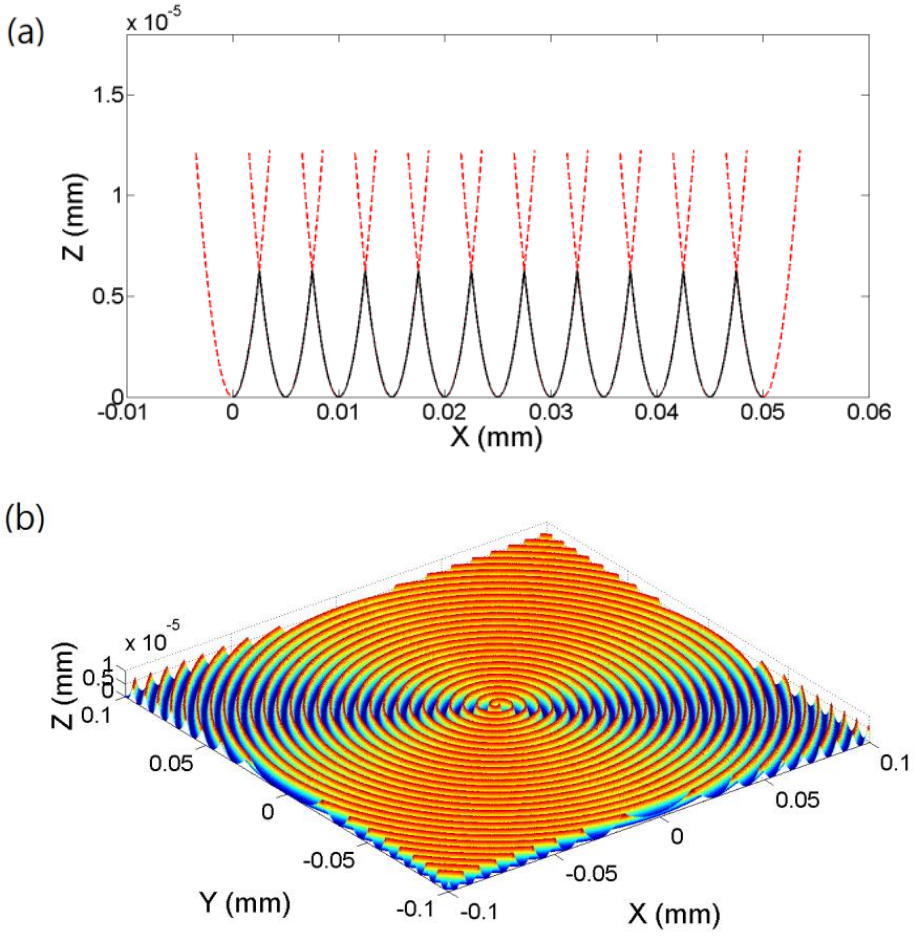

Figure 2.1 (a) Ideal two-dimensional and (b) three-dimensional surface topography of a diamond-turned flat surface.

However, during actual cutting process, several factors can influence the surface roughness, such as the vibration between the diamond tool and workpiece, the misalignment between the diamond tool tip and the spindle center, thermal variation, air nozzle direction, cutting fluids, etc. The misalignment between the tool tip and the spindle center can cause a local high point at the center of the workpiece as well as form error for the whole surface. Depending on whether the tool tip is higher or lower than the spindle center, the local high point at the workpiece center can either be a cone or a rod. These situations are shown in Figure 2.2. In Figure 2.2, the central high points are greatly enlarged for clearer demonstration, and the typical sizes for these cones or rods due to the misalignment are about 10 um in diameter and 1 um in height. On the other hand, if the tool pasts the spindle center in the feeding direction, the resulting surface will be deformed to W-shape if we are cutting a convex surface; when the tool is not yet to the center in the feeding direction, the profile of the fabricated convex surface will be M-shape. The result is opposite when we are fabricating a concave surface. Figure 2.3 gives a summary of the two conditions for the form error caused by the tool misalignment in X direction [2]. Using interferometric technique, this misalignment issue can be well corrected. Thermal variation, air nozzle direction, and cutting fluids can be thought of as environmental factors, and are not the main focus of this paper.

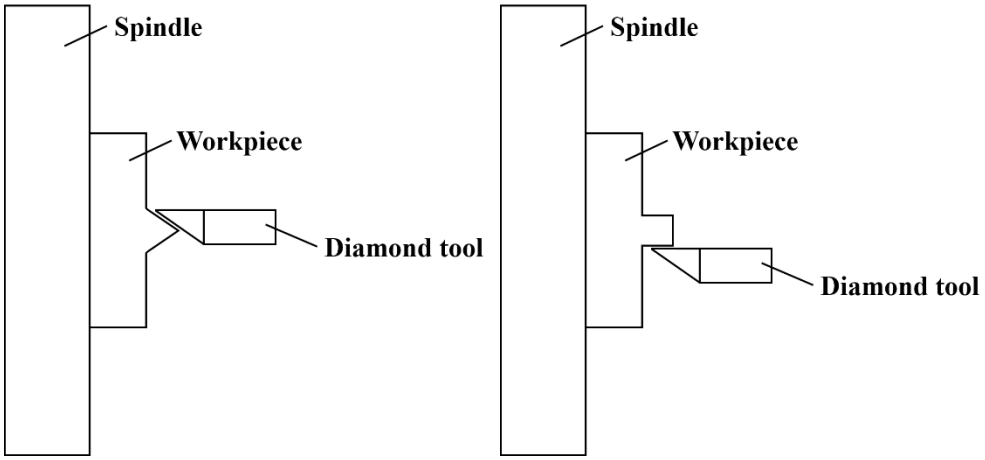

(a) (b)

Figure 2.2 Schematic representation of the diamond tool misalignment in Y direction. (a) Tool is higher than the spindle center, and (b) tool is lower than the spindle center.

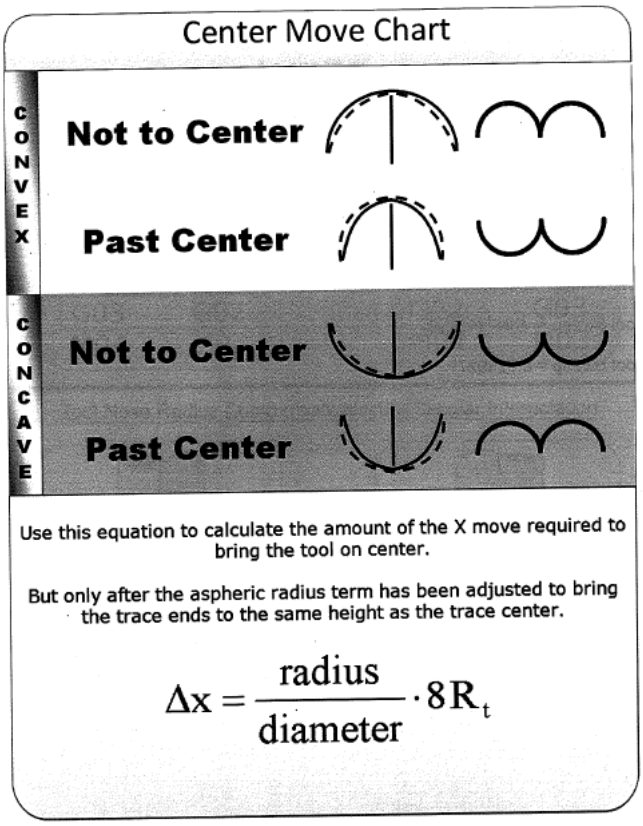

Figure 2.3 Schematic representation of the diamond tool misalignment in X direction [2].

The vibration between diamond tool and workpiece is one of the most important factors influencing the surface roughness generation. Several researchers have explored the influences of tool-workpiece vibration in CNC turning and diamond turning [11-19]. Some of their models are based on the relative vibration between the diamond tool and the workpiece in the infeed direction [12, 13], or the vibration in the cutting direction [14]. However, based on our experimental findings, there is also significant relative tool-workpiece vibration in the feeding direction. Although this vibration is not as evident in modeling flat surfaces, it is equally important to the vibration in the infeed direction when considering curved surfaces and it becomes dominant when describing vertical cylindrical side edge of the workpiece. Without considering this relative tool-workpiece vibration in the feeding direction, it is insufficient to model curved surfaces. As a result, we propose a more general model based on these two vibrations and other basic cutting parameters to describe the surface topography of the flat surface as well as cylindrical surface of the workpiece. Figure 2.4 gives a schematic representation of the diamond turning process. It also shows the relative vibrations between the tool and workpiece in both infeed and feeding directions, which are in the Z and X directions, respectively. We assume these two vibrations to be simple harmonic motions (SHM). This gives us a relatively simple model to build but can however provide the most useful information from the diamond turning process.

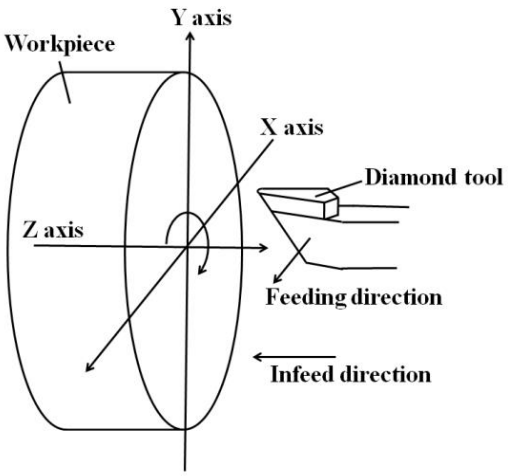

Figure 2.4 Schematic representation of the diamond turning process.

Before calculating the two-dimensional surface profile on the flat surface, we need to first locate the tool tip locations along the radial direction in each revolution. The simple harmonic motion in Z and X directions can be described respectively as

$$Z_{SHM}(i,k) = A_z sin\{2\pi f_z t - \varphi_z\} \qquad (2.3)$$

$$X_{SHM}(i,k) = A_x sin\{2\pi f_x t - \varphi_x\} \qquad (2.4)$$

where A_z and A_x are the amplitudes of vibration in each direction, f_z and f_x are the frequencies of the vibration in each direction. The phase φ_z and φ_x are the phase shifts for the vibration in each direction. When we consider the radial progression of the tool from the edge of the workpiece, $-R_0$, to the center, we can acquire the positions of the tool tip in Z and X directions respectively as

$$z_t(i,k) = A_z sin\left\{2\pi f_z \frac{[k+(i-1)N_\theta]\Delta\theta}{\omega} - \varphi_z\right\} \qquad (2.5)$$

$$r_t(i,k) = -R_0 + [k+(i-1)N_\theta]\Delta R + A_x sin\left\{2\pi f_x \frac{[k+(i-1)N_\theta]\Delta\theta}{\omega} - \varphi_x\right\} \qquad (2.6)$$

for k=1,2,…N_θ and i=1,2,…N. $\Delta\theta$ is the angular resolution, N_θ the total number of sections around the circle, $N_\theta = 2\pi/\Delta\theta$, ω the angular speed (rad/s), R_0 the radius of the workpiece, and $N = R_0/f$ is the total number of tool tip points along the radius of the workpiece. Figure 2.5 shows a sample tool tip locus for k=0, the black curve shows the influence of relative vibration in the infeed direction only and the red curve considers the vibrations in both infeed and feeding directions. In Figure 2.5, we purposely exaggerate the amplitude of vibration in the feeding direction to have a clearer comparison between the two curves. Here we use f_x=33.34 Hz, f_z=90.27 Hz, A_x=50um, A_z=2.5nm, andω=209.44 rad/s for the simulation.

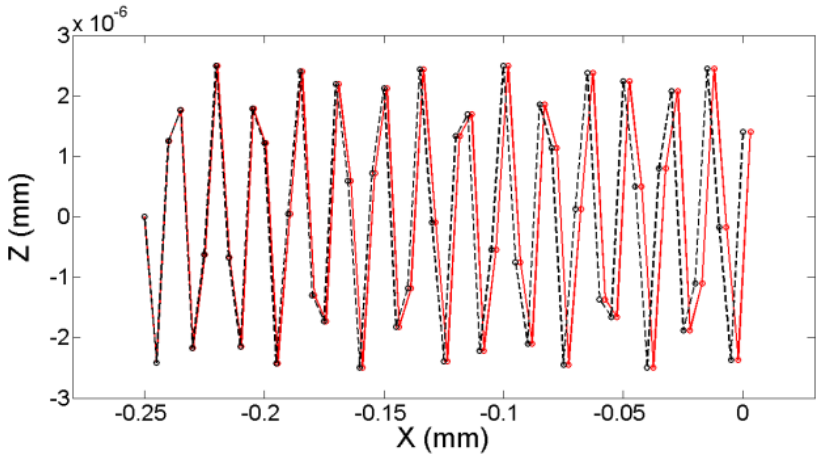

Figure 2.5 Tool tip locus for k=0. Black curve shows the influence of relative vibration in the infeed direction only and the red curve considers the vibrations in both infeed and feeding directions.

Now that we have the tool tip locus along the radial section, we can acquire the two-dimensional surface topography by adding the diamond tool profile onto each tool tip location. Since the typical depth of cut is greatly smaller than the tool radius, we can use parabolic approximation to describe the tool profile, as in Equation 2.7

$$z \approx z_t(i,k) + \frac{\left(x - r_t(i,k)\right)^2}{2R} \qquad (2.7)$$

The point where the tool profile intercepts with its neighboring tool profile shows the upper limit of the surface topography. At this interception point, $x_t(i,k)$, the location of the tool profile on ith tool tip is equal to the location of the tool profile on the i+1th tool tip,

$$z_t(i,k) + \frac{[x_t(i,k) - r_t(i,k)]^2}{2R} = z_t(i+1,k) + \frac{[x_t(i,k) - r_t(i+1,k)]^2}{2R} \qquad (2.8)$$

where k=1,2,…N_θ and i=1,2,…N-1. Assume $\varphi_x = 0$ and $\varphi_z = 0$ for simplicity, we can solve Equation 2.8 and get all the interception points along the radial direction:

$$x_t(i,k) = \frac{2RA_z cos[C_z(2k + (2i-1)N_\theta)]sin(C_z N_\theta)}{N_\theta \Delta R + 2A_x cos[C_x(2k + (2i-1)N_\theta)]sin(C_x N_\theta)} + \frac{[2k + (2i-1)N_\theta]\Delta R - 2R_0}{2} + A_x sin[C_x(2k + (2i-1)N_\theta)]cos(C_x N_\theta) \qquad (2.9)$$

where k=1,2,…N_θ and i=1,2,…N-1, $C_x = \pi f_x \Delta\theta/\omega$ and $C_z = \pi f_z \Delta\theta/\omega$ are constants.

By using Equations 2.5 to 2.9, we can get a two-dimensional surface roughness profile along radial direction for a specific k section. Figure 2.6 shows the two-dimensional surface roughness profile along radial direction for k=0. Considering all sections around the circle for k=1, 2,…, N_θ, we can acquire the three-dimensional surface topography of the diamond-turned flat surface, as shown in Figure 2.7.

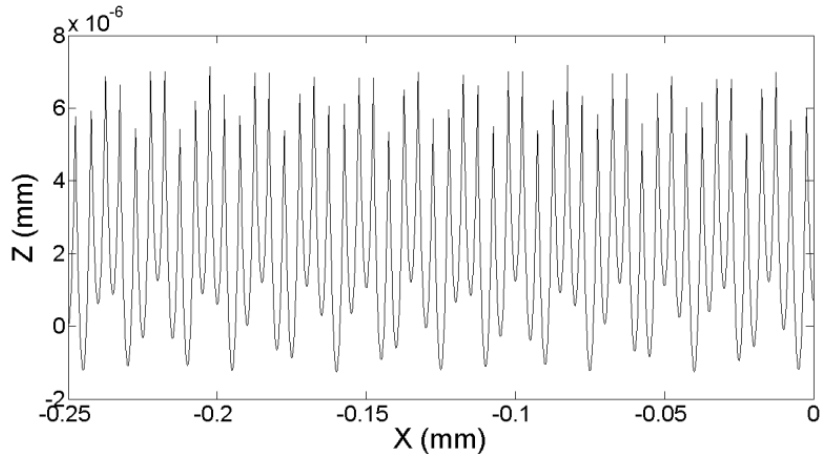

Figure 2.6 Two-dimensional surface roughness profile along radial direction for k=0.

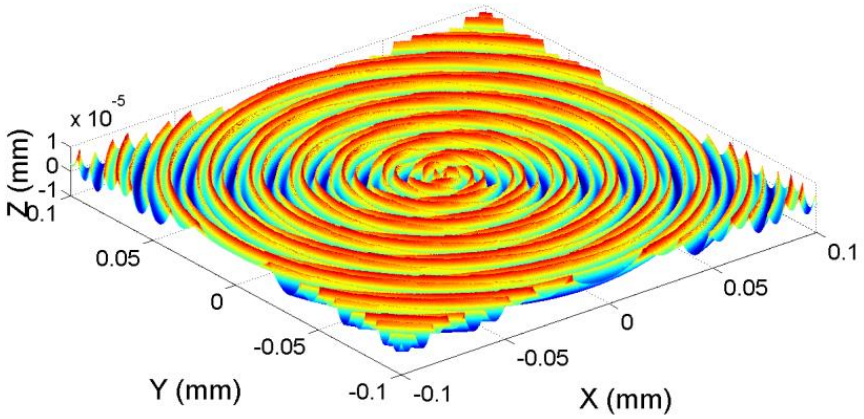

Figure 2.7 Three-dimensional surface topography of the flat surface of the workpiece.

2.2 Three-dimensional surface topography model for cylindrical surface

We can further extend this model to describe surfaces other than flat by introducing coordinate system rotation to the vibrations in Equations 2.3 and 2.4 in order to redistribute these two vibrations to the new reference axes. This procedure is necessary since during diamond turning process, the actual cutting point on the diamond tool is changing constantly based on the local shape of the workpiece it is cutting, and the diamond tool is always cutting the local surface of the

workpiece perpendicularly. As a result, the contributions of the two vibrations in the ineed and feeding directions are different along a curved surface. Equation 2.10 shows the coordinate rotation matrix, where α is the angle of rotation from the X axis. For each tool tip location on the radial profile of the surface that is to be fabricated, α can be derived from the slope at that point. Once we know the angle α and thus the new sets of amplitude of vibration in the X and Z directions, we can add tool profile onto each tool tip point and find the interception points between two neighboring tool profiles. The process is similar to Equations 2.5 to 2.9 except there are two vibration terms with different amplitudes and frequencies in both the new $X'$and Z'axes. Figure 2.8 gives an example of the tool tip locus on a spherical surface with radius of curvature of 0.5mm, f_x=47 Hz, f_z=70 Hz, A_x=5um, and A_z=5um. The amplitude and frequency of both vibrations are purposely exaggerated to have a clearer demonstration. In Figure 2.8(a), we only consider the vibration in the infeed direction, and the contribution of this vibration continuously decreases when we go from center to the outer edge of the spherical surface. This is because when we are at or near the center, the vibration in the infeed direction acts nearly perpendicularly on the surface, but once we are away from the center and being close to the edge of the surface, this vibration becomes essentially parallel to the surface, and the influence is less significant. On the other hand, when we consider the vibrations in both infeed and feeding directions, as in Figure 2.8(b), the contribution of these two vibrations act consistently throughout the whole spherical surface. As a result, it is sufficient to model curved surfaces when we take into consideration both the relative tool-workpiece vibrations in the infeed and feeding directions. Further derivation of the equations for a curved surface is out of scope of this paper and will be discussed separately. In this paper, we will consider a special situation when α equals to 90°, the description of surface topography changes from a flat surface to a cylindrical surface of the workpiece. In such case, we are cutting the vertical

side edges of the workpiece, and the contributions of the two vibrations are interchanged. The set of equations that characterize the surface topography are essentially the same as Equations 2.5 to 2.9 except the value of A_x is interchanged with A_z, and f_x is interchanged with f_z. With these modifications, we can acquire the three-dimensional surface topography of the diamond-turned cylindrical surface of the workpiece, as shown in Figure 2.9.

$$\begin{bmatrix} X_{SHM}{}' \\ Z_{SHM}{}' \end{bmatrix} = \begin{bmatrix} cos\alpha & -sin\alpha \\ sin\alpha & cos\alpha \end{bmatrix} \begin{bmatrix} X_{SHM} \\ Z_{SHM} \end{bmatrix} \qquad (2.10)$$

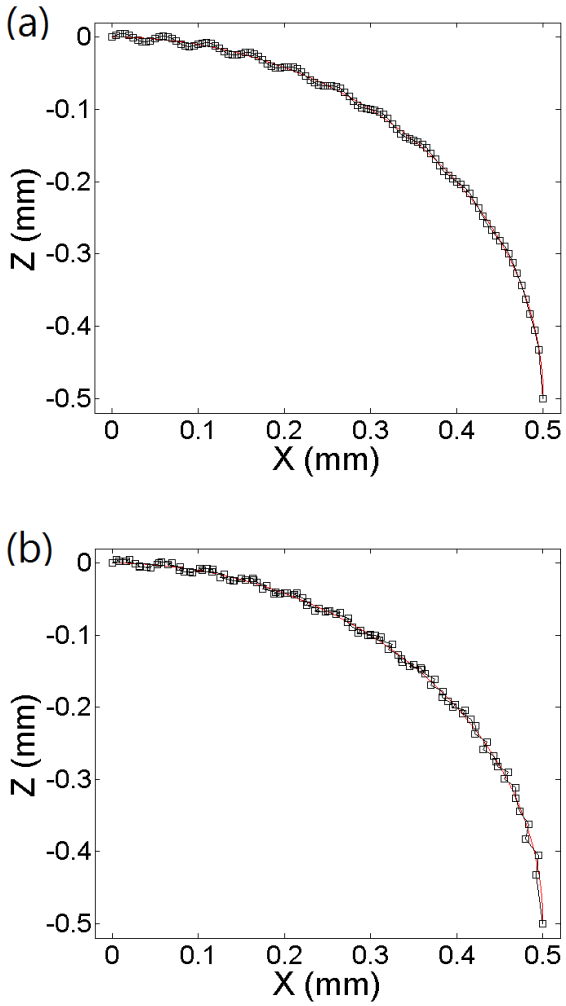

Figure 2.8 Tool tip locus on a spherical surface with relative tool-workpiece vibration (a) in infeed direction only and (b) in both infeed and feeding directions.

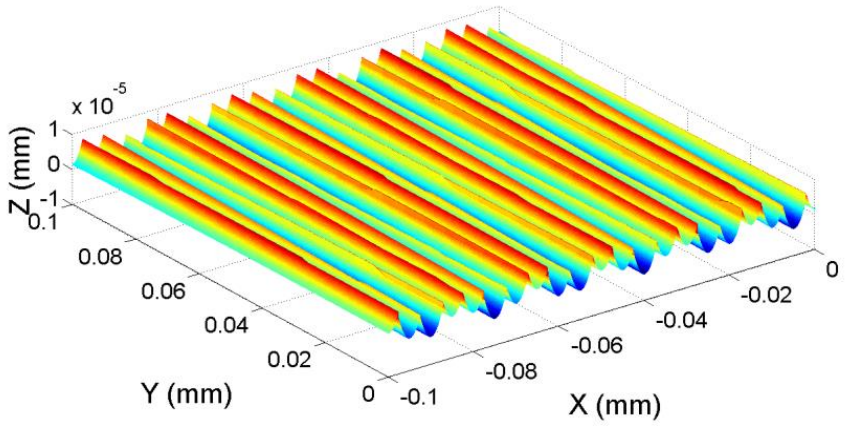

Figure 2.9 Three-dimensional surface topography of the cylindrical surface of the workpiece.

Since the ultimate purpose of this model is to aid optical designers in system design and optimization, it is more preferable to convert polar coordinate description to Cartesian coordinate system by mapping these sample points to rectangular grids. We use the built-in function scatteredinterpolant from Matlab to do the mapping and interpolation. With this conversion, the sample points of the surface topography can now be easily added to the corresponding locations of the lens surface, and we can use this new surface for further analysis and optimization.

Figure 2.10 gives an example on how this method is performed to an optical surface. Here we are interested in the surface topography of a diamond-turned cylindrical surface with the radius of curvature of 6.5mm. Figure 2.10(a) shows a small portion of the perfect cylindrical surface of the lens, and Figure 2.10(b) shows the same portion of the cylindrical surface after diamond turning process. We can see that in Figure 2.10(b) the surface becomes rougher than in Figure 2.10(a). Here again we purposely exaggerate the amplitude of vibration in order to have a clearer demonstration.

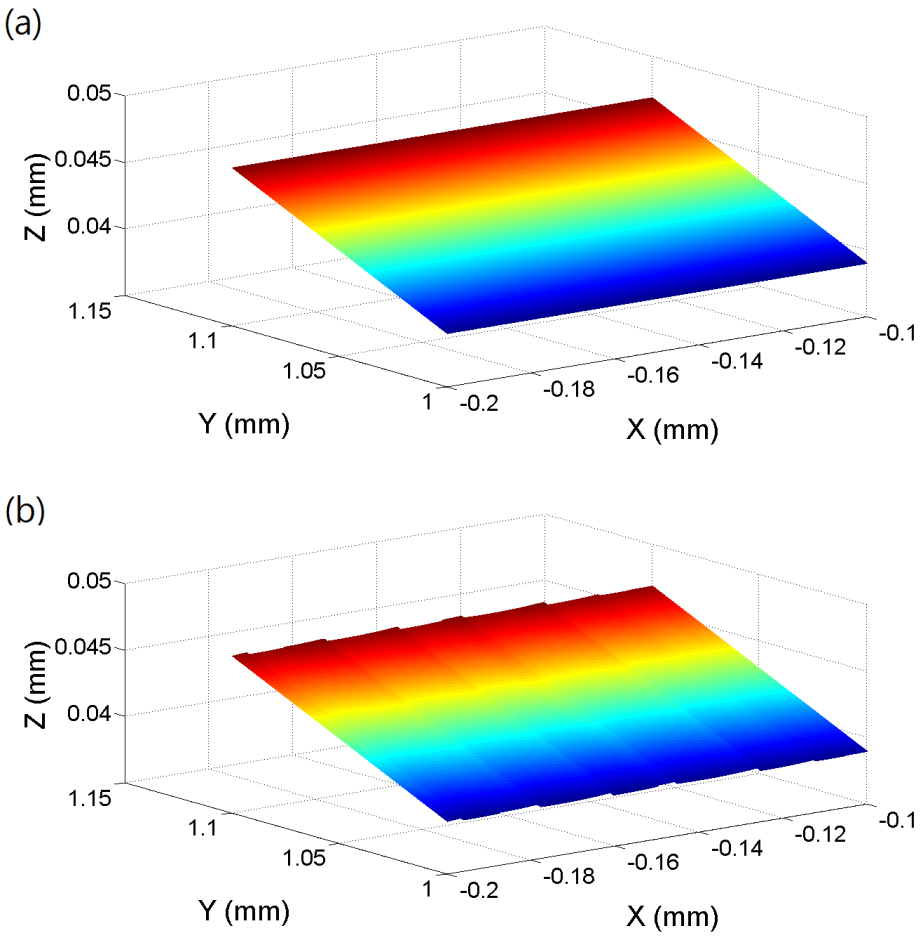

Figure 2.10 A small portion of the three-dimensional surface topography of (a) the perfect cylindrical surface, and (b) cylindrical surface after diamond turning process.

Once we have acquired the three-dimensional surface topography, it is straightforward to calculate the arithmetic average surface roughness R_a, root mean squared surface roughness R_q, and maximum height (peak to valley) of the surface profile R_t. Equations 2.11 to 2.13 show the formula for each parameter described above.

$$R_a = \frac{1}{n}\sum_{i=1}^{n}|z_i| \qquad (2.11)$$

$$R_q = \sqrt{\frac{1}{n}\sum_{i=1}^{n} z_i^2} \qquad (2.12)$$

$$R_t = \max_i z_i - \min_i z_i \qquad (2.13)$$

2.3 Experimental verification

To verify the proposed model, we carry out a series of experiments by cutting metal flat mirror surfaces as well as cylindrical surfaces. The experiments can be divided into two groups. Group I analyzes the relationship between feed rate and surface roughness by changing the feed rate from 2mm/min to 15mm/min while keeping other cutting parameters constant. Group II includes four cylindrical surface cutting tests to verify the surface topography obtained in the previous section. All of the cutting experiments are conducted on the four-axis single point diamond turning machine 350FG from Nanotech. Table 2.1 summarizes the cutting parameters for the two groups. In Group I, we test four different metal materials, namely, C64200, CuSN8, RSA6061, and RSA905. In Group II, we use RSA6061. The three-dimensional surface topography and the surface roughness parameters are measured by a Veeco NT 9800 optical profiler.

Table 2.1 Cutting parameters for the two groups.

Group	Spindle speed (RPM)	Feed rate (mm/min)	Depth of cut (um)	Tool Radius (mm)
I	2000	2	2	0.5
I	2000	5	2	0.5
I	2000	10	2	0.5
I	2000	15	2	0.5
II	2000	5	2	0.5

The relative tool-workpiece vibrations in both the infeed and feeding directions are measured by the program PEWIN provided with the diamond turning machine, and the measurement results are shown in Figure 2.11. Figure 2.11(a) shows the relative tool-workpiece vibration in the infeed direction, and Figure 2.11(c) shows its spectral plot. Similarly, Figure 2.11(b) shows the relative tool-workpiece vibration in the feeding direction, and Figure 2.11(d) shows its spectral plot. We can observe that a dominant mode of vibration with an average magnitude of about 1nm and a frequency of 90.27 Hz occurred in the infeed direction, and a dominant mode of vibration with an average magnitude of about 2nm and a frequency of 33.34 Hz occurred in the feeding direction. Although there are also several weaker modes of vibration in the measurements, we ignore those vibration modes for now and only consider the dominant mode in our present model. Another important observation is that the magnitude of vibration in the feeding direction is about two times the magnitude of vibration in the infeed direction and with an apparently different frequency of vibration. This confirms the necessity of including two sets of vibration in our model.

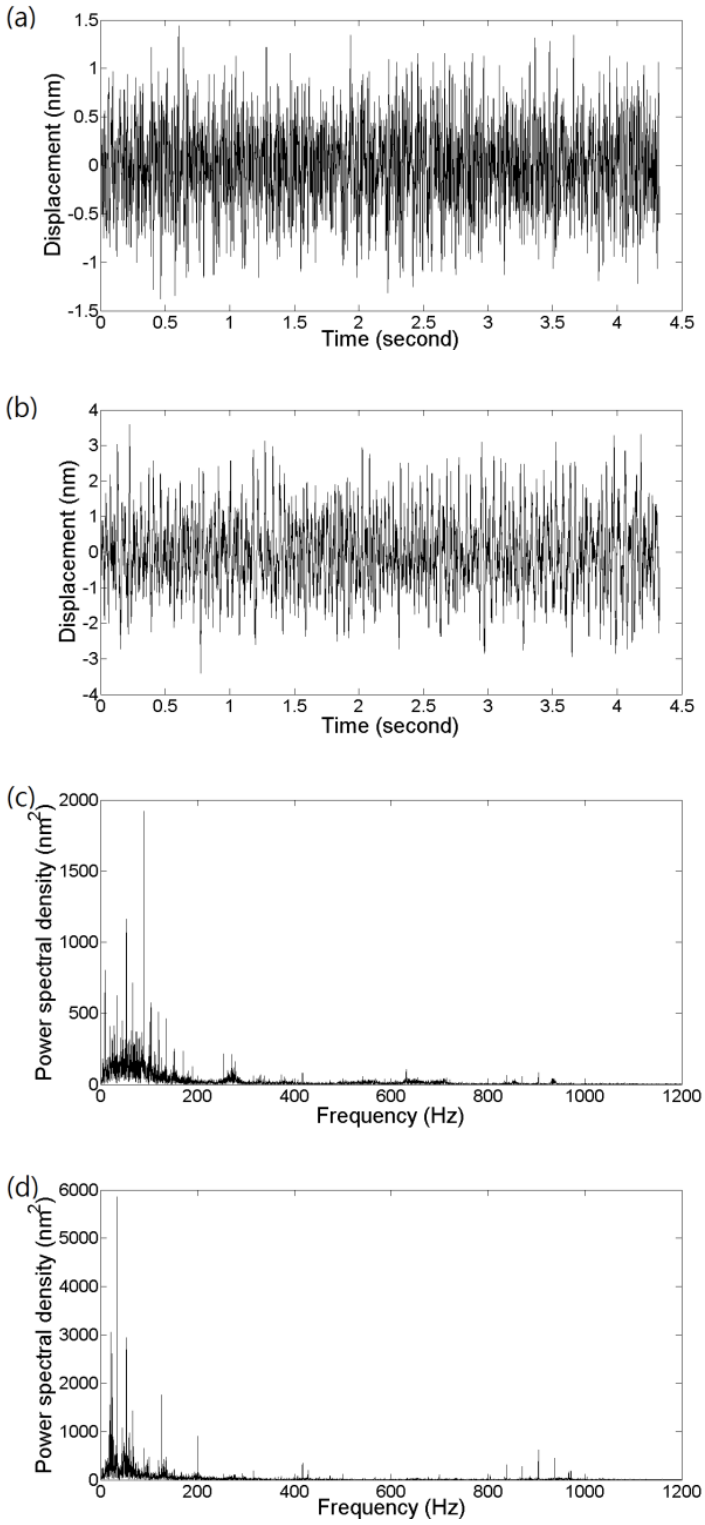

Figure 2.11 Relative tool-workpiece vibration in (a) infeed direction and (b) feeding direction, and its spectral plot in (c) infeed direction and (d) feeding direction.

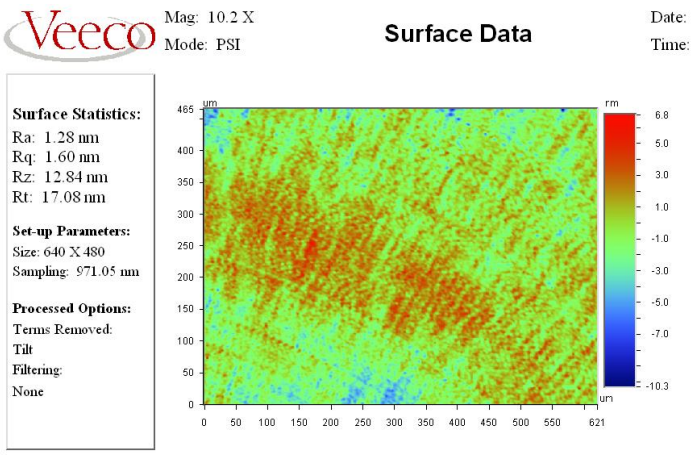

Figure 2.12 Measurement result of the RSA6061 flat mirror surface.

Figure 2.12 shows one of the measurement results of the diamond-turned RSA6061 flat mirror surface from the Veeco NT 9800. It is fabricated with the spindle speed of 2000RPM, feed rate of 5mm/min, and depth of cut of 2um. In this surface roughness plot, we can clearly see the spiral tool marks that is characteristic of single point diamond turning process.

Figure 2.13 shows the measurement results for Group I, which studies the relation between the arithmetic average surface roughness R_a, root mean squared surface roughness R_q and feed rate. In this figure, we also plot the theoretical surface roughness that we calculate from Equation 2.2 as well as the simulated surface roughness that we acquire using Equation 2.11 and Equation 2.12. We can see that the model we proposed gives a better estimation of the surface roughness than the theoretical predictions. The theoretical surface roughness is much lower than the actual one when the feed rate is slower than 10mm/min, but it becomes closer to the actual result when the feed rate increases. This is because in the theoretical case, we assume the cutting condition to be ideal and ignore all other factors that influence the generation of surface topography. However, in the simulated model, we take into consideration the vibration between the diamond tool and the workpiece. As a result, the prediction from the simulated model is more accurate than the

theoretical one. When the feed rate increases, the influence from tool profile starts to take over the influence from vibration, and the differences from both the theoretical case and the simulated model to the actual results become smaller. Throughout the experiment, we can observe that both the arithmetic average surface roughness and the root mean squared surface roughness for copper alloy are constantly larger than that for aluminum alloy under the same cutting condition. This could be explained by the different swelling and recovery properties of copper alloy and aluminum alloy [20]. Note also that there is still a small discrepancy between the simulated model and the actual result. This is due to other environmental factors that we do not take into consideration in the model such as variation of temperature in the diamond turning machine, air nozzle direction, cutting fluids, and other environmental vibrations around the diamond turning machine.

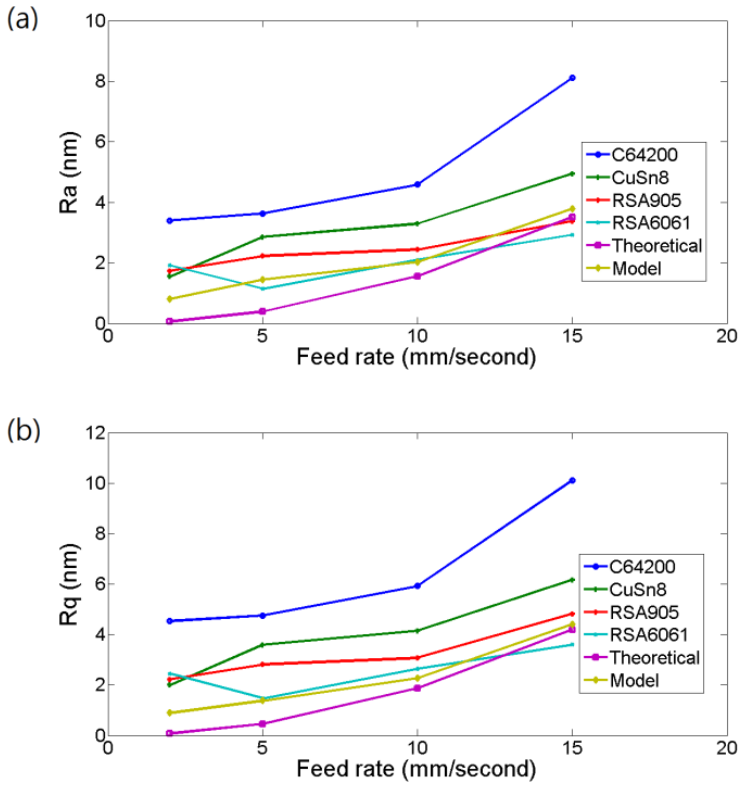

Figure 2.13 Measurement results for Group I. (a) the arithmetic average surface roughness R_a, and (b) root mean squared surface roughness R_q.

Figure 2.14 shows one of the measurement results of the diamond-turned cylindrical surface of the RSA6061 workpiece, and Table 2.2 shows the measurement results for Group II, which consists of four vertical side edge cutting tests to justify the surface topography we obtain from the proposed model. We also calculate the theoretical surface roughness as well as the simulated surface roughness in Table 2.2. We can see that the model predicts well as compared to the theoretical calculations.

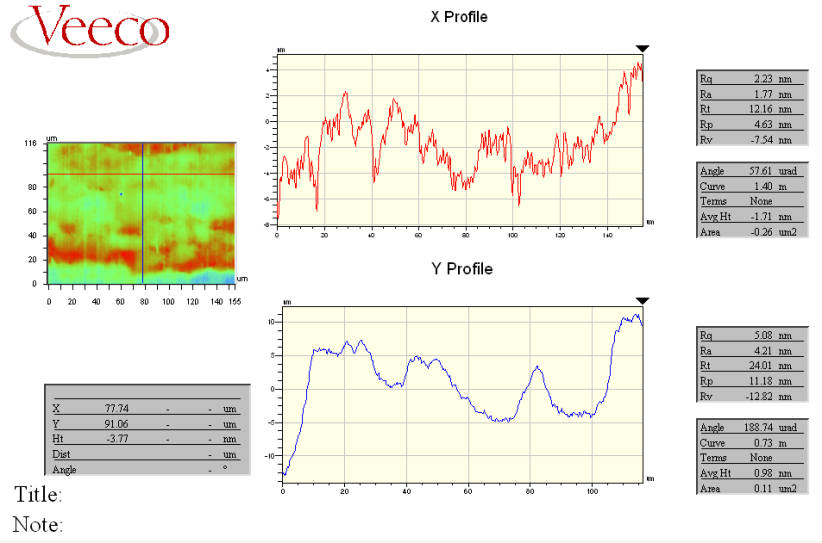

Figure 2.14 Measurement result of the RSA905 cylindrical surface.

Table 2.2 Measurement results for Group II.

	#1	#2	#3	#4	Model	Theoretical
R_a(nm)	1.77	1.82	1.79	1.90	1.45	0.39
R_q(nm)	2.23	2.18	2.29	2.36	1.66	0.46

2.4 Conclusion

We propose a model to simulate the surface topography generated by single point diamond turning machine. In the model, we take into consideration the basic tool cutting parameters and the relative vibration between the tool and the workpiece in both infeed and feeding directions. This model can describe the surface topography for flat surface and cylindrical surface of the workpiece. By proper coordinate system rotation, the model is also able to describe more complex spherical surfaces or freeform surfaces. We give an example by showing the tool tip locus on a spherical surface with and without considering the vibration in the feeding direction, and conclude that it is necessary to include both the vibrations in the infeed and feeding directions in order to make the model robust when describing curved surfaces. Further derivation of the equations for curved and freeform surfaces will be studied in future work. A series of experiments to cut flat mirror surfaces and cylindrical surfaces on several metals are performed to verify the proposed model. We find good correlation between the model and the diamond-turned parts. With this model added to the optical surface of interest, optical designers can benefit from having a more realistic lens surface to analyze and optimize.

CHAPTER 3 MODELING OF SURFACE TOPOGRAPHY ON DIAMOND TURNED SPHERICAL AND FREEFORM SURFACES

In Chapter 2, we have proposed a model to describe the surface topography of a diamond turned flat surface. However, there is a lack of a more general model to describe spherical and freeform surfaces. In this chapter, we propose a model to estimate the surface topography of the diamond turned spherical and freeform surfaces. The model takes into consideration the basic cutting parameters as well as the dominant relative vibration components between the diamond tool and the workpiece in both infeed and feeding directions. We first discuss the principles and create a model for spherical surfaces. The model is then extended to describe more general freeform surfaces. We also show how the micro waviness of the diamond tool impacts the surface topography. Finally, we conduct a series of face cutting experiments and conclude that there is good correlation between the model and the experiment results.

3.1 Three-dimensional surface topography model for spherical surface

In previous chapter, we propose a model to estimate the flat and cylindrical edge surface topography generated by single point diamond turning machine. In the model, we take into consideration the basic tool cutting parameters as well as the relative vibration between the tool and the workpiece in both infeed and feeding directions. We first find the tool tip locations along the radial direction in each revolution, and then add the diamond tool profile onto each tool tip location. Next we derive an analytical equation for the locations of interception points between neighboring tool profiles and trim the unwanted tool profile above these interception points to acquire the two dimensional surface profile along radial direction. Finally, we extend this profile to three

dimensional surface topography by considering all sections of the two dimensional surface profiles along one revolution. Figure 3.1 shows an example of the three-dimensional surface topography of a diamond-turned flat surface of the workpiece [21]. However, this model is only suitable for describing flat surfaces and we cannot simply apply this model to a curved surface. To better illustrate this, we consider a diamond-turned wedge surface. As shown in Figure 3.2(a), the black curve represents the surface profile of a diamond-turned flat surface and the red curve shows the result of directly adding the black curve to a wedge surface. It is clear that this is not the correct surface topography for a diamond turned wedge. The reason is that during the diamond turning process, the actual cutting point on the diamond tool changes constantly based on the local slope of the workpiece it cuts. For example, if the wedge angle in Figure 3.2(a) is 10°, then the diamond tool is cutting the workpiece with the portion of the diamond tool centered at 10°. When the diamond tool cuts along the wedge, each diamond profile constitutes the 2D profile of the diamond-turned wedge surface, as shown in the red curve in Figure 3.2(b). As a comparison, the black curve in Figure 3.2(b) represents the surface profile of a diamond-turned flat surface.

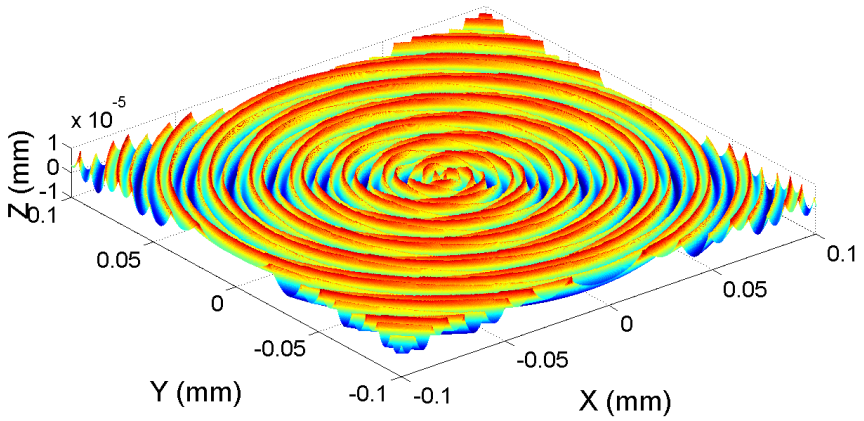

Figure 3.1 Three-dimensional surface topography of a diamond turned flat surface [21].

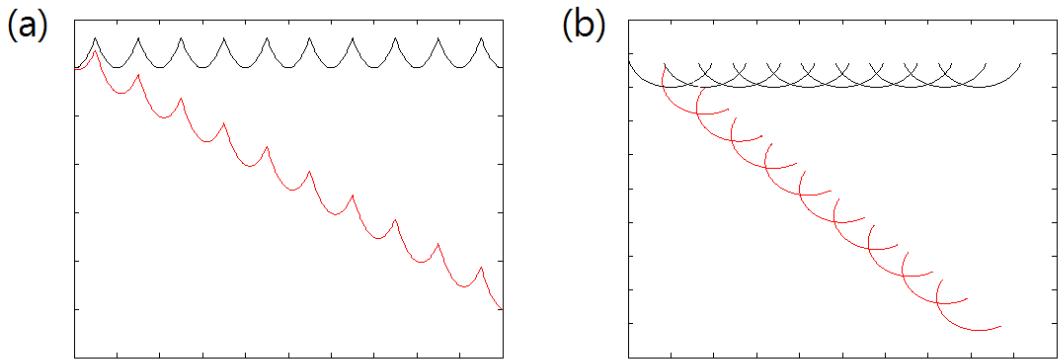

Figure 3.2 (a) The black curve shows the surface profile of a diamond-turned flat surface and the red curve shows the result of directly adding the black curve to a wedge surface. (b) The red curve shows the correct surface profile of a diamond-turned wedge and the black curve shows the profile of a diamond-turned flat surface.

Instead of using analytical equations to find the interception points for each neighboring diamond tool profiles in order to generate the surface topography as in the case of describing flat surfaces, we use a numerical approach to find each tool tip position and the interception point between neighboring diamond tool profiles for a spherical or freeform surface.

Since the diamond tool is always cutting the local surface of the workpiece perpendicularly, the surface topography at different regions of a curved surface is directly related to different portions of the diamond tool. As a result, in our model, we need to first generate a perfect diamond tool profile. This diamond tool profile serves as a reference for subsequent construction of surface topography. By including micro weaviness in this diamond tool profile, or importing a real diamond tool measurement profile, we can acquire an even more realistic model for surface topography. We will discuss the inclusion of diamond tool weaviness in more detail later in this section.

The next step is to find the tool tip locations. Recall that under ideal condition, the two-dimensional surface profile of the diamond turned surface along the radial direction can be viewed as repeated tool profiles centered at the tool tip locations at intervals of feed distance per spindle revolution (mm/rev), and the three-dimensional surface topography can be modeled based on the azimuthal progression of the two-dimensional surface profile [21]. Once we find all the tool tip locations, we can add the corresponding tool profile onto each tool tip. In our previous model, we consider the influence of the relative vibration between the tool and the workpiece in both infeed and feeding directions. This is because the relative tool-workpiece vibration in the feeding direction has equal contribution to the surface roughness generation as the vibration in the infeed direction. However, for simplicity of the derivation of equations, we only consider one dominant frequency component for each direction in the previous model. This assumption becomes less accurate if there are several dominant frequency components in the actual tool-workpiece vibration. Figure 3.3(a) and (b) show respectively an example vibration and its frequency spectrum of the relative tool-workpiece vibration in the feeding direction. We can see that although the frequency component at 33.34 Hz is the most dominant, there are also several less dominant peaks at much higher frequencies. As a result, we take into consideration multiple frequency components in the new model for more realistic estimation and better accuracy. To acquire multiple frequency components, we first set a threshold value on the frequency spectrum plot, and then retrieve all the values above this threshold. The more frequency components we take into consideration in the new model, the more accurate the model will be, but it will also be more time-consuming in the simulation process.

When we consider the radial progression of the tool from the edge of the workpiece, $-R_0$, to the center, we can acquire the positions of the tool tip in Z and X directions respectively as

$$Z_t(i,k) = Z(i,k) + \sum_{m=1}^{N_Z} A_{Zm} sin\left\{2\pi f_{Zm} \frac{[k+(i-1)N_\theta]\Delta\theta}{\omega} - \varphi_{Zm}\right\} \quad (3.1)$$

$$X_t(i,k) = -R_0 + [k+(i-1)N_\theta]\Delta R + \sum_{n=1}^{N_R} A_{Xn} sin\left\{2\pi f_{Xn} \frac{[k+(i-1)N_\theta]\Delta\theta}{\omega} - \varphi_{Xn}\right\} \quad (3.2)$$

for i=1,2,…N and k=1,2,…N_θ. A_Z and A_X are the amplitudes of vibration in each direction, f_Z and f_X are the frequencies of the vibration in each direction. The phase φ_z and φ_x are the phase shifts for the vibration in each direction. $\Delta\theta$ is the angular resolution, ΔR the radial resolution, N_θ the total number of sections around the circle, $N_\theta = 2\pi/\Delta\theta$, ω the angular speed (rad/s), R_0 the radius of the workpiece, and $N = R_0/f$ is the total number of tool tip points along the radius of the workpiece where f is feed rate (mm/rev). N_Z and N_R are the number of frequency components that are above the threshold in the infeed and feeding directions, respectively. Finally, Z(i, k) is the Z profile of the workpiece surface at point i and section k. In Equations 3.1 and 3.2, we assume that the relative vibrations between the diamond tool and workpiece are simple harmonic motions. As an example, Figure 3.4 shows the ideal vibration-free tool tip locations (blue dots) as well as tool tip locations with the consideration of vibrations (black dashed square) along a spherical surface with radius of curvature of 31mm, spindle speed of 2000 RPM, and feed rate of 10 mm/min. We purposely exaggerate the amplitude of vibration to have a clearer comparison between these two situations.

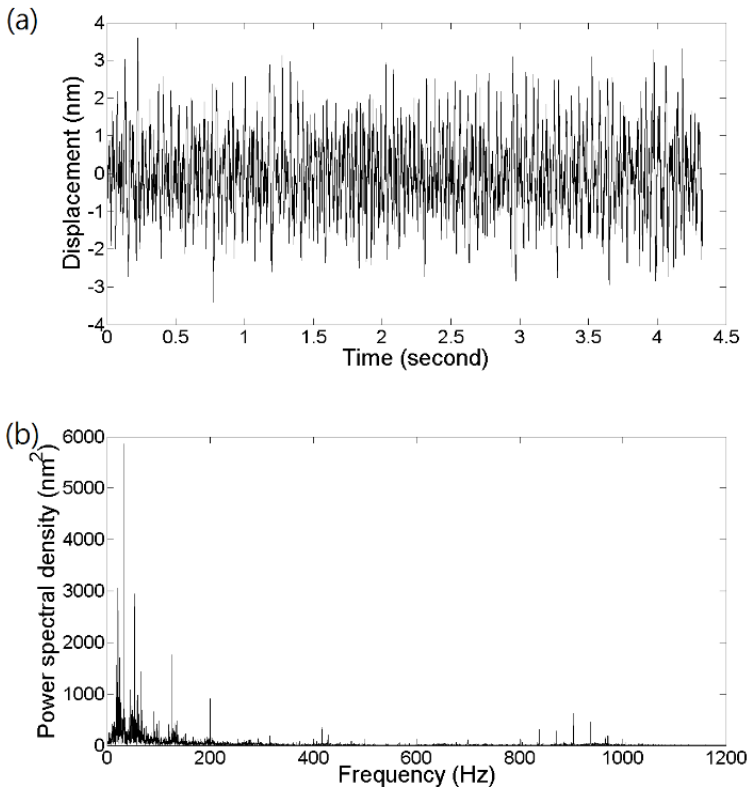

Figure 3.3 (a) An example relative tool-workpiece vibration in the feeding direction, and (b) its spectral plot.

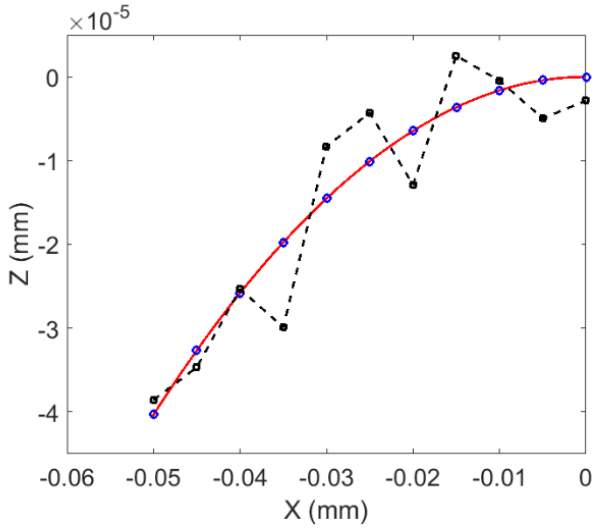

Figure 3.4 Ideal vibration-free tool tip locations (blue dots) as well as tool tip locations with the consideration of vibrations (black dashed square) along a spherical surface with radius of curvature of 31mm, spindle speed of 2000 RPM, and feed rate of 10 mm/min.

Once we locate all the tool tip coordinates, we can add the corresponding diamond tool profile onto each tool tip location. Recall that during the diamond turning process, the actual cutting point on the diamond tool changes constantly based on the local slope of the workpiece it cuts. For each tool tip position, we first calculate its slope, and then find the corresponding portion of the diamond tool profile that has the matching slope. This portion is the part of the diamond tool that is actually cutting the surface around that specific tool tip location. In our model, we constrain the portion size of the diamond tool to be equal to two times the distance between neighboring tool tip locations to avoid missing the interception point due to unexpected vibration of the neighboring tool tip location. As a result, the tool profile is centered at the tool tip, and extended to the neighboring tool tip locations. Theoretically, this is the portion that will influence the surface topography. The distance between each neighboring tool tip can be determined by the spindle speed and feed rate, and in our example in Figure 4 with the spindle speed of 2000 RPM and feed rate of 10 mm/min, this distance is 5 um.

After we attach the diamond tool profile onto each tool tip, we need to find the interception points between neighboring tool profiles. These interception points define the local upper limits of the surface topography around each tool tip location, and the diamond tool profiles underneath these interception points constitute the two-dimensional surface topography. Figure 3.5 shows an example two-dimensional surface topography for k=0 with surface radius of curvature of 31 mm, diamond tool radius of 0.5 mm, spindle speed of 2000 RPM, and feed rate of 10 mm/min. When we consider all sections around the workpiece, we can acquire the three-dimensional surface topography of the diamond-turned spherical surface as shown in Figure 3.6. Figure 3.7(a) shows the surface roughness after removing spherical form from Figure 6. In Figure 3.7(a), we consider 7 frequency components in each direction of relative tool-workpiece vibration. As a comparison,

Figure 3.7(b) shows the surface roughness after form removal as in Figure 3.7(a) but with only one frequency component in the infeed and feeding directions, respectively. We can clearly observe a more periodic pattern in Figure 3.7(b) as a result of not considering multiple frequency components in the relative tool-workpiece vibrations. This is inadequate for describing a realistic diamond-turned surface and can often underestimate the real surface roughness and create periodic patterns in the model that does not belong to the actual diamond-turned surface.

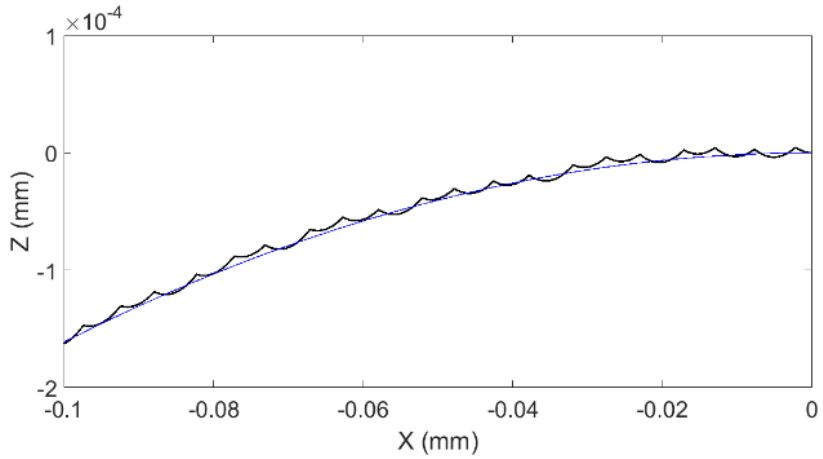

Figure 3.5 Two-dimensional surface topography for k=0 with surface radius of curvature of 31 mm, diamond tool radius of 0.5 mm, spindle speed of 2000 RPM, and feed rate of 10 mm/min.

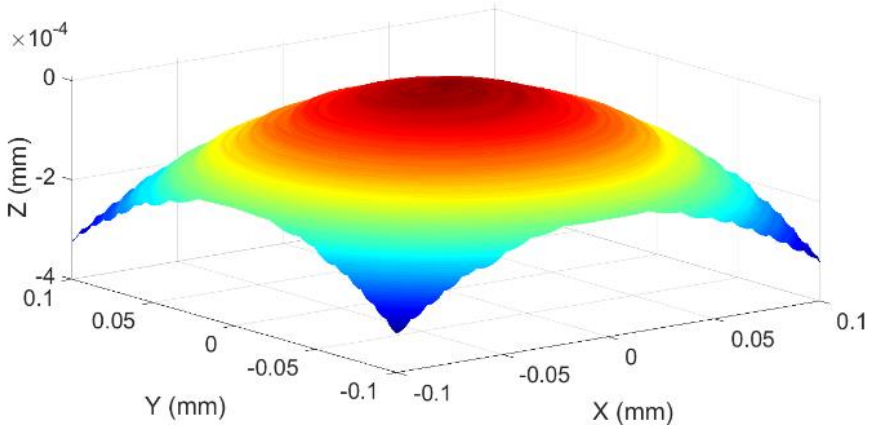

Figure 3.6 Three-dimensional surface topography of the diamond turned spherical surface after considering all sections around the workpiece.

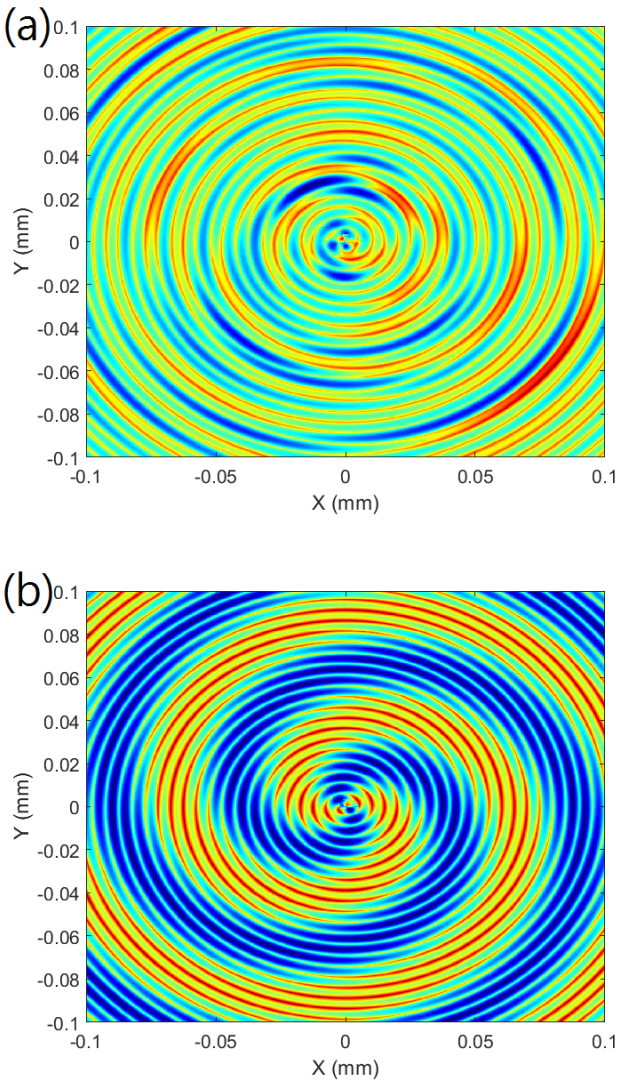

Figure 3.7 (a) The surface roughness after removing spherical form from Figure 3.6, and (b) same surface roughness but with only one frequency component in the infeed and feeding directions, respectively.

One of the advantages of this model is the ability to consider diamond tool waviness and tool wear during diamond turning process. Several researches have discussed the influence of tool wear in depth [22, 23]. Tool wear is micro waviness on the diamond tool that can degrade the optical quality of the diamond turned surfaces and greatly increase surface roughness. Figure 3.8 shows a

0.5 mm radius diamond tool with tool wear around the center of the tool profile. As mentioned earlier, the way to consider tool wear in the model is to substitute the imperfect profile that we measured from the actual diamond tool for the perfect tool profile, and use this new profile for subsequent calculations. Figure 3.9 demonstrates the two-dimensional surface topography with the consideration of tool wear. In this example, we add a series of random noise to the tool profile for simulation purpose. All other parameters remain the same as the case in Figure 3.5. Depending on the condition of the diamond tool, micro waviness on the tool profile can range from several micrometers to tens of micrometers.

Tool weaviness is the imperfection of diamond tool radius of curvature from a perfect circle. With tool weaviness, the diamond tool might undercut or overcut the surface at a specific portion with programmed numerical control (NC) code that is designated for a perfect diamond tool. This will cause surface form error and would greatly degrade the optical performance of the lens. Besides tool weaviness that comes from diamond tool itself, there is another source of error that comes from aligning the diamond tool. When we align the tool on the diamond turning machine, we need to use camera to record at least three coordinate points on the tool and calculate the corresponding tool center and best fit radius of curvature. Depending on the experience and how we choose the reference points, we might underestimate or overestimate the actual radius of curvature. This also results in the form error of the diamond turned surface. By including the tool weaviness and considering the underestimation or overestimation of the tool radius of curvature, this model can be extended to not only describe surface roughness but also estimate surface form accuracy in diamond turning process. More detailed derivation will be studied in future work.

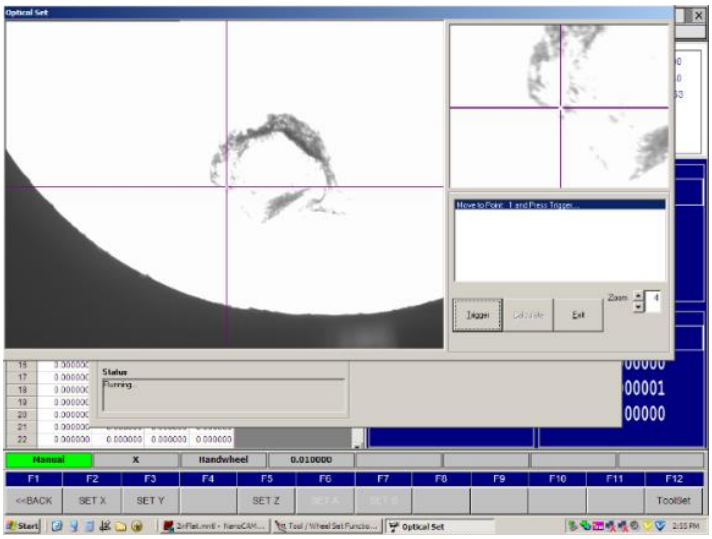

Figure 3.8 A 0.5 mm radius diamond tool with tool wear around the center of the tool profile.

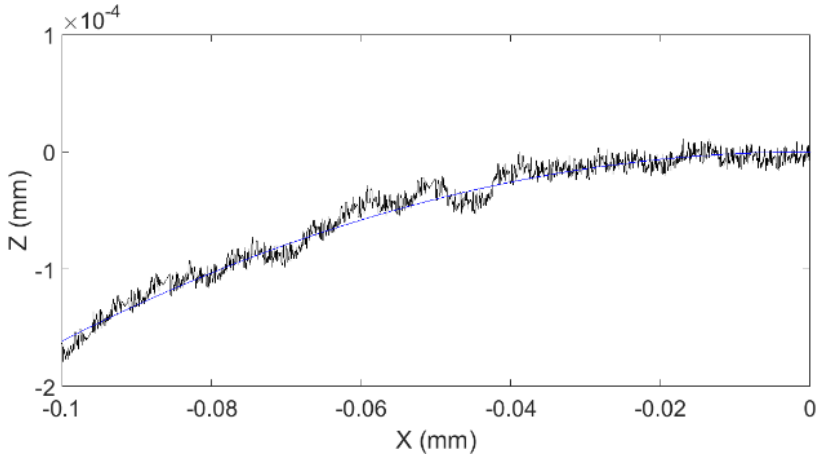

Figure 3.9 The two-dimensional surface topography with the consideration of tool wear.

3.2 Three-dimensional surface topography model for freeform surface

In this section, we extend the model to describe a more general freeform surface. The procedure for generating two-dimensional tool marks is similar to the steps as described in last section. However, since freeform surface is any non-rotationally symmetric surface, different radial sections of the freeform surface will have different profiles. The generation of each radial two-dimensional tool marks will therefore be different. Once we combine all the radial two-dimensional tool marks, we can get the three-dimensional surface topography for the freeform surface. Figure 3.10 shows an example freeform surface for laser beam shaping application [3], and Figure 3.11 shows the simulated surface topography result for that diamond turned freeform surface. The two insets show the enlarged surface topography at the center and outer edge of the surface, respectively. In this example, the simulation parameters are chosen to match the real cutting conditions with diamond tool radius of 0.5 mm, feed rate of 5 um/rev and the spindle speed is 25 RPM. Since fabricating a freeform surface is more complicated than diamond turning of a rotationally symmetric surface, there are more factors that will influence surface generation and surface roughness. For example, following errors for the Z and C coordinates in the Slow Slide Servo (SSS) can degrade surface roughness and also form accuracy. This is especially significant in the Z direction when diamond turning a freeform surface with large height variation. Besides, tool nose radius effect caused by round tool nose geometry can result in overcut of the surface and therefore deteriorate surface fidelity [24]. In our current model, we neglect these factors that influence freeform surface topography for simplicity purpose, and will investigate the inclusion of these factors in future study.

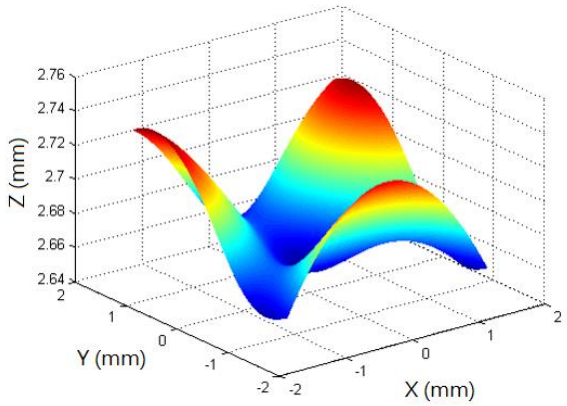

Figure 3.10 An example freeform surface for laser beam shaping application [5].

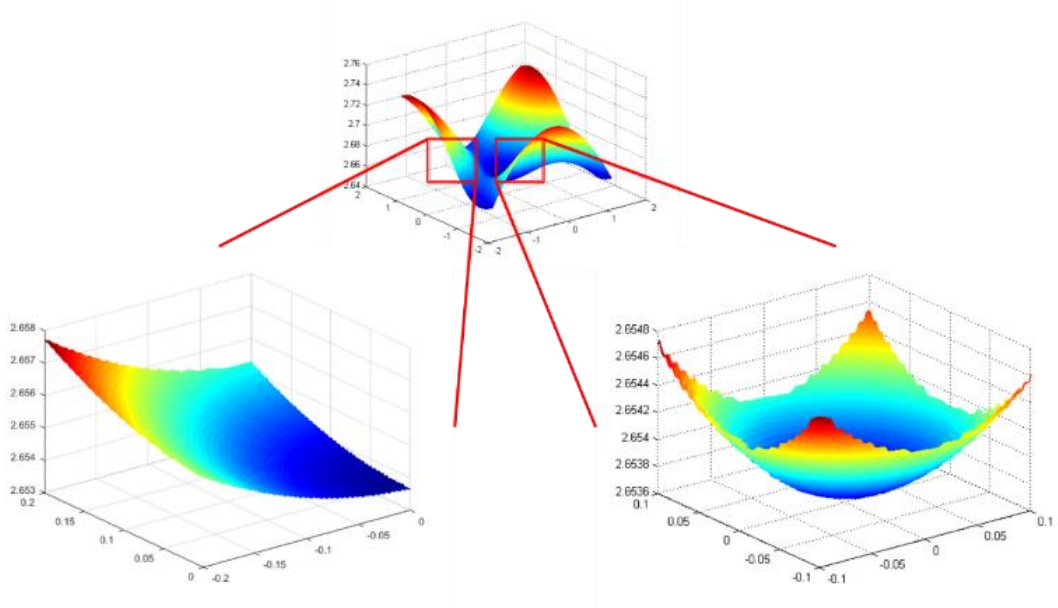

Figure 3.11 The simulated surface roughness result for the diamond-turned freeform surface in Figure 3.10.

3.3 Experimental verification

In this section, we carry out a series of diamond turning experiments to verify the proposed model. The experiments can be divided into two parts. In the first part, we cut a spherical surface to verify the surface topography obtained from the proposed model. In the second part, we analyze the relationship between feed rate and surface roughness by changing the feed rate from 5 mm/min to 20 mm/min while keeping other cutting parameters constant. All of the cutting experiments are conducted on the four-axis single-point diamond turning machine 350FG from Nanotech. Table 3.1 summarizes the cutting parameters for the two parts.

Table 3.1 Cutting parameters for the two parts.

Group	Surface Type	Spindle speed (RPM)	Feed rate (mm/min)	Depth of cut (um)	Tool Radius (mm)
I	Spherical	2000	10	3	0.5
II	Spherical	2000	5	3	0.53
II	Spherical	2000	10	3	0.53
II	Spherical	2000	15	3	0.53
II	Spherical	2000	20	3	0.53

The relative tool-workpiece vibrations in both the infeed and feeding directions are measured by the program PEWIN provided with the diamond turning machine, and the measurement results are shown in Figure 3.12. Figure 3.12(a) shows the relative tool-workpiece vibration in the infeed direction, and Figure 3.12(c) shows its spectral plot. Similarly, Figure 3.12(b) shows the relative tool-workpiece vibration in the feeding direction, and Figure 3.12(d) shows its spectral plot. As we mentioned earlier, there are actually several dominant modes of vibration in the frequency spectrum, and we would underestimate the surface roughness and obtain periodic patterns in the model that does not belong to the actual diamond-turned surface if we only consider one frequency component in each direction in the model. Throughout the experiment, we consider 9 frequency components in the infeed direction and 12 frequency components in the feeding direction, respectively.

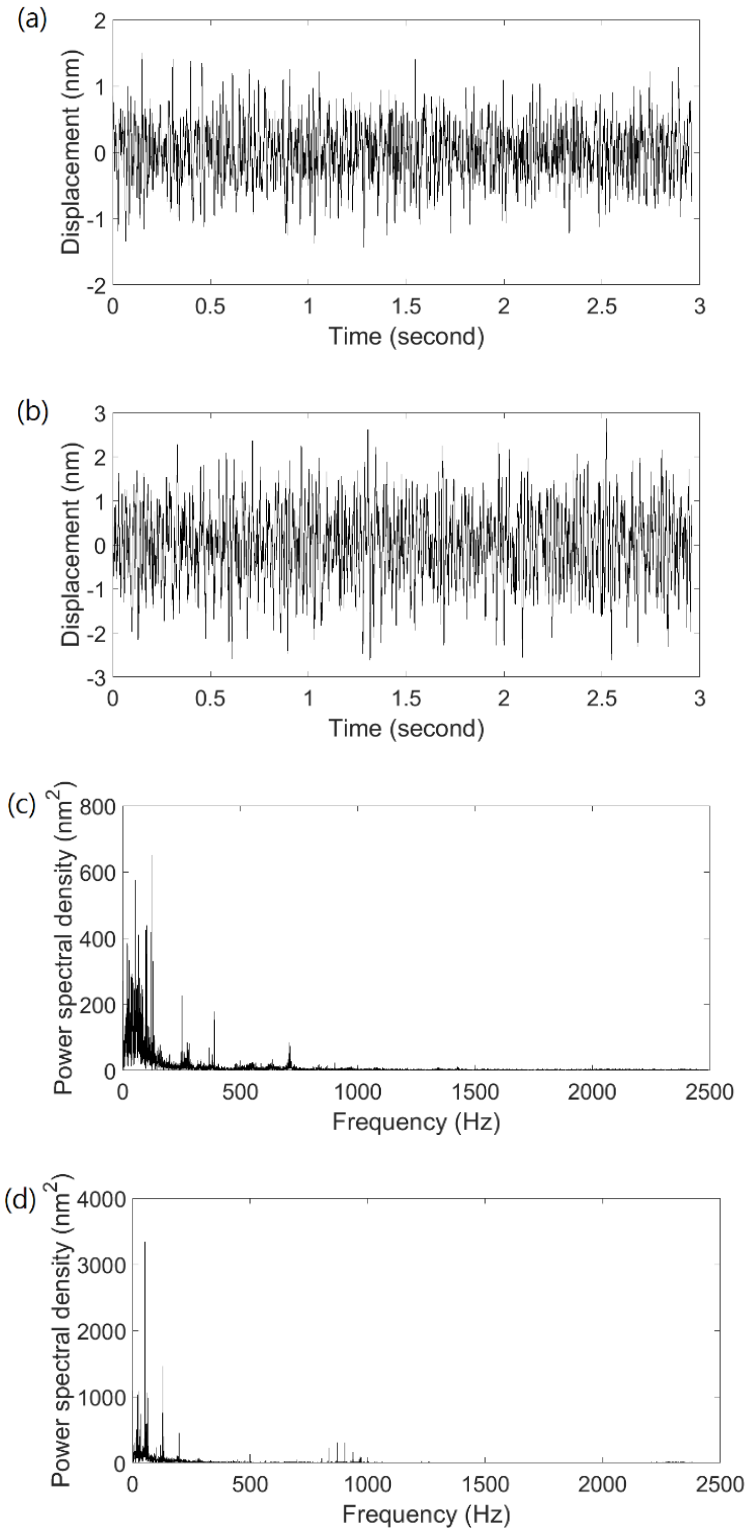

Figure 3.12 Relative tool-workpiece vibration in (a) infeed direction and (b) feeding direction, and its spectral plot in (c) infeed direction and (d) feeding direction.

In part I of the experiment, we first cut a convex spherical surface with the radius of curvature of 31mm on a high precision copper stud. The diamond tool radius is 0.5 mm, spindle speed is 2000 RPM, feed rate is 10 mm/min, and the depth of cut is 3 um. After the diamond turning process, we use ZYGO optical profilometer to measure different regions of the surface and compare the results with the surface topography estimated by the proposed model. Figure 3.13 shows the measured two-dimensional and three-dimensional surface topography of the diamond turned spherical surface. We can clearly observe in the two-dimensional topography that the diamond tool is cutting the surface with different portions of the tool at different locations along the spherical surface. This confirms our derivation that the diamond tool is always cutting the workpiece perpendicularly and matches well with the simulated two-dimensional profile in Figure 3.5. Figure 3.14 shows the comparison between the measured surface topography and the simulated results after a spherical form removal. Figure 3.14(a) is measured at the center of the spherical surface, and Figure 3.14(c) is measured 1 mm to the left of the center. Figure 3.14(b) and (d) are the corresponding simulation results. We can see that the model matches very well with the actual surface. Although there are still some local variations that the model fails to simulate, it can be overcome by including more frequency components in the model.

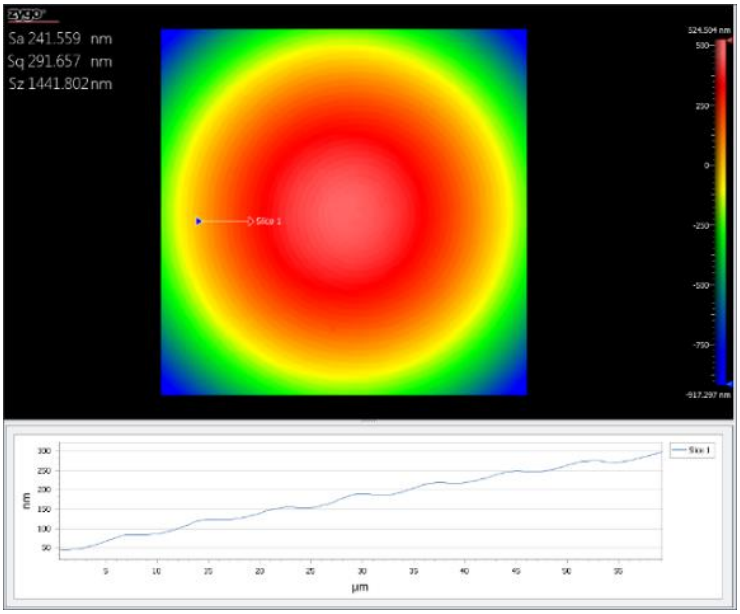

Figure 3.13 Measured two-dimensional and three-dimensional surface topography of the diamond turned spherical surface.

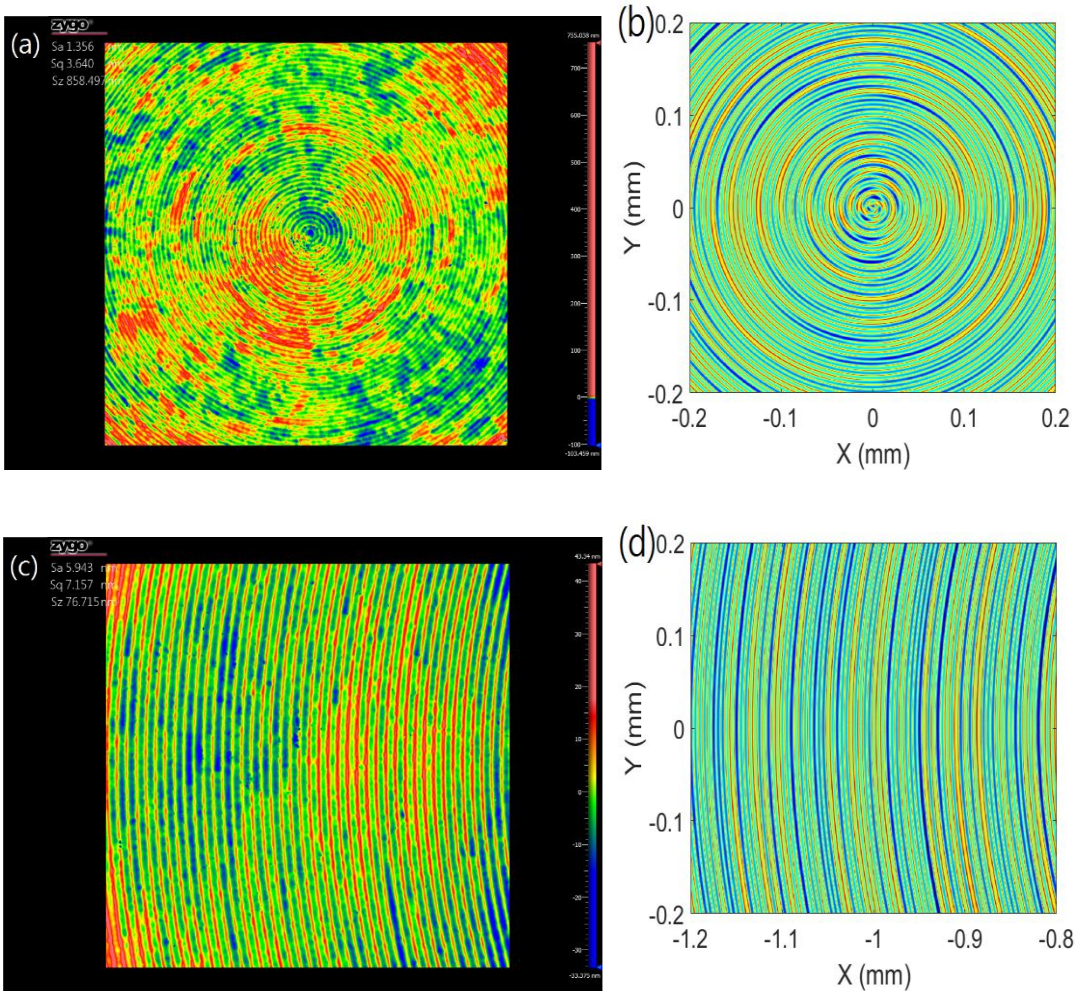

Figure 3.14 (a) Surface topography measured at the center of the spherical surface after a spherical form removal, and (b) its corresponding simulation result. (c) Surface topography measured 1 mm to the left of the center after a spherical form removal, and (d) its corresponding simulation result.

In the second part of the experiment, we cut a convex spherical surface with radius of curvature of 31mm on the same high precision copper stud and analyze the relationship between feed rate and surface roughness as listed in Table 3.1. Table 3.2 summarizes the measurement results from the Zygo optical profilometer with the spherical form removed, where R_a means the

arithmetic average surface roughness, and R_q represents the root mean squared surface roughness. Equations 3.3 and 3.4 show the formula for each parameter described above.

$$R_a = \frac{1}{n}\sum_{i=1}^{n}|z_i| \qquad (3.3)$$

$$R_q = \sqrt{\frac{1}{n}\sum_{i=1}^{n} z_i^2} \qquad (3.4)$$

From Table 3.2 we can see that the proposed model gives a very good estimation of the surface roughness when the feed rate is faster than 10 mm/min. When the feed rate is lower than 10 mm/min, the model tends to underestimate the surface roughness value. This can be explained by the influences of other environmental factors such as temperature variation, air nozzle direction, cutting fluids, and other environmental vibrations around the diamond turning machine that we did not take into consideration in the model. When the feed rate is fast enough, the influences from the relative tool-workpiece vibration and the diamond tool profile overtake other environmental factors and therefore the proposed model has a good estimation. However, when the feed rate is very slow, the influences from other environmental factors may have the same order of magnitude as the influences from vibration and diamond tool profile. In this case, these environmental factors start to dominate the surface roughness and the proposed model shows underestimation of the surface roughness value. These environmental factors can be considered and included into the model by adding a linear compensation to the surface roughness value calculated from current model.

Table 3.2 Measurement results from the Zygo optical profiler and from the proposed model.

	Feed rate (mm/min)			
	5	10	15	20
R_a(nm)	2.50	2.60	3.64	5.94
R_q(nm)	3.21	3.29	4.55	7.16
Model R_a (nm)	1.18	2.03	3.58	6.23
Model R_q (nm)	1.37	2.27	4.23	7.28

3.4 Conclusion

In this chapter, we propose a model to estimate the surface topography of the diamond turned spherical and freeform surfaces. The model differs from previous model that simulates the surface topography of a diamond turned flat surface in that the proposed model takes into consideration the local slope of the workpiece and the corresponding portions of the diamond tool that cuts the workpiece perpendicularly. The model also considers multiple dominant relative vibration components between the diamond tool and the workpiece in both infeed and feeding directions. By considering multiple frequency components in both directions, we can acquire a more realistic and accurate model and avoid creating periodic patterns that does not belong to the actual diamond-turned surface. We also show how the diamond tool waviness and micro weaviness caused by tool wear can be included into the model and how it will influence the surface profile. The model can be further extended to describe not only surface roughness but also surface form accuracy provided that we have the information of the actual diamond tool weaviness. Detailed study will be investigated in future work. A series of experiments to cut spherical surfaces on a high precision copper stud are performed to verify the proposed model. We observe a great match of the simulated surface topography and the measured result and conclude that there is a good correlation between the model and the diamond turned spherical surface. Due to other environmental factors that start

to dominate the surface topography when the feed rate becomes too slow, we suggest adding a linear term to the current model to compensate for the influences.

CHAPTER 4 DIAMOND TURNING FABRICATION OF SELF-ALIGNED AND SELF-ASSEMBLED OPTICAL SYSTEM

In this chapter, we propose a technique by integrating mechanical mounts into lens elements to fulfill a self-aligned and self-assembled optical system. To prove this concept, we designed, fabricated, and tested an ultra-compact endoscope system as well as a microscope objective that adopt this technique. By taking advantages of the specially designed fixtures and observing the interference fringes between the lens and fixture, we developed a method to minimize decenter and tilt between the two surfaces of the lens during the diamond turning fabrication process. The integrated mechanical mounts provide an easy assembly process for the lens systems while maintaining high precision in system alignment.

4.1 Introduction

Diamond turning is an ultra-precision fabrication method for generating spherical and freeform surfaces with sub-micrometric form accuracy and can reach surface roughness of only several nanometers. In addition, with the high resolution and straightness of the machine axes, we can also have a very precise control of the other specifications of the lens such as lens thickness, lens diameter, lens decenter and tilt. It is therefore advantageous to utilize these ultra-precision characteristics of the diamond turning machine to fabricate complex lens systems both for high imaging quality and fast prototyping. There have been many publications about the diamond turning fabrication of freeform lenses or other complex lenses in all aspects of applications [3-4, 25-30]. However, there is relatively few publications about the fabrication, alignment, and assembly process analysis of lens

systems generated by diamond turning process [31-33]. In this chapter we propose a new technique in designing a lens system that integrates mechanical mounts into each lens element. We can directly assemble the lenses without lens barrel for holding the lenses. This optical system is therefore very compact, lightweight, low cost, and easy to assemble, while having high imaging quality.

4.2 Fabrication of the ultra-compact endoscope system

4.2.1 System specification

To demonstrate the concept, we designed and prototyped a three-lens endoscope system that adopts this technique. In this design, we used a CMOS sensor which is 400 pixels by 400 pixels with each pixel size 3 um by 3 um. The size of the sensor array is therefore 1.2 mm by 1.2 mm, and the sensor dimension is 1.8 mm by 1.8 mm including packaging. As a result, we set the outer diameter of endoscope lenses to be 1.8 mm to match the size of the sensor. The design specifications are listed in Table 4.1 and the lens configuration of the proposed endoscope is shown in Figure 4.1. The endoscope has a diagonal half field of view of 27° and F/# of 4. Lens 1 and lens 3 are made from OKP-1, and lens 2 is made from polymethyl methacrylate (PMMA). OKP-1 is a flint-like material with low Abbe number (v=22) and high refractive index (n=1.64) [34] while PMMA behaves like a crown material. With the combination of OKP-1 and PMMA, we can effectively correct chromatic aberration. Besides, both OKP-1 and PMMA are easy to fabricate through diamond turning process, and they are also suitable materials for plastic molding if mass production is desired in the future. Figure 4.2 shows the corresponding modulation transfer function (MTF). It shows that the endoscope has a diffraction-limited

performance.

Table 4.1 Design specifications of the proposed endoscope.

Diagonal half field of view	27°
F/#	4
Clear aperture	0.92 mm
Outer diameter	1.8 mm
Wavelength range	486 to 656 nm
Total length	3.469 mm

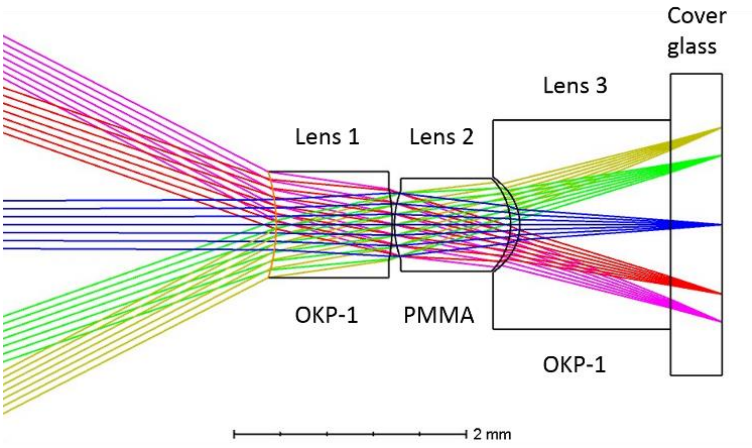

Figure 4.1 Lens configuration of the endoscope system.

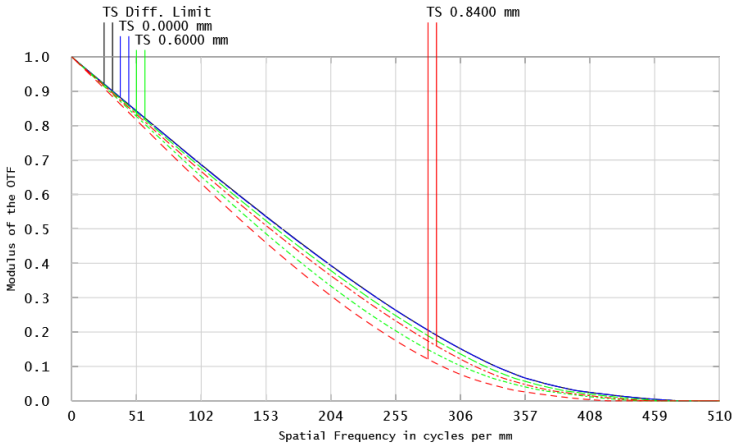

Figure 4.2 Modulation transfer function of the endoscope system.

A tolerance analysis was performed in Zemax to verify that the endoscope could be fabricated in-house by the diamond turning machine. The tolerances were set to have a worst case MTF of 30% at the Nyquist frequency, which is 166 cycles per mm at a test wavelength of 587 nm. As a comparison, the design has a nominal MTF of 45% at the Nyquist frequency. Table 4.2 lists the tolerance values based on the in-house diamond turning capability. A Monte Carlo simulation was performed to perturb the tolerance values listed in Table 4.2 and generate 500 samples. Over 90% of the Monte Carlo samples have the MTF of at least 33% at the Nyquist frequency. This simulation result shows that the proposed endoscope with adequate performance could be achieved in-house provided that the tolerance values in Table 4.2 are met.

Table 4.2 Tolerance values for the proposed endoscope.

Radius of curvature (%)	±1
Thickness (um)	±5
Surface decenter (um)	±5
Surface tilt (°)	±0.1
Element decenter (um)	±5
Element tilt (°)	±0.1
Index	±0.001
Abbe number	±1

4.2.2 Modified system design

Traditionally, lenses are assembled in the lens barrel with specially designed mechanical mounts that can both hold the lenses in place and help align each lens on the optical axis. However, the use of mechanical mount becomes challenging when the lens diameter reduces significantly to 2mm or less. In such a case, not only is the fabrication of lens barrel and mechanical mounts extremely difficult, but the finished lens barrel will also significantly increase the total size and weight of the system. The prototype we propose here integrates the mechanical mounts to the lens element itself so that we can simply clip each lens onto another lens element, and the mechanical mounts serve as the aligning and supporting purpose. As a result, there is no need to have an extra lens barrel to hold the lenses. Figure 4.3 shows the modified system layout from Figure 4.1 with the addition of mechanical mounts on each lens element, and Figure 4.4 shows the detailed dimensions of the mechanical mount in Lens 1. From Figure 4.3, we can see that the clear aperture of

each lens surface is unchanged, and the structures added onto the lens will not influence the imaging capability. In this modified design, we choose to have interference fit (press fit) between each neighboring lens element. This means that two parts are fastened together by friction after the parts are pushed together. As an example, the inner diameter of the mechanical mount at the left side of modified lens 2 is 1.2 mm, and in order to have the press fit for lens 1 and 2, the outer diameter of the mechanical mount at the right side of modified lens 1 is set to be 1.19 mm. The same criterion is chosen for all the modified lens surfaces. Although there is a 12 um air gap between lens 2 and lens 3 in the original design, this air gap can be maintained by the precise control of the thickness difference between the mechanical mounts on lens 2 and lens 3 during diamond turning process.

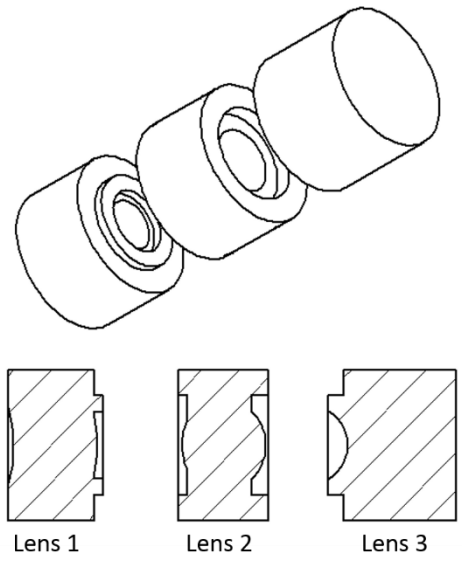

Figure 4.3 Modified endoscope system design considering integrated mechanical mounts.

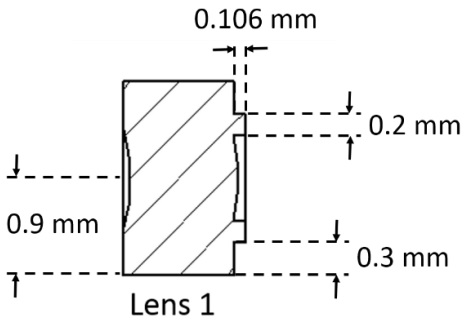

Figure 4.4 Detailed dimensions for the integrated mechanical mount on Lens 1.

4.2.3 Fabrication of the fixture

Because the size of the endoscope lens is so small, it cannot be directly held on the spindle. As a result, we need to design a fixture that can securely hold the endoscope lens. The fabrication of the fixture is analogous to cutting a series of circular steps. Because these circular steps have vertical side walls, it is beneficial to use a half radius diamond tool to cut these circular steps. Figure 4.5 shows a half radius diamond tool with tool radius of 0.07 mm and a flat surface on the left side. Theoretically, if we can align this half radius diamond tool to be perfectly perpendicular to the spindle surface, we will be able to cut perfect vertical side walls of the circular steps. However, since we are using a camera that is hung on the Y axis of the diamond turning machine for alignment, the alignment of the half radius diamond tool is limited by the alignment of the camera, and it is not possible to perfectly aligned the half radius diamond tool. There will be two situations for the misalignment of the half radius diamond tool, as shown in Figure 4.6. Figure 4.6(a) shows that the half radius diamond tool is rotated clockwise by a few degrees. In this case, the included angle of the half radius diamond tool changes from the original 0° - 60° to about 10° - 70°, assuming the half radius diamond tool has an included angle of 60° and is rotated

clockwise by 10°. It is obvious that the 0-degree point is not in the range that this half radius diamond tool can cut, so this kind of tool setup cannot fabricate the flat surfaces of the circular steps of the fixture. Besides, because of the clockwise rotation of the tool, the original flat surface at the left side of the half radius diamond tool also becomes tilted. When we use this setup to cut the circular steps, the tilted left side surface will hit the fixture surface and create a tilted side edge, as shown in Figure 4.7(a).

On the other hand, Figure 4.6(b) shows the half radius diamond tool that is rotated counterclockwise by a few degrees. In this case, the included angle of the half radius diamond tool changes from the original 0° - 60° to about -10° - 50°. The 0° point is included in the range of this half radius diamond tool and therefore it can cut the flat surface of the circular step. Because the half radius diamond tool is now tilted in the direction opposite to the case in Figure 4.6(a), the tilted flat surface at the left side of the half radius diamond tool will not hit the vertical side edge of the circular step when the tool cuts into the fixture, as shown in Figure 4.7(b).

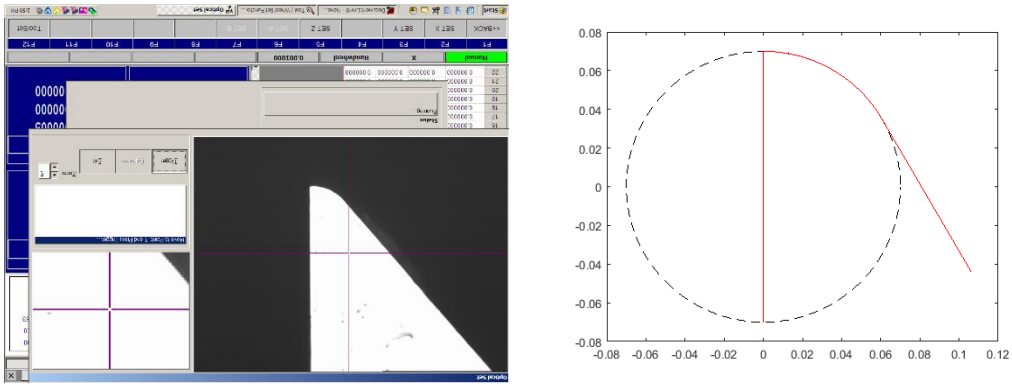

Figure 4.5 A half radius diamond tool with tool radius of 0.07 mm and a flat surface on the left side.

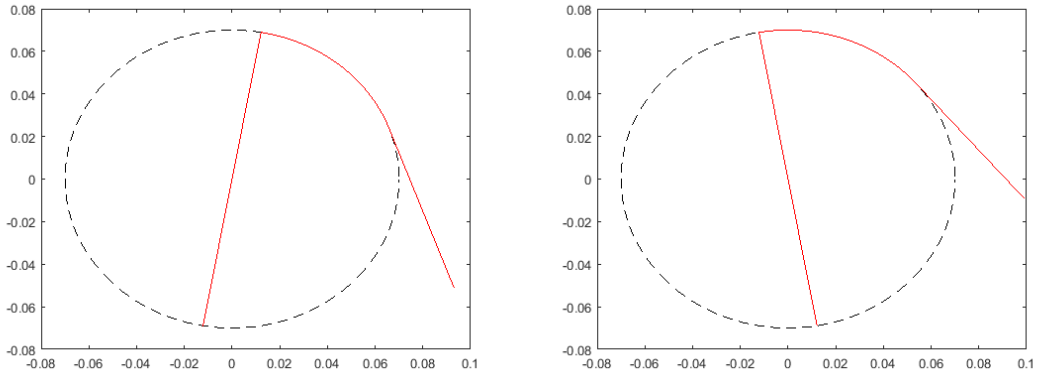

(a) (b)

Figure 4.6 Misalignment of the half radius diamond tool. (a) Tool is rotated clockwise by 10° and (b) tool is rotated counterclockwise by 10°.

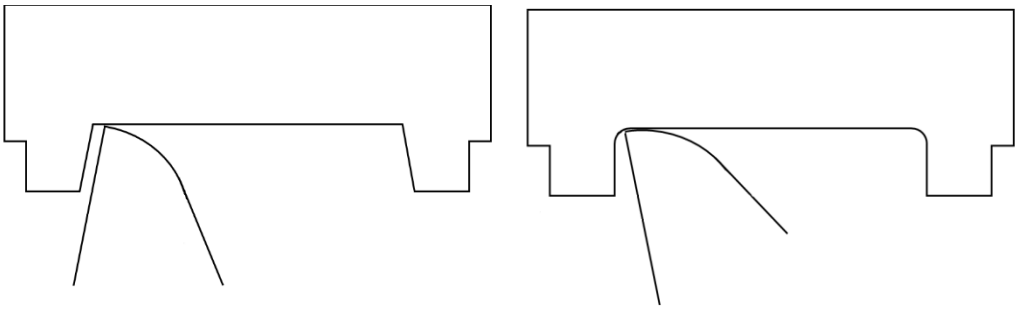

(a) (b)

Figure 4.7 Circular steps generated by the half radius diamond tool that is rotated (a) clockwise by 10°, and (b) counterclockwise by 10°.

However, in order to cut the step size to its designed value, we would need to compensate for the tilt of the half radius diamond tool. As shown in Figure 4.6(b) and 4.7(b), although the half radius diamond tool is still cutting the flat surface of the circular step using the 0° point, the actual point that is touching the vertical side wall is the tool tip with the -10° point rather than the flat side of the diamond tool. The influences of this rotated

diamond tool are that the actual step size is slightly larger than the designed value due to the tilted -10° point and the side wall will have a rounded corner instead of vertical because of the -10° - 0° arc, which is demonstrated in Figure 4.7(b). The circular step diameter difference can be calculated as 2*0.07*sin(10°)=24 um and the height of the rounded corner is 0.07*cos(10°)=68 um. As a result, when we use this setup to cut a circular step, we need to offset the tool X coordinate by -12 um in order to compensate for the 24 um difference from the perfect circular step diameter. Besides, the rounded corner may cause the lens not being able to fit perfectly into the fixture. This issue can be overcome by adding a small chamfer at the edge of the lens to avoid contact with the rounded corner. Because of the issue caused by a clockwise rotated half radius diamond tool, we always rotate the half radius diamond tool counterclockwise by several degrees to make sure its 0-degree point can cut the flat surface and the diamond tool flat surface does not hit the vertical side wall.

4.2.4 Fabrication of the endoscope lenses

After all the fixtures are fabricated, we are ready to cut the lenses. In this section, we present a detailed process of fabricating the side edges of the lens to its designed diameter. Recall that the diamond tool always cut the local workpiece surface perpendicularly. As a result, the included angle of the diamond tool must include the 90° point in order to cut the vertical side edge of the lens. However, regular diamond tools usually have an included angle from -60° to 60°, and we must rotate the diamond tool by at least 30° to cover the 90° point which is used to cut the vertical side edge of the lens. Figure 4.8 shows a 0.5 mm radius diamond tool that is rotated by 35° to cut the side edge of the lens. The included

angle of this diamond tool now ranges from -25° to 95°.

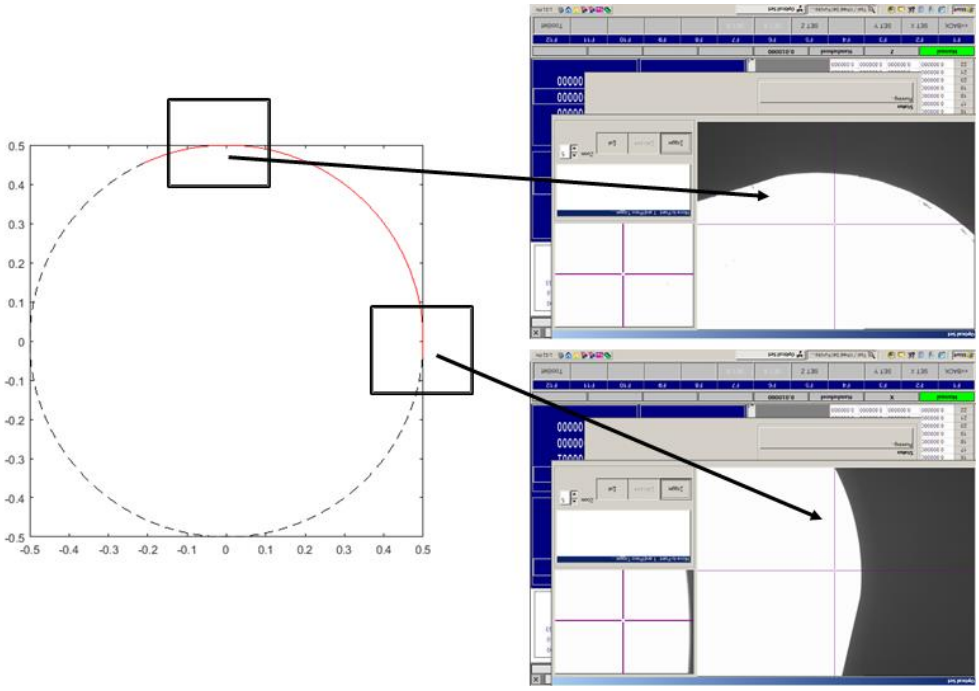

Figure 4.8 A 0.5 mm radius diamond tool rotated by 35° to cut the vertical side edge of the lens. The inset shows the 0° point and 90° point.

Once the diamond tool is installed and aligned properly, we can start to cut the vertical side edge. Instead of steadily moving the spindle in X direction while changing the Z position of the diamond tool constantly to cut regular spherical lens surface, we develop a program that can fix the X and Y coordinates of the spindle and only allow the diamond tool to move steadily in Z direction and use the 90° point to cut the side edge. Since the diamond tool is aligned on the Z axis stage such that the X and Y coordinates in the program represent the location of the center of curvature of the diamond tool, we need to compensate for the offset caused by the tool radius when cutting the side edge of the lens using the 90°

point of the diamond tool. As an example, assume we have a 0.5 mm radius diamond tool and would like to cut a PMMA rod with 10 mm in diameter, we need to first rotate the diamond tool by about 35 degrees and align the tool. We then roughly align the PMMA rod on the spindle. Next we input all the required parameters (tool radius, feed rate, spindle speed, depth of cut, lens size, and lens thickness, etc.) into the developed Matlab program to generate the tool path with offset to cut the side edge of the PMMA rod. This offset is to make sure that we can fabricate to the exact lens diameter as we need. To be more specific, in the final loop of the tool path program, the tool position should be located at -5.5 mm due to the 5 mm PMMA rod radius and the 0.5 mm tool radius, assuming the spindle is rotated counterclockwise.

4.2.5 Decenter control during fabrication process

One of the most important factors that will influence optical imaging quality of a diamond-turned optics is the misalignment between the two surfaces of the lens during fabrication process. In order to achieve high precision of the specifications for each lens in the proposed endoscope system, we investigated and developed some methods that can help to improve the alignment between lens surfaces. The misalignment can be divided into decenter and tilt. The decenter between the two surfaces of a lens is limited by the precision of the indication of each surface on the spindle center. For regular lenses, we can directly indicate each surface to be well-aligned on the spindle center no matter the lens is fixed in the fixture or vacuumed on the spindle directly. However, this is usually not the case for ultra-compact lenses. The thickness for the lenses in this proposed endoscope system is no more than 1 mm, and once the lens is fixed into the fixture, there will be less

than 0.5 mm of space for the indicator probe to contact the lens edge. As a result, it is challenging to directly indicate the lens.

Instead of directly indicating the lens itself, we cut another circular ring at the outer edge of the fixture for indication purpose during the fabrication process of the fixture so that this outer ring and the circular-step fixture structure are concentric at the spindle center. Figure 4.9 shows a detailed view of the fixture. Rather than indicating the lens, we can indicate the vertical side wall of the outer ring to make sure the fixture is centered at the spindle. By the precise control of the circular step size, we can be sure that the fixture can hold the lens strong enough and the displacement of the lens from the fixture center is kept within the tolerance specification. In our design, the step size of the fixture is set as 10 um larger than the diameter of the lens. In this way, we can have a press fit between the lens and the fixture. Depending on the lens surface shape that is inserted into the fixture, we need to change the total number and the size of each circular step accordingly. As an example, Figure 4.10(a) shows the fixture for a lens with a concave surface. We only need to fabricate one step to properly hold the lens. On the other hand, Figure 4.10(b) shows the fixture for a lens with a convex surface. In this case, two steps are necessary. The first step is to hold the lens and fix it in the fixture center. The second step is only an open space to accommodate the convex surface and to avoid any contact between the fixture and the lens surface. According to our experiment, we can indicate the outer ring of the proposed fixture and align it on the spindle center with less than 0.2 um radial runout. This means that most of the decenter of the lens comes from the displacement of the lens in the fixture circular-step structure, which is at most 5 um in this case.

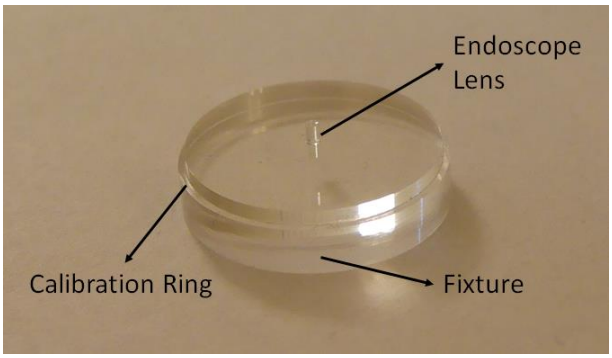

Figure 4.9 Fixture for ultra-compact lenses.

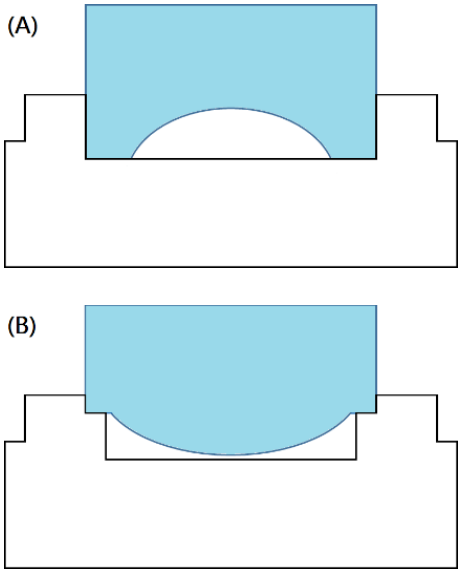

Figure 4.10 Modified fixture with an outer indication ring for (a) lens with flat or concave surface, or (b) lens with convex surface.

In order to verify the amount of displacement of the lens in the fixture circular-step structure, we cut a 3 mm long, 1.8 mm in diameter PMMA rod with the same cutting parameters as we fabricated the endoscope lenses. This PMMA rod was put into the fixture and glued. Then the fixture was held on the spindle, and we indicated the outer ring of the fixture until we had about 0.2 um radial runout, showing that the fixture was nicely centered

on the spindle. Next we used the indicator to indicate the PMMA rod and read out the total radial runout value. This value corresponds to two times the decenter value between the PMMA rod and the spindle center. Figure 4.11 shows the setup of the experiment. This experiment procedure was repeated five times, and the mean value of the decenter was 1.53 um with a standard deviation of 0.38 um. The result shows that using the calibration ring on the fixture is effective and the amount of decenter is within the tolerance listed in Table 4.2.

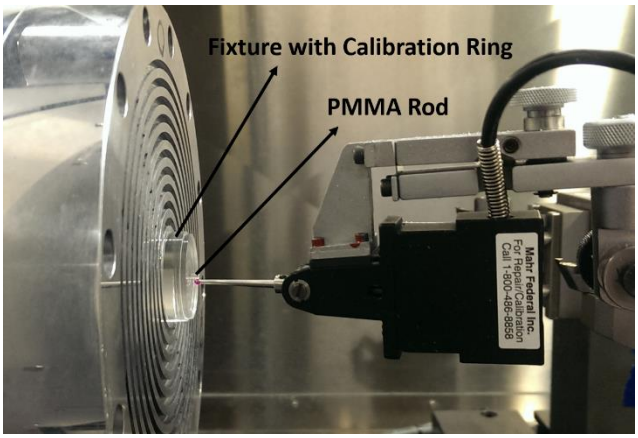

Figure 4.11 Setup for decenter measurement on the spindle.

4.2.6 Tilt control during fabrication process

As for controlling the tilt between two surfaces of the lens element, we propose using interference fringes to minimize the tilt between the fixture front surface and the lens back surface, and it will in turn minimize the tilt between the two surfaces of the lens. We take the flat portion of the fixture surface that makes contact with the lens surface to be the reference flat. Depending on the fixture type we use, different flat surface on the fixture serves as the reference flat. As an example, in Figure 4.10(a), the bottom surface of the central circular step is the reference flat, and in Figure 4.10(b), the bottom surface of the smaller circular step that holds the convex surface serves as the reference flat. Once the lens is inserted into the fixture, the portion of the flat surface of the lens will have interference with the fixture flat surface provided that the wedge angle between these two surfaces is small enough. If the wedge angle is too large, there will be too many interference fringes present and therefore making the observation rather difficult. The working principle is similar to a Fizeau interferometer, but now the reference surface is the fixture front flat surface and the test surface is the flat portion of the lens. Figure 4.12 shows some of the interferograms for a Fizeau interferometer [35]. By comparing the interferogram we acquire from the fixture and lens surfaces and the interferograms in Figure 4.12, we can easily have an understanding of how well the lens is aligned on the fixture. Since the fixture surface and the lens surface are both flat, we would expect the interference fringes between these two surfaces to be straight lines. If the observed fringes are not straight, we know either the fixture flat surface or the flat surface of the lens is incorrectly fabricated, or there might be some deformation on the surfaces. By calculating the fringes, we can have a quantitative measurement on the amount of tilt. Figure 4.13 gives an example of the

interference fringes between the fixture and one of the endoscope lenses. The lens surface that was in contact with the fixture is a flat surface. In this figure, we purposely created a small amount of wedge between the lens and fixture surface to show the interference fringes.

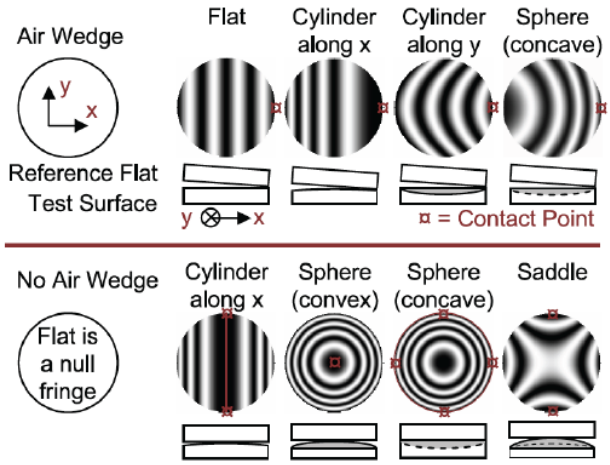

Figure 4.12 Some interferograms of Fizeau interferometer [35].

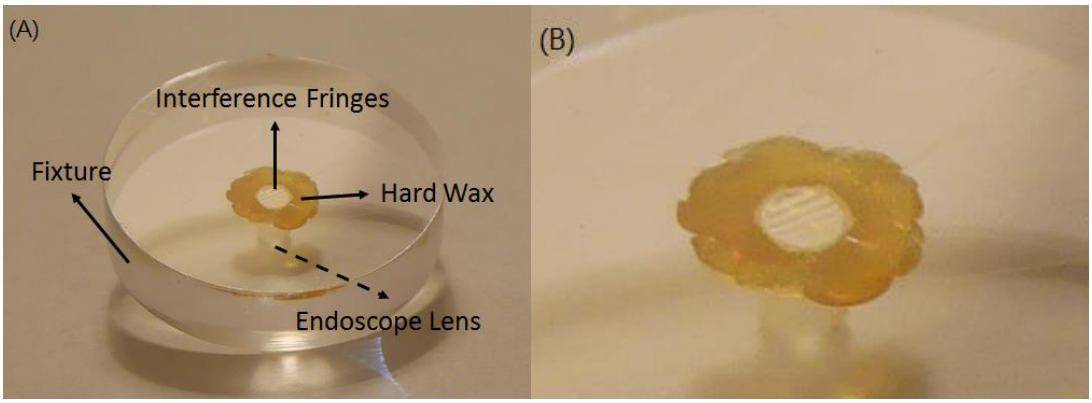

Figure 4.13 (a) The setup for observing interference fringes between the fixture and lens surface. (b) Enlarged interference fringes. We can clearly see the straight fringes, which means the two surfaces are flat, and there is no unexpected deformation. In order to minimize tilt, we need to null the fringes between these two surfaces.

All the fixtures we discussed so far were made from PMMA rod for low cost and fast prototyping. After the lens was put into the fixture, we used hard wax to secure them.

The tilt between the fixture and the lens surface is mainly caused by the difference between the internal diameter of the fixture and the diameter of the lens. Although this 10 um difference in diameter is necessary for the lens to be press fitted into the fixture, it will inevitably cause tilt between the two surfaces if the lens is not perpendicularly inserted into the fixture. When there is tilt and the straight interference fringes are present, we can simply push one side of the lens surface and observe the motion of the fringes to know the direction of the wedge. We can then minimize the wedge by nulling the interference fringes. These procedures are done after we apply hard wax around the fixture and lens, and before the hard wax is totally cooled down and hardened.

Before assembling the endoscope, we measure the tilt between the two surfaces of each lens to make sure they are within tolerances. We put a microscope slide under the Zygo NewView optical profilometer, and adjust the tilt of the stage to reduce the tilt of the microscope slide to 0.001°. We then put each lens on the microscope slide and measured the front surface. Next we removed tilt from the measurement result, and the amount we removed is the tilt between the front surface and the back surface of the lens. Figure 4.14(a) gives the tilt of Lens 1, which is 0.023°. The tilt for Lens 2 and Lens 3 are 0.052° and 0.064°, respectively. As a comparison, the tilt of the complete endoscope is 0.022°, and the setup is shown in Figure 4.14(b). The result shows that the amount of tilt between the two surfaces is within the tolerance value listed in Table 4.2.

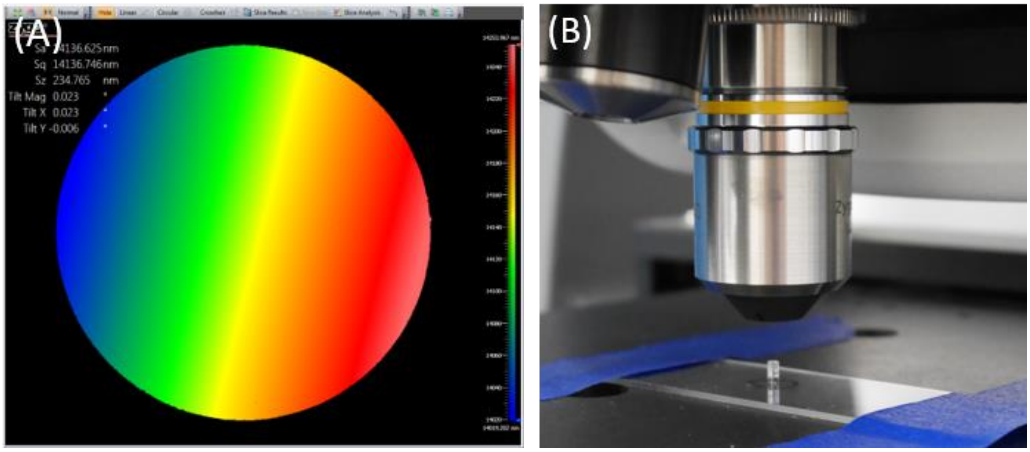

Figure 4.14 (a) Tilt measurement result for Lens 1. (b) Setup for the tilt measurement for the whole endoscope system.

4.2.7 Assembly of the endoscope system

Once we fabricate all three endoscope lenses, we can simply assemble them by pressing each lens and clipping onto another lens element to build the endoscope system. However, the resulting imaging quality was poor due to a large amount of stray light that went into the system from the outer structure of the lens element. Besides, although each lens can be clipped onto another, it is still not strong enough. In order to have a stable and reliable endoscope system, we need to do some extra steps in the assembly process. The first step is to blacken all the areas outside of lens clear aperture to minimize stray light that goes into the system. We use black ink and permanent marker to blacken these areas. For a compact system, this method is cost effective and time saving. After blackening the lenses and assembling the endoscope, we propose applying a heat shrink tube outside of the endoscope lenses as the supporting structure as well as a second layer to further reduce stray light. We chose a heat shrink tube with diameter slightly larger than that of the endoscope system, put the assembled three-lens endoscope into the heat shrink tube, used

a micrometer to hold the endoscope lenses and heat shrink tube in place, and applied gentle heat to gradually shrink the heat shrink tube. Figure 4.15 shows the completed ultra-compact endoscope system after we attached the endoscope to the CMOS sensor. Here we applied a thin layer of PDMS to glue the endoscope onto the sensor cover glass to avoid any air gap between them. In Figure 4.15, we also show a complete set of individual endoscope lenses. The rightmost lens is blackened by a permanent marker to demonstrate how it can block stray light that comes from outside of field of view. Figure 4.16 shows a preliminary testing result of the endoscope system in resolving a 1951 USAF target. The smallest resolvable features are group 3, element 2 with a resolution limit of 8.98 line pairs per mm. The expected resolution limit is about 10.5 line pairs per mm. With this endoscope system, we can have a high resolution of the images. However, the contrast of the image is not as high as expected. One reason could be the limitation that we are not able to fully blacken the lens surface outside of the aperture stop. This causes a small amount of stray light going into the system from the mechanical mounts and eventually reaches the sensor. A more detailed study about the testing and stray light analysis of this endoscope system will be discussed in future work.

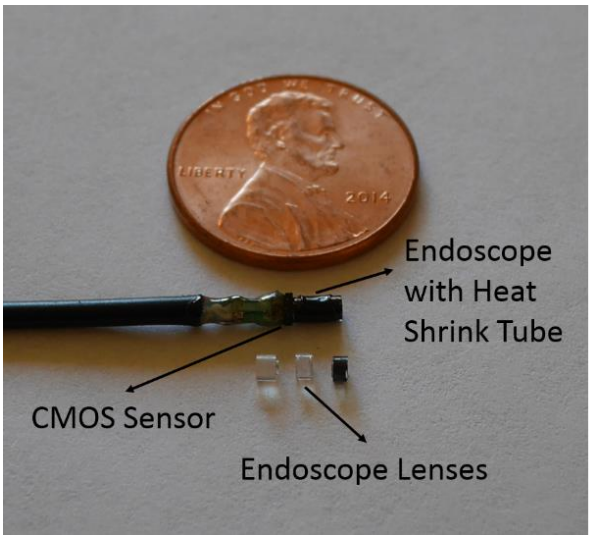

Figure 4.15 Proposed ultra-compact endoscope system.

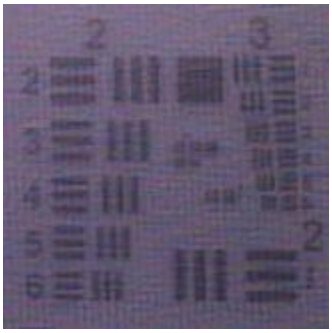

Figure 4.16 Preliminary testing result of the proposed endoscope system.

4.3 Fabrication of the microscope objective system

4.3.1 System specification

As a second example of the lens system that utilizes this technique, we design a microscope objective that is made up of four plastic lenses. The design specifications are listed in Table 4.3 and the lens configuration of the microscope objective is shown in Figure 4.17. The microscope objective has a NA of 0.5. Lens 1 and lens 3 are made from polymethyl methacrylate (PMMA), and Lens 2 and Lens 4 are made from OKP-4 HT.

There are four aspheric surfaces in this design. Figure 4.18 shows the corresponding modulation transfer function (MTF).

Table 4.3 Design specifications of the microscope objective.

NA	0.5
Clear aperture	11 mm
Outer diameter	13 mm
Wavelength range	798 to 1000 nm
Total length	15.7 mm

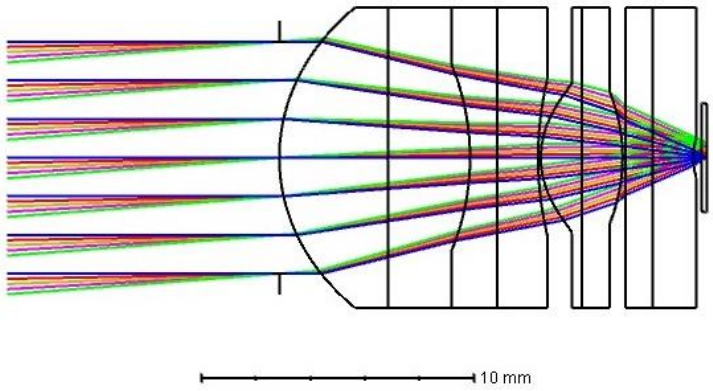

Figure 4.17 Lens configuration of the microscope objective.

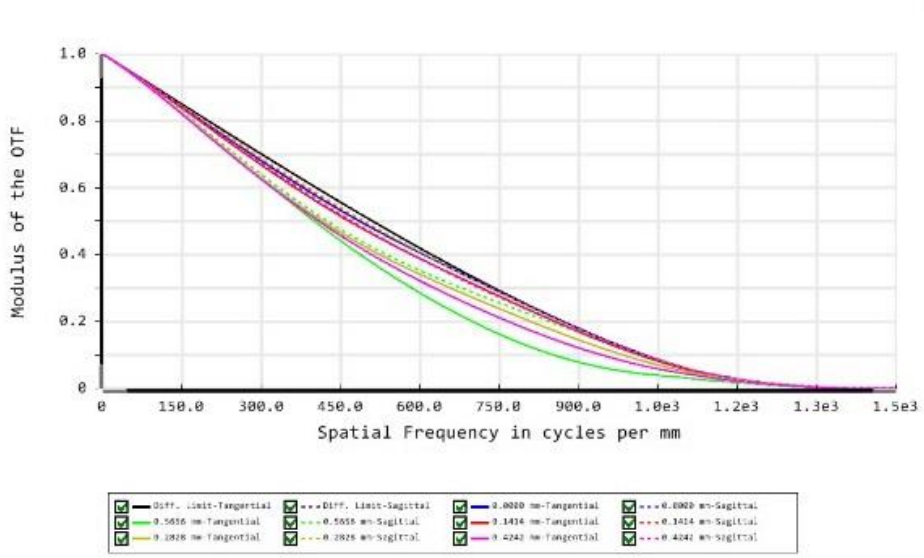

Figure 4.18 Modulation transfer function of the microscope objective.

4.3.2 Modified system design

With the similar procedure of adding mechanical mounts outside of the lens clear aperture as the endoscope system, we can get the modified lens layout for diamond turning fabrication, as shown in Figure 4.19. In this case, the lens clear aperture is 11mm, and the lens diameter including integrated mechanical mount is 13mm. We apply press fit between two lenses so that when we clip one lens onto the other, the mechanical mounts are strong enough to hold the lenses while maintaining the alignment of the lenses within the tolerance value. The step height of every mechanical mount is set to be 0.7 mm. Ideally, the step height should be large enough to hold the lens steadily. However, because we are diamond turning the mechanical mount structure and the lens surface at the same time, the maximum permissible step height is limited by the lens profile, radius of the half radius diamond tool, and the primary clearance angle of the diamond tool.

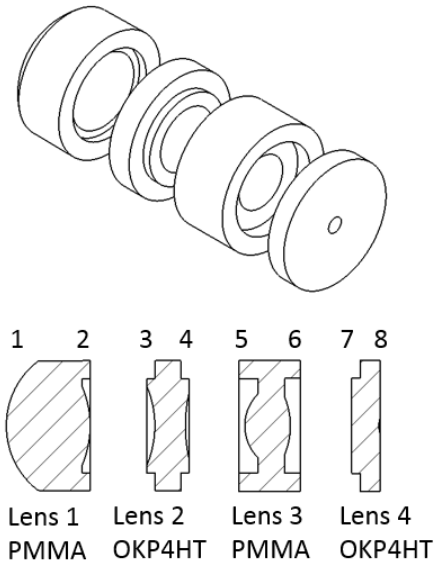

Figure 4.19 Modified microscope objective design considering integrated mechanical mounts.

4.3.3 Diamond turning fabrication of the microscope objective lenses

In order to avoid or minimize the number of fixtures to make for the microscope objective, we need to determine the fabrication order for each lens surface. As an example, when we fabricate Lens 1, if we diamond turn the aspheric convex surface 1 first, then we would need a fixture similar to Figure 4.10(b) to hold this convex surface in order to cut surface 2. On the other hand, if we diamond turn surface 2 first, we can use the flat portion of surface 2 outside of the lens clear aperture as the base and avoid using any extra fixture to hold the lens when fabricating surface 1.

Since some of the lens surfaces in this microscope objective design are aspheric surfaces, it is difficult to measure those surfaces directly by using traditional interferometry. As a result, we first find the best fit sphere for those aspheric surfaces, and calculate the corresponding radius of curvature. Figure 4.20 shows the sag table of the concave aspheric surface (Surface 8) of Lens 4 in the microscope objective design as well as its

corresponding best fit sphere sag and the deviation between the aspheric sag and the best fit sphere sag. Instead of diamond turning the aspheric surface directly, we first cut the best fit sphere on the lens. Then we use interferometer to measure this spherical surface. By iteratively measuring the diamond-turned best fit spherical surface and fine adjusting the diamond tool X and Y positions, we can optimize the diamond tool position and minimize the form error of the best fit sphere. Figure 4.21 shows the measurement result of the best fit sphere for Surface 8. With the peak-to-valley value of 0.068 waves and the RMS error of 0.012 waves, we know that this best fit sphere surface is well within the tolerance value. Next we use this same diamond tool setting to cut the actual aspheric surface. By removing the deviation portion between the aspheric sag and the best fit sphere sag, which is at most 6 um in this case, we can finish the final aspheric surface in only several extra loops, and at the same time be confident that the aspheric surface form error is within the tolerance value. This method of iteratively measuring the best fit sphere and fine adjusting the diamond tool position is applied to all of the aspheric surfaces in the microscope objective system.

1: Sag Table

Units are Millimeters.
Slope units are dimensionless.
Semi-Diameter of surface 14: 7.182198E-001.
Algorithm assumes +z goes from glass to air.

Method: Minimum Volume Removal
Best Fit Sphere Radius   :   2.395168E+000
Best Fit Sphere Vertex Offset :   0.000000E+000
Maximum Depth to Remove   :   5.483209E-003
RMS of Depth to Remove   :   4.013966E-003
Maximum Slope Deviation   :   8.859120E-002
RMS Slope Deviation   :   2.895965E-002
Volume To Remove   :   5.946750E-003   cubic Millimeters

Y-coord	Sag	BFS Sag	Deviation	Remove
0.000000E+000	0.000000E+000	0.000000E+000	0.000000E+000	0.000000E+000
2.000000E-002	7.028701E-005	8.350292E-005	-1.321591E-005	1.321591E-005
4.000000E-002	2.812392E-004	3.340291E-004	-5.278994E-005	5.278994E-005
6.000000E-002	6.331313E-004	7.516311E-004	-1.184998E-004	1.184998E-004
8.000000E-002	1.126425E-003	1.336396E-003	-2.099711E-004	2.099711E-004
1.000000E-001	1.761776E-003	2.088447E-003	-3.266714E-004	3.266714E-004
1.200000E-001	2.540039E-003	3.007941E-003	-4.679027E-004	4.679027E-004
1.400000E-001	3.462280E-003	4.095072E-003	-6.327924E-004	6.327924E-004
1.600000E-001	4.529786E-003	5.350069E-003	-8.202828E-004	8.202828E-004
1.800000E-001	5.744075E-003	6.773195E-003	-1.029120E-003	1.029120E-003
2.000000E-001	7.106908E-003	8.364753E-003	-1.257845E-003	1.257845E-003
2.200000E-001	8.620300E-003	1.012508E-002	-1.504778E-003	1.504778E-003
2.400000E-001	1.028653E-002	1.205455E-002	-1.768014E-003	1.768014E-003
2.600000E-001	1.210816E-002	1.415357E-002	-2.045408E-003	2.045408E-003
2.800000E-001	1.408802E-002	1.642259E-002	-2.334567E-003	2.334567E-003
3.000000E-001	1.622926E-002	1.886210E-002	-2.632839E-003	2.632839E-003
3.200000E-001	1.853532E-002	2.147263E-002	-2.937301E-003	2.937301E-003
3.400000E-001	2.100999E-002	2.425473E-002	-3.244740E-003	3.244740E-003
3.600000E-001	2.365739E-002	2.720902E-002	-3.551635E-003	3.551635E-003
3.800000E-001	2.648202E-002	3.033614E-002	-3.854119E-003	3.854119E-003
4.000000E-001	2.948883E-002	3.363678E-002	-4.147942E-003	4.147942E-003
4.200000E-001	3.268326E-002	3.711166E-002	-4.428396E-003	4.428396E-003

Figure 4.20 Sag table of one of the aspheric surfaces in the microscope objective as well as its corresponding best fit sphere sag and the deviation between the aspheric sag and the best fit sphere sag.

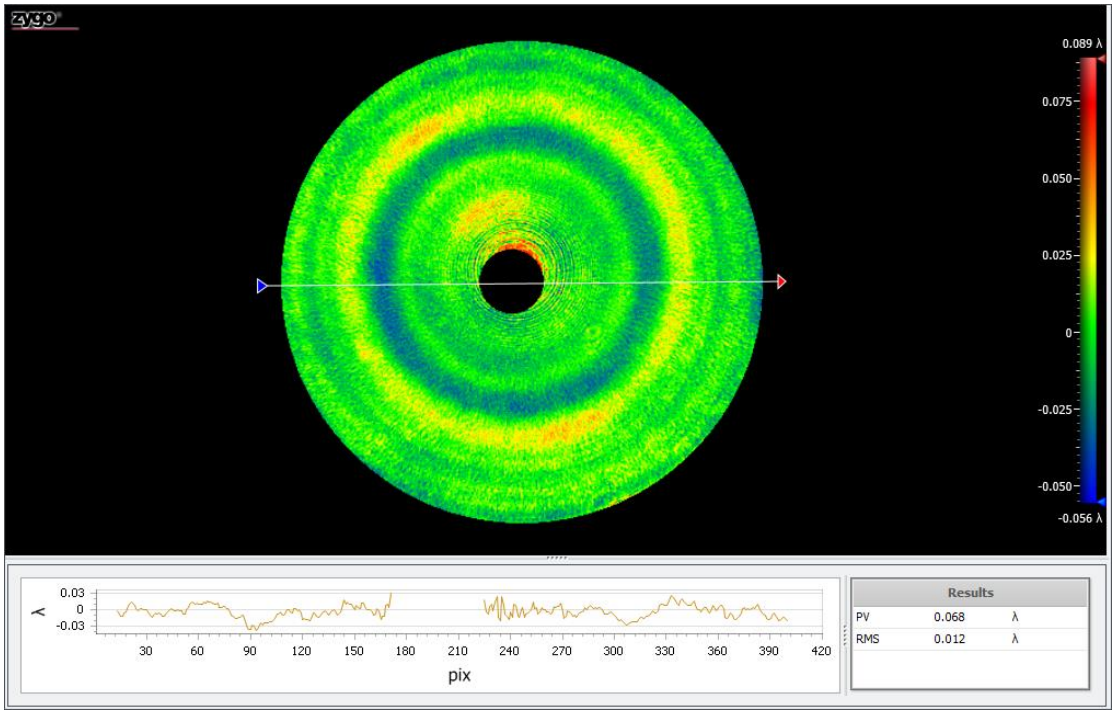

Figure 4.21 Interferometer measurement result of the best fit sphere for the concave aspheric surfaces of lens 4.

4.3.4 Assembly of the microscope objective

Figure 4.22 shows the completed lens elements as well as the drawing of the modified lenses. We can clearly see the mechanical structures outside of lens clear apertures that serve as assembling and aligning purpose. Figure 4.23 shows the case when we clip all the lenses together. There are no extra steps needed for the assembly process. Because in this microscope objective design, Lens 1 and Lens 2 are cemented doublet, and Surface 3 is a spherical surface picked up from Surface 2, we need to put extra caution in the fabrication and assembly of these two surfaces. As mentioned in Section 4.3.2, the step height of every mechanical mount is set to be 0.7 mm, but the step height in surface 2 is purposely set to be slightly less than 0.7 mm, say, 0.68 mm. In this case, when we assemble Lens 1 and

Lens 2, the spherical portions of Surface 2 and Surface 3 will contact each other while the flat portions of the mechanical mounts in Surface 2 and Surface 3 will have a small gap and can never touch each other. This can guarantee that Surface 2 and Surface 3 always cement well and no air gap may present between these two spherical surfaces due to the influence of the mechanical mounts outside of the lens clear aperture.

Figure 4.24 shows the final assembly of the entire microscope objective when we put the assembled lenses into the lens barrel and apply the glass window at the front end of the microscope objective.

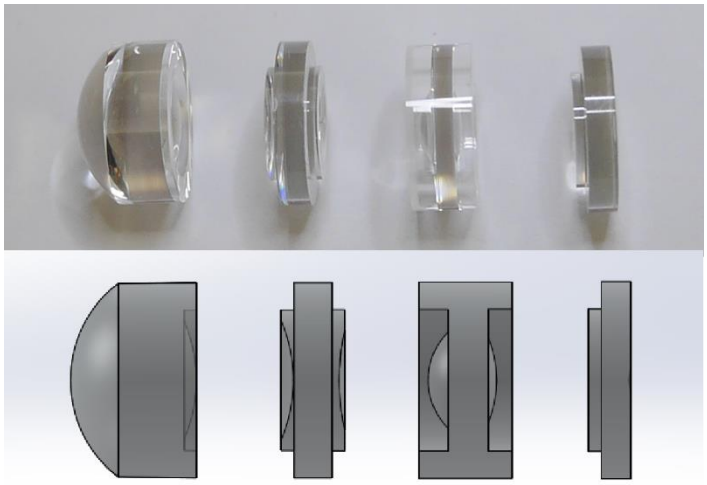

Figure 4.22 Completed microscope objective lens elements and the modified lens drawing.

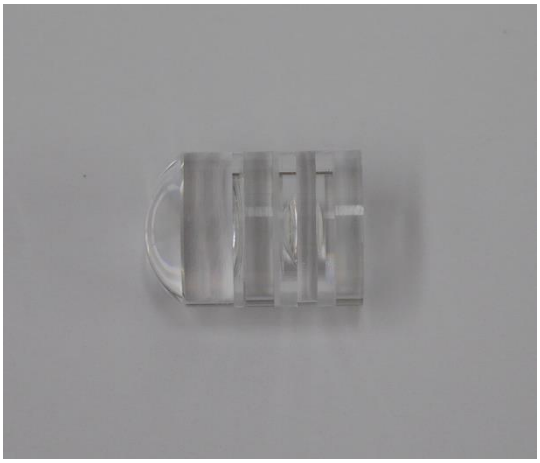

Figure 4.23 Microscope objective after all the lens elements are assembled together.

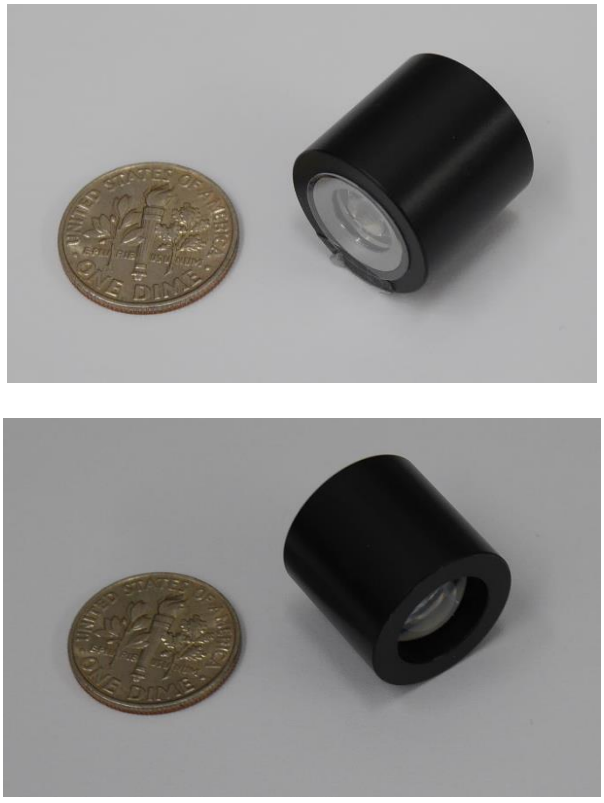

Figure 4.24 Final assembly of the microscope objective.

4.3.5 Testing of the microscope objective

Because this microscope objective is designed as infinitely corrected, we can test it by replacing one of the microscope objective under a commercial microscope with the one we fabricated. Figure 4.25 shows a preliminary testing result of the microscope objective system in resolving a 1951 USAF target. We see that the optical system can resolve all the features in the 1951 USAF target down to group 9, element 3 with a resolution limit of 645.1 line pairs per mm. The measured resolution and contrast is much better than the case for the ultra-compact endoscope in previous section. The better system performance comes from the fact that we cut the best fit sphere and minimized its form error before the finish cut for every lens surface, and this can greatly constrain the surface form error to be well within the tolerance value. However, there is still stray light that goes into the system as we did not take any stray light reduction procedure in this preliminary testing. One way to reduce stray light is to use permanent marker or dark ink to blacken the surfaces outside of the lens clear aperture.

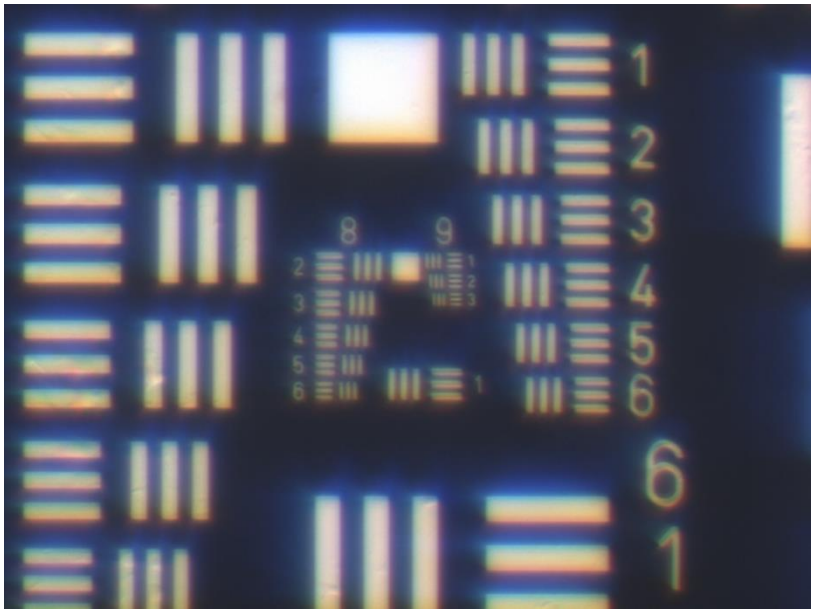

Figure 4.25 1951 USAF target measurement result.

4.4 Conclusion

In this chapter, we propose a technique which integrates the mechanical mounts into each lens element so that they can be assembled by simply clipping each lens into another. This configuration is therefore very compact, lightweight, easy to assemble, low cost; it can maintain good imaging quality as well. To demonstrate the concept, we designed and fabricated a three-lens ultra-compact endoscope system as well as a four-lens microscope objective with the consideration of adding specific mechanical mount on each lens element. During the diamond turning fabrication process, we designed a fixture with an extra outer ring to help indicate the lens on the spindle center in order to minimize decenter between the two surfaces of the lens. We also used interference fringes to aid in correcting tilt between the lens and fixture. By observing the interference fringe patterns between the fixture flat surface and the flat portion of the lens surface and trying to null the interference fringes, we were able to minimize the tilt between the lens and the fixture, which in turn can significantly improve imaging quality of the lens system. Finally, we show the assembly and testing results of the two systems and conclude that the technique we proposed is promising in getting a self-aligned and self-assembled lens system with high imaging quality.

CHAPTER 5 DIAMOND TURNING FABRICATION METHOD AND ANALYSIS FOR BLAZED GRATINGS

In this chapter, we discuss about the diamond turning fabrication method and analysis for circular blazed gratings. Commercial software tends to generate tool paths that undercut the grating surface but with correct grating profile. We present another tool path generation method for circular blazed gratings that can generate correct step height but with the cost of overcutting the grating profile. In order to have a detailed analysis and comparison on the performance of the blazed gratings with different fabrication methods, we propose a model to simulate the surface topography of the diamond turned blazed gratings with the consideration of basic cutting parameters. We also include the influences resulted from the diamond tool tilt in this model. The model is then used to evaluate the grating performance and diffraction efficiency. Finally, a conclusion on optimal fabrication method for blazed gratings with highest diffraction efficiency is suggested.

5.1 Tool path generation and fabrication of circular blazed gratings

In this section, we discuss about the tool path generation and fabrication process of circular blazed gratings. Throughout this chapter, we use the commercial software NanoCAM2D provided by Moore Nanotechnology Systems to design the circular blazed gratings. The design of blazed gratings in NanoCAM2D can be thought of as a combination of straight lines with a specific slope and vertical lines. One of the most important differences between blazed gratings and aspheric surfaces is that there are slope discontinuities in the gratings while the slopes in aspheric surfaces are always continuous. Recall that the diamond tool is always cutting the local surface of the workpiece perpendicularly, which means the cutting point of the diamond tool along the workpiece

profile has the same slope as the local workpiece surface it is cutting. As a result, at the point where there is a slope discontinuity, the diamond tool can never cut the surface correctly because of the finite size of the diamond tool nose radius. In such a case, we would either overcut or undercut the surface. As an example, we design a blazed grating with the groove spacing of 50 um and the step height of 5 um in NanoCAM2D. The diamond tool is set to be a half radius diamond tool with the tool radius of 50 um and the flat side on the left. When we use NanoCAM2D to design the gratings, the tool path it generates tends to undercut the grating profile. This is shown in the tool path simulation in Figure 5.1, where the diamond tool does not actually cut to the bottom of the grating. Instead, it stops at the point where the diamond tool is tangent to the grating. This will cause the grating to have an incorrect step height but correct grating profile. Such undercut situation can be improved by choosing a diamond tool with smaller radius. Several research groups have also proposed their tool path generation methods for cutting the circular gratings [30, 36-39]. However, most of them are focused on the fabrication methods based on a five-axis diamond turning machine, which has a rotational B-axis that can rotate the diamond tool in accordance with the spindle C-axis and the translational axes. In such a case, they can choose a sharply pointed diamond tool and use the tool tip to cut the whole grating. However, this is not the case for our current setting of the diamond turning machine, as we do not have the rotational B-axis.

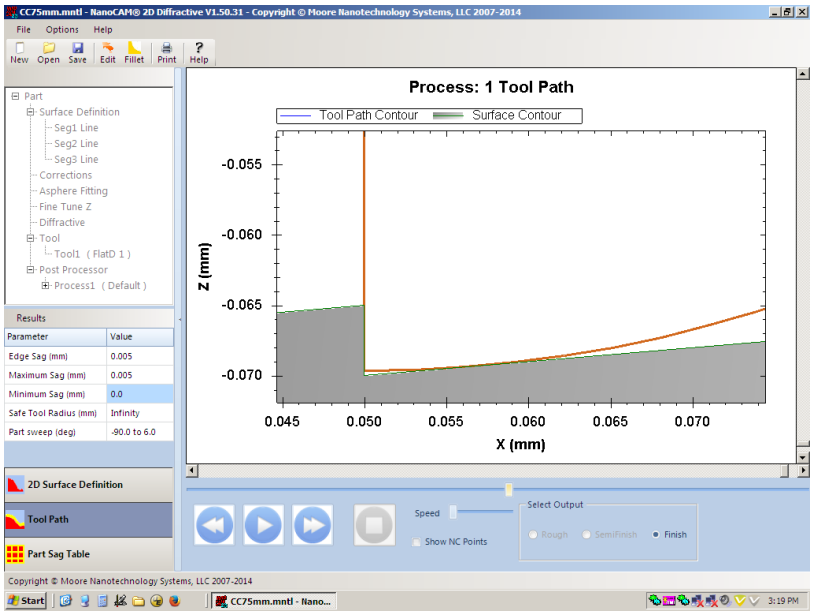

Figure 5.1 Simulated tool path for the circular blazed grating from NanoCAM2D.

5.1.1 Tool path generation for circular blazed gratings

We use Matlab to generate the tool path for cutting the circular blazed gratings with correct step heights. Although this tool path can produce correct step height, it will inevitably create an overcut into the grating and therefore generate an incorrect grating profile. The generation of the tool path can be divided into two steps. In the first step, we generate the tool path to cut one period of the grating, which is essentially equivalent to cutting a straight line with a specific slope. With the groove spacing and the step height from the design specification, we can calculate the slope of the grating, and find the corresponding diamond tool portion with the same slope that actually contacts the grating surface during the cutting process. Figure 5.2 shows the simulated tool path for cutting one period of the grating. The red line shows the ideal grating profile; the blue curves show the half radius diamond tool profile, and the black arrow shows the direction of the tool path. In this example, we have the groove spacing of 25 um, step height of 5 um, diamond tool

radius of 30 um, and the cutting speed is set to be 5 um per revolution. We can notice that, due to the tool nose radius effect, a small portion of the grating near the bottom is not properly removed by the diamond tool, causing the step height to be smaller than the ideal value. This undercut of the step height is the same as the situation caused by the tool path generated from NanoCAM2D, and it will be corrected in next step.

For the second step of the tool path generation, we need to carefully design the tool path so that we can cut the correct step height while minimizing the influence to the other part of the grating. This is done by first allowing the diamond tool to plunge into the bottom of the grating. This will inevitably cause some overcut of the grating due to the tool nose radius effect, as shown in Figure 5.3. After we cut the correct step height of the grating, we cannot just move the diamond tool along the grating profile, as this will create even more overcut of the grating before the diamond tool is tangent to the grating profile. As a result, we move the diamond tool straight up a small distance until the diamond tool is tangent to the grating. Next, we can repeat Step I and move the diamond tool along the grating to finish one period of the grating, which is shown in Figure 5.4. By the repeated combinations of Step I and Step II, the tool path for the entire grating can be generated. In this way, we can make sure that we obtain the true step height as required by the design specification, and we do not create extra overcut of the grating other than the initial plunge cut.

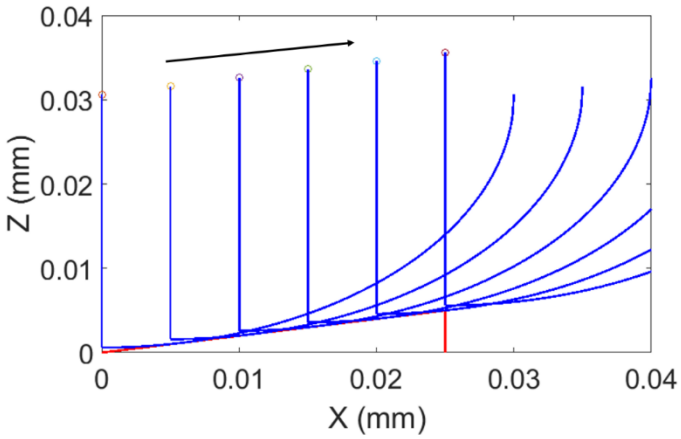

Figure 5.2 Matlab simulated tool path for Step I, where the tool is cutting the grating along its profile.

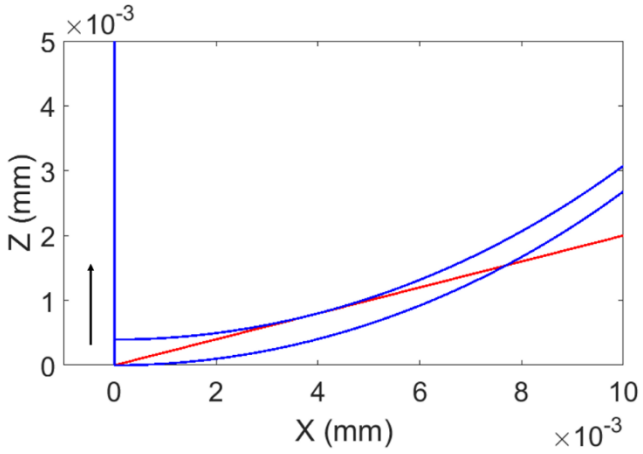

Figure 5.3 Matlab simulated tool path for Step II, where the tool is plunged into the bottom of the grating and moved out until it is tangent to the grating profile.

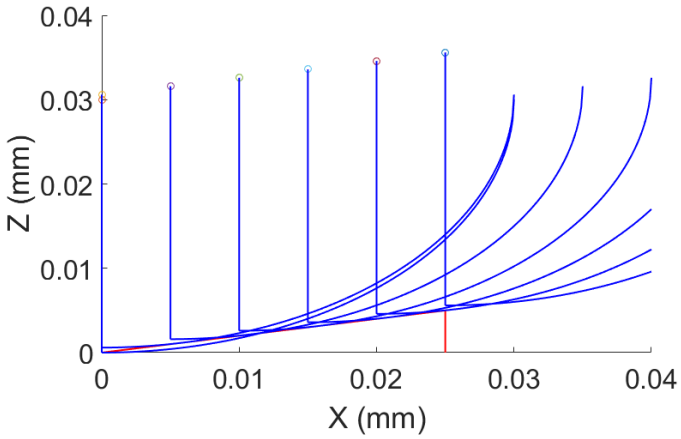

Figure 5.4 Matlab simulated tool path for one period of the grating by combining Step I and Step II.

5.1.2 Diamond turning fabrication of circular blazed gratings

Once we have generated the tool path for circular blazed gratings from Matlab as discussed in previous section, we can apply the tool path to the diamond turning machine and cut the gratings. In this section, we show an example of fabricating a circular blazed grating with the groove spacing of 25 um, step height of 1.5 um, with the diamond tool radius of 31 um, spindle speed of 2000 RPM, and the feed rate of 2 mm/min. Figure 5.5 shows the measurement result of the grating by the Zygo Newview optical profilometer. We can see from Figure 5.5 that the actual step height and the groove spacing match well with the design specifications. However, there are still some small discrepancies between the actual and ideal values. This may be caused by two possible reasons. The first reason is that the half radius diamond tool is not perfectly aligned to be perpendicular to the spindle surface. Instead, it is tilted a very small amount either clockwise or counterclockwise. When we do the plunge cut with this improper tool setting, the tilted portion of the half radius diamond tool can remove extra materials of the vertical walls of the grating, causing

the vertical walls to be slightly tilted and the step height slightly less than the designed value. More details about the simulation of the grating surface topography with respect to the half radius diamond tool orientation will be studied in Section 5.2. The second reason is because the half radius diamond tool is so sharp that it is also very fragile, and the diamond tool tip might crack during the cutting process. Once the diamond tool tip is cracked, the diamond tool cannot generate the correct step height because the tool will undercut the surface.

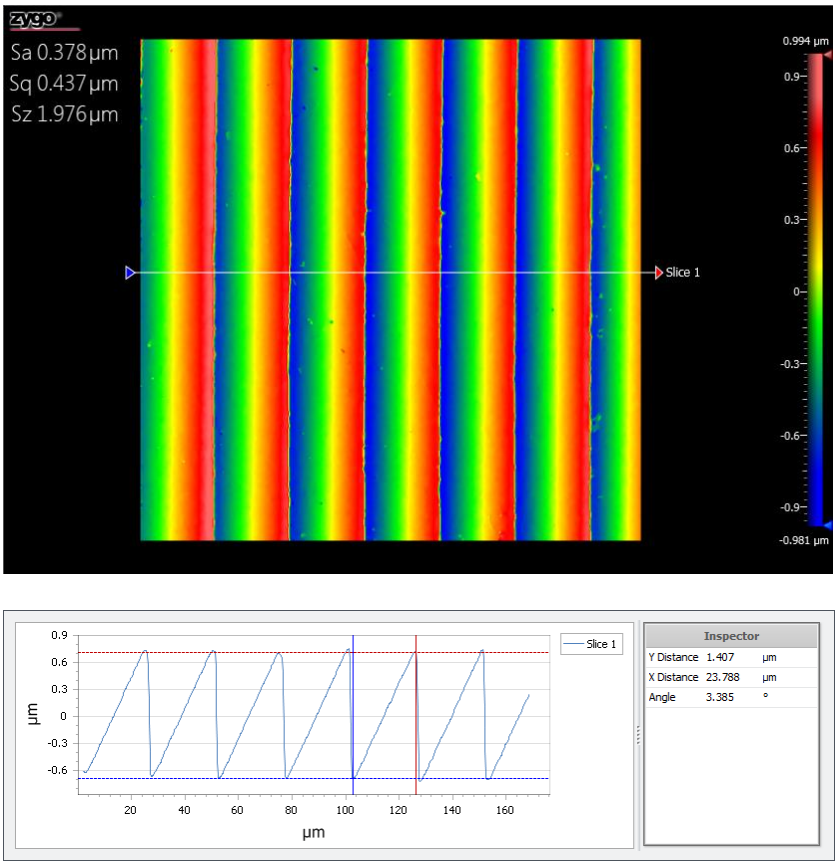

Figure 5.5 Measurement result of the blazed gratings generated with the proposed tool path.

5.2 Modeling of the diamond turned circular blazed gratings

5.2.1 Modeling of the gratings generated by the proposed tool path

In this section, we present a simulation for the grating surface topography in order to have a better understanding of the performance and efficiency of the diamond turned circular blazed gratings. Based on the two-step tool path to cut the gratings, we can simulate the surface topography by trimming the unwanted diamond tool profiles shown in Figure 5.4 and get the diamond turned grating profile. The simulation of this grating surface is shown in Figure 5.6. In Figure 5.6, the groove spacing is set as 10 um with the step height of 1 um, diamond tool radius of 20 um, and feed rate of 1 um per revolution for a clearer demonstration. The solid red line shows the ideal grating profile, and the solid black curve shows the simulated diamond turned grating profile. It can be seen that due to the first step of plunge cut, the diamond tool will overcut the grating. For the successive tool paths, the diamond tool will move along the grating surface and create a smooth tool mark.

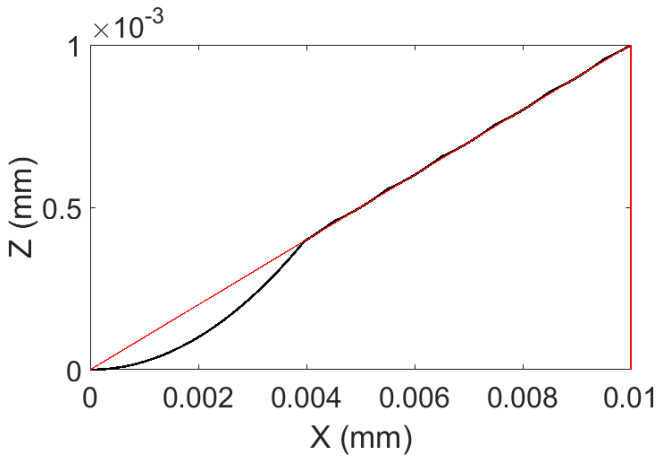

Figure 5.6 Simulation of the diamond turned grating profile. The solid red line shows the ideal grating profile, and the solid black curve shows the simulated diamond turned grating profile.

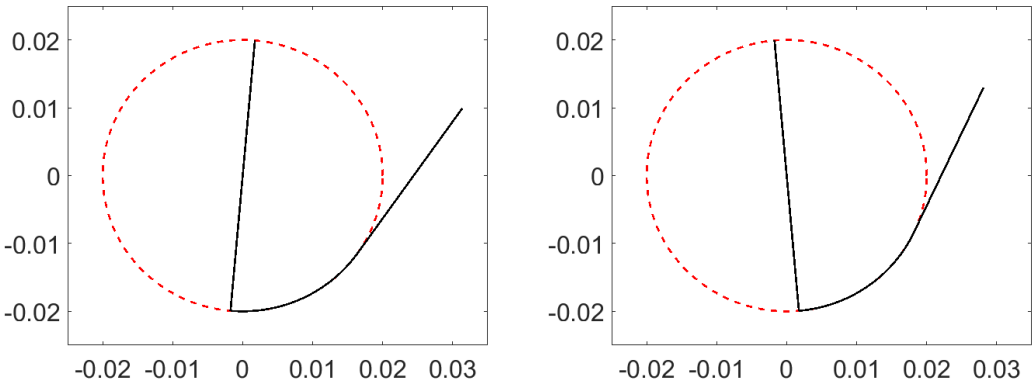

(a) (b)

Figure 5.7 (a) The half radius diamond tool tilted clockwise by 5° and (b) tilted counterclockwise by 5° with respect to the spindle axis. Units are in mm.

As discussed in Section 5.1.2, the actual cutting results tend to have smaller step heights than the ideal design value due to the orientation of diamond tool. As a result, we need to consider the diamond tool orientation in our simulation. The diamond tool can either be tilted clockwise or counterclockwise with respect to the spindle axis. Figure 5.7(a) and (b) show these two conditions respectively with the diamond tool radius of 20 um, including angle of 60°, and the tilt angle of 5°.

When the diamond tool is tilted clockwise by, for example, 5°, the sweep angle of that tool will change from the original 0° - 60° to -5° - 55°. As a result, if we use the same tool path setting with this tilted diamond tool to cut the grating, the -5° - 0° portion of the diamond tool will cut into the vertical side wall of the grating, removing portion of the grating and at the same time, leaving the -5° - 0° portion of the diamond tool profile at the bottom of the grating it removed. The tool path for this condition is shown in Figure 5.8, and the diamond turned grating profile is shown as blue dashed curve in Figure 5.9.

On the other hand, when the diamond tool is tilted counterclockwise by, for example, 5°, the sweep angle of that tool will change from the original 0° - 60° to 5° - 65°. If we use the same tool path setting with this tilted diamond tool to cut the grating, three cases will happen. First, because the 0° portion is not included in the tilted diamond tool anymore, we can never cut to the bottom of the grating. Instead, we can only reach the R-R*cos(5°) point, where R is the radius of curvature of the diamond tool. Second, because the flat portion of the half radius diamond tool is also tilted by 5°, this flat surface will cut the grating vertical wall and create a 5° tilted side wall. Third, at the end of the first period of the original tool path setting, the half radius diamond tool tip will move to the top of the grating profile to do the plunge cut for the next grating profile. Since the actual diamond tool is tilted counterclockwise by 5°, it means that the highest point of the grating will be shifted in X direction from the original 10 um position to about 10+ R*sin(5°) um provided that the step height is small compared to the diamond tool radius. Besides, the top of the grating will also change in Y direction from 1 um to 1+m* R*sin(5°), where m is the slope of the grating. Figure 5.10 shows the detailed procedure for generating the diamond turned grating profile with the diamond tool tilted counterclockwise. In Figure 5.10(a), the black dotted curve shows the diamond tool location for a tool without any tilt, the red dashed curve shows the actual diamond tool that is tilted counterclockwise by 5°, and the solid blue curve shows the actual tool position after the plunge cut for the next period of grating. The red arrow indicates the portion of the grating that is not removed properly by the tilted diamond tool. This portion of the grating should be totally removed if the diamond tool is not tilted. Figure 5.10(b) shows the full tool path for cutting one period of grating with

diamond tool tilted counterclockwise. The corresponding diamond turned grating profile is shown as red dotted curve in Figure 5.9. For both the clockwise and counterclockwise conditions, the topography for the successive tool paths along the grating will not be influenced. This is because in this example, the diamond tool cutting point for the grating occurs at arctan(0.001/0.01)=5.71°, which is just outside of the 5° tilt angle and is included in the diamond tool sweep angle in both conditions.

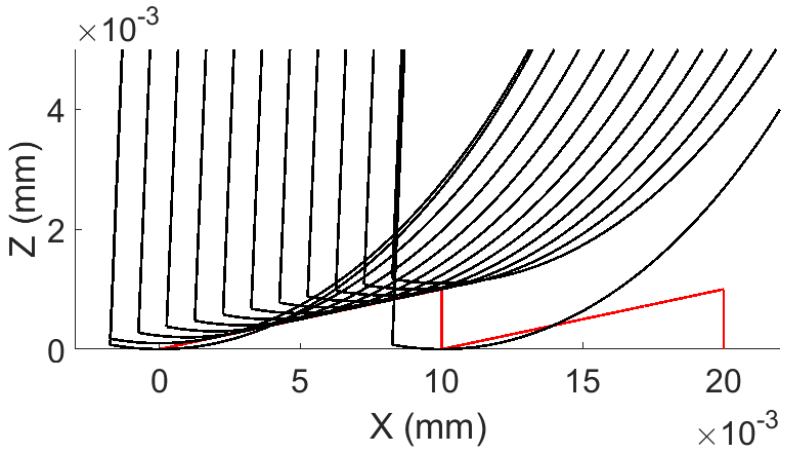

Figure 5.8 The tool path for cutting one period of grating with diamond tool tilted clockwise.

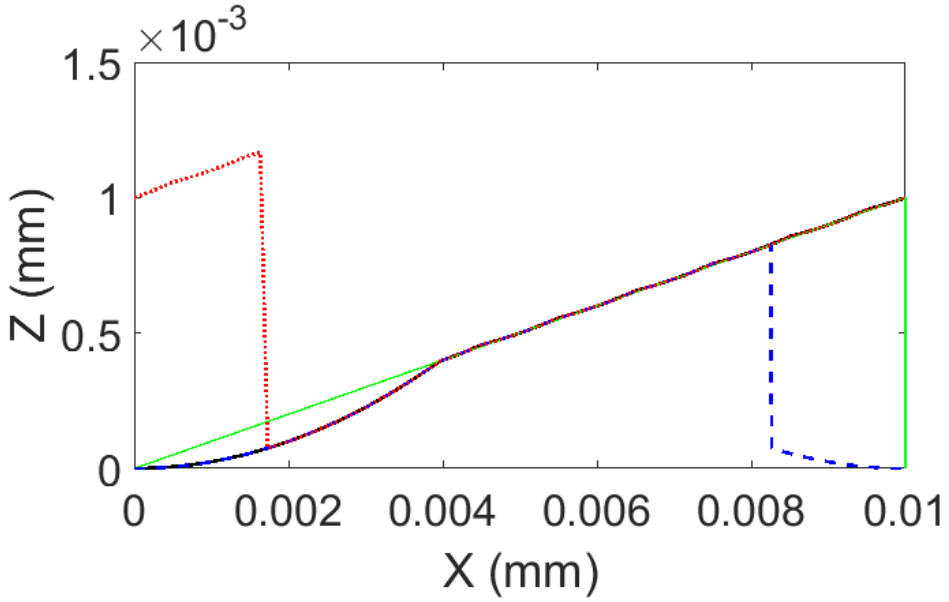

Figure 5.9 Simulation of the diamond turned grating surface with the consideration of diamond tool orientation. The solid green line shows the ideal grating profile, and the solid black curve shows the simulated diamond turned grating profile without diamond tool tilt. The blue dashed curve shows the grating profile with the diamond tool tilted clockwise by 5°, and the red dotted curve represents the grating profile with the diamond tool tilted counterclockwise by 5°.

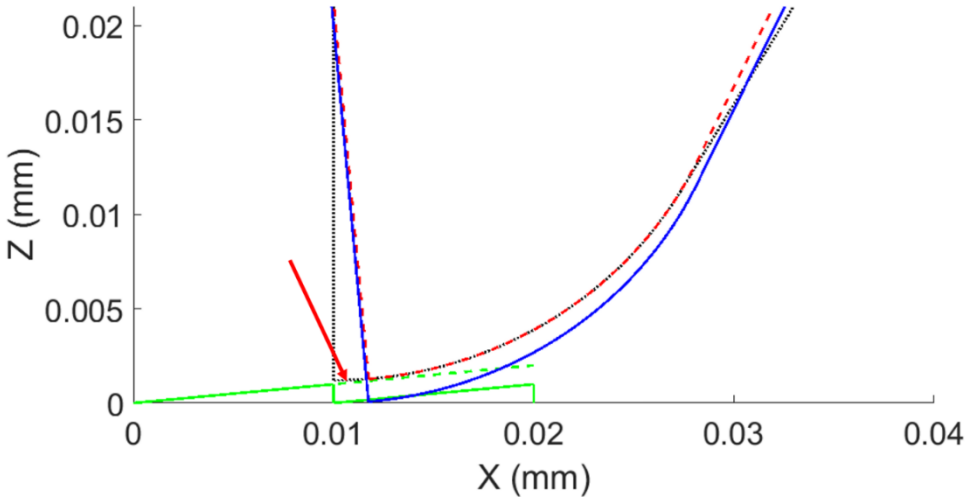

(a)

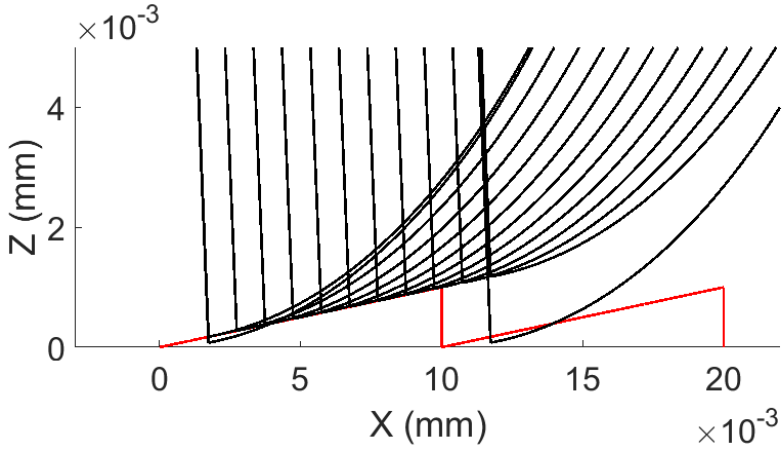

(b)

Figure 5.10 (a) Detailed procedure for generating the diamond turned grating profile with the diamond tool tilted counterclockwise. The black dotted curve shows the diamond tool location for a tool without any tilt, the red dashed curve shows the actual diamond tool that is tilted counterclockwise by 5°, and the solid blue curve shows the actual tool position after the plunge cut for the next period of grating. The red arrow shows the portion of the grating that is not removed by the tilted diamond tool after plunge cut. (b) The tool path for cutting one period of grating with diamond tool tilted counterclockwise.

Since the grating profile in Figure 5.9 shows only one period, when we tile this profile multiple times, we can generate the whole diamond turned blazed grating profile. Figures 5.11(a), (b), and (c) show the complete topography for the blazed grating with the consideration of perfect diamond tool, diamond tool tilted clockwise by 5°, and diamond tool tilted counterclockwise by 5°, respectively. We can observe that although in Figure 5.11(a) there will be overcut of the grating due to the plunge cut, the grating step height is maintained in this case. However, when the diamond tool is tilted clockwise as in Figure 5.11(b), the grating step height will be less than the ideal value and the grating profile is greatly deformed. As for the counterclockwise case, it is interesting to note that although the diamond tool cannot cut to the bottom of the grating, which will cause a loss of step height, the portion of the grating that is not properly removed by the tilted diamond tool (Red arrow in Figure 5.10(a)) can actually increase the step height to compensate for this loss. And the final step height can be roughly estimated as

$$\boldsymbol{H - \left(R - Rcos(5^{\circ})\right) + mRsin(5^{\circ})} \qquad (\mathbf{5.1})$$

where H is the step height. In out example, the final step height is 1.098 um instead of 1 um.

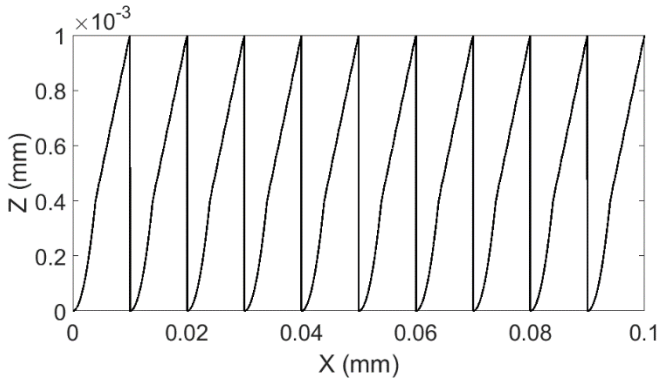

(a)

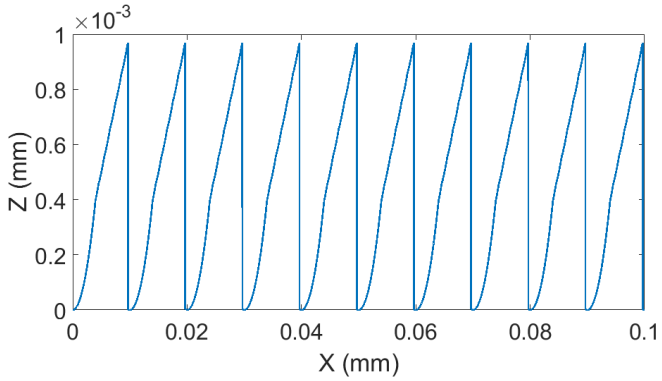

(b)

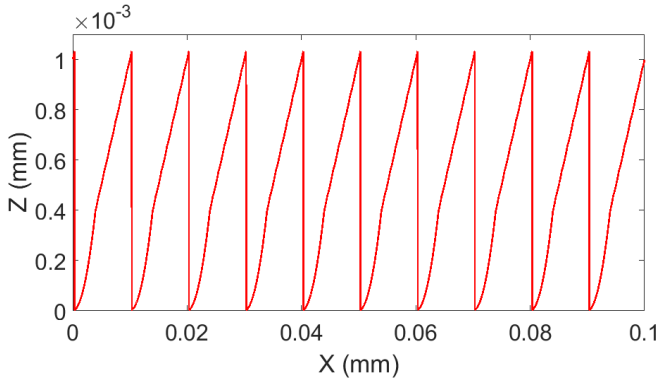

(c)

Figure 5.11 Complete topography for the blazed grating with the consideration of (a) no tilt for the diamond tool, (b) diamond tool tilted clockwise by 5°, and (c) diamond tool tilted counterclockwise by 5°.

5.2.2 Modeling of the gratings generated by NanoCAM2D

In previous section, we provide the simulation of the grating profiles generated by the tool path that we proposed in Section 5.1. However, it is also important to acquire a grating profile generated by the commercial software, which is NanoCAM2D in our case, and compare the performance of the two cases. Therefore, in this section, we present the model for the blazed grating based on the tool path generated by NanoCAM2D. As shown in Section 5.1, this kind of tool path tends to undercut the grating profile, and the main difference from the proposed tool path is the absence of the plunge cut to the bottom of the grating. Figure 5.12 shows the tool path provided by NanoCAM2D for cutting one period of grating. Figures 5.12(a), (b), and (c) demonstrate the cases without diamond tool tilt, with diamond tool tilted clockwise, and with diamond tool tilted counterclockwise, respectively. Figure 5.13 gives the corresponding diamond turned grating profiles for the three cases.

From Figure 5.12, we can observe that, despite the absence of the plunge cut to the bottom of the grating, they are having the same trends as in Figure 5.9. The grating profile is greatly deformed and step height greatly reduced for the case with the diamond tool tilted clockwise. However, for the counterclockwise case, the loss of step height due to the missing of the 0° diamond tool profile is compensated by the extra grating profile that is not properly removed by the plunge cut.

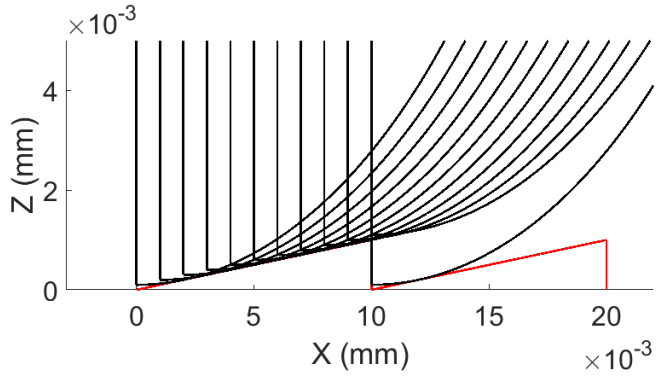

(a)

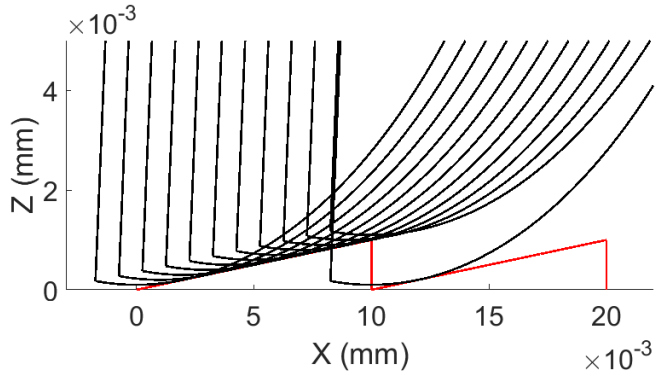

(b)

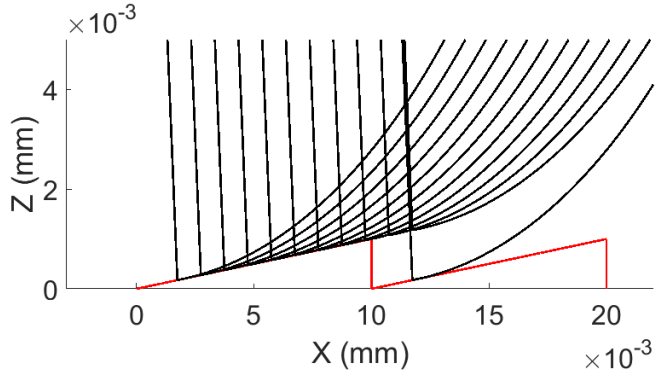

(c)

Figure 5.12 The tool path provided by NanoCAM2D for cutting one period of grating. (a) No tilt for diamond tool, (b) diamond tool is tilted clockwise, and (c) diamond tool is tilted counterclockwise.

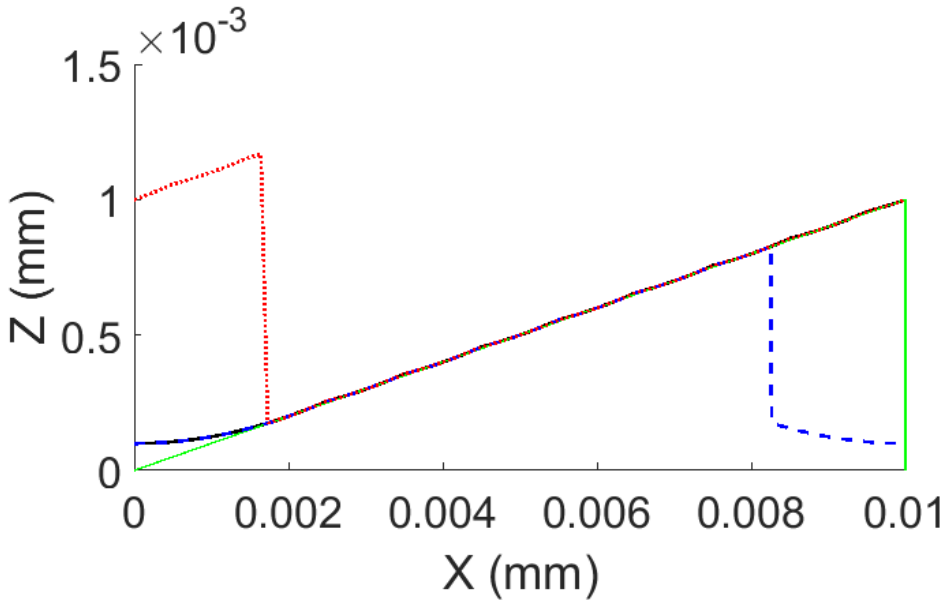

Figure 5.13 Simulation of the diamond turned grating surface generated with the tool path from NanoCAM2D with the consideration of diamond tool orientation. The solid green line shows the ideal grating profile, and the solid black curve shows the simulated diamond turned grating profile without diamond tool tilt. The blue dashed curve shows the grating profile with the diamond tool tilted clockwise by 5°, and the red dotted curve represents the grating profile with the diamond tool tilted counterclockwise by 5°.

5.3 Diffraction efficiency calculation for the diamond turned blazed gratings

Once we have the model for diamond turned circular blazed grating, it is straightforward to calculate its diffraction efficiency. For simplicity, we restrict our analysis on the YZ plane and assume the grating is put on the Y axis and has a transmission function of t(y). If the period of the grating is T, the transmission function of the grating has the property of $\mathbf{t(y) = t(y + T)}$, and it can be expressed as a Fourier series

$$\boldsymbol{t(y) = \sum_{m=-\infty}^{\infty} A_m e^{i2\pi m f_0 y}} \qquad \mathbf{(5.2)}$$

where $\mathbf{f_0} = \frac{\mathbf{1}}{\mathbf{T}}$ is the spatial frequency of the grating and

$$A_m = \frac{1}{T}\int_0^T t(y)\, e^{-i2\pi m f_0 y} dy \qquad (5.3)$$

are the Fourier coefficients.

Now we have an incident plane wave $\mathbf{U_i}$ on the z=0 plane traveling along the YZ plane with an angle of $\boldsymbol{\theta_i}$ with respect to Z axis such that

$$U_i(y, z = 0) = e^{\frac{i2\pi}{\lambda/n} y sin\theta_i} \qquad (5.4)$$

where $\boldsymbol{\lambda}$ is the wavelength in vacuum, n is the refractive index on illumination side.

When this plane wave travels through the grating, the transmission wave can be described by

$$U_t(y, z = 0) = U_i(y, z = 0) t(y)$$

$$= e^{\frac{i2\pi}{\lambda/n} y sin\theta_i} \sum_{m=-\infty}^{\infty} A_m e^{i2\pi m f_0 y}$$

$$= \sum_{m=-\infty}^{\infty} A_m e^{i2\pi y\left(\frac{sin\theta_i}{\lambda/n} + m f_0\right)}$$

$$= \sum_{m=-\infty}^{\infty} A_m e^{i2\pi y\left(\frac{sin\theta_o}{\lambda/n'}\right)} \qquad (5.5)$$

where $\boldsymbol{\theta_0}$ is the angle of refraction, and $\mathbf{n'}$ is the refractive index on observation side.

The last line of Equation 5.5 can be thought of as a series of plane waves, and the traveling angle of each plane wave satisfies

$$\frac{sin\theta_o}{\lambda/n'} = \frac{sin\theta_i}{\lambda/n} + m f_0 \qquad (5.6)$$

which is the grating equation.

From Equation 5.5 we know that the diffraction field is composed of a series of plane waves which are traveling with the angle determined by the grating equation. The amplitude of each plane wave is represented by its Fourier coefficient $\mathbf{A_m}$. Diffraction efficiency $\boldsymbol{\eta_m}$ is the input energy that is transferred to the $\mathbf{m^{th}}$ order, which is represented by

$$\boldsymbol{\eta_m = A_m A_m^*} \qquad (\mathbf{5.7})$$

where $\mathbf{A_m^*}$ is the complex conjugate of $\mathbf{A_m}$.

From Equations 5.6 and 5.7, we can see two important characteristics of the diffraction gratings, that is, the spatial frequency of the grating determines the travel angle for different orders of diffraction waves, and the transmission function of the grating determines the diffraction efficiency for each diffraction order.

Now if we have a blazed grating with the phase changing from 0 to the maximum $\boldsymbol{\alpha 2\pi}$ in one period, we can get the diffraction efficiency from Equation 5.7

$$\boldsymbol{\eta_m = sinc^2(\alpha - m)} \qquad (\mathbf{5.8})$$

If $\boldsymbol{\alpha = 1}$ in Equation 5.8, then $\boldsymbol{\eta_1 = 1}$, and all other $\boldsymbol{\eta_m = 0}$. In this case, we have a blazed grating with 100% diffraction efficiency, and all the incident light goes to the first order diffraction. Because of its simplicity, we will focus our analysis in this section to the blazed grating with phase change from 0 to $\boldsymbol{2\pi}$.

With the blazed grating, we know that the Optical Path Difference (OPD) is

$$\boldsymbol{\big(n'(\lambda) - n(\lambda)\big)d(y)} \qquad (\mathbf{5.9})$$

where $\mathbf{d(y)}$ is the step height of the grating.

As a result, the phase function is

$$\boldsymbol{\frac{2\pi}{\lambda}\big(n'(\lambda) - n(\lambda)\big)d(y)} \qquad (\mathbf{5.10})$$

For the blazed grating, the step height is chosen such that it has a $\mathbf{2\pi}$ phase change at the maximum step height $\boldsymbol{d_{max}}$

$$\frac{\mathbf{2\pi}}{\boldsymbol{\lambda}}\big(\boldsymbol{n'(\lambda) - n(\lambda)}\big)\boldsymbol{d_{max}} = \mathbf{2\pi} \qquad (\mathbf{5.11})$$

So

$$\boldsymbol{d_{max}} = \frac{\boldsymbol{\lambda}}{|\boldsymbol{n'(\lambda) - n(\lambda)}|} \qquad (\mathbf{5.12})$$

If, for simplicity, we further assume that $\boldsymbol{\lambda = 0.5}$ um, $\boldsymbol{n'(\lambda) = 1.5}$, and $\boldsymbol{n(\lambda) = 1}$ is in air, we can get $\boldsymbol{d_{max} = 1}$ um. These are the basic parameters used in our previous simulations for clearer demonstration of the results, but these parameters can easily be changed to other values that fit the specific applications.

In the simulation and calculation below, we again choose the groove spacing to be 10 um, step height of 1 um, $\boldsymbol{n(\lambda) = 1}$, $\boldsymbol{n'(\lambda) = 1.5}$, $\boldsymbol{\lambda = 0.5}$ um, half radius diamond tool radius of 20 um, spindle speed of 2000 RPM, and feed rate of 2 mm/min. We follow the steps in Section 5.2 to create four sets of blazed grating profiles, which are the ideal blazed grating, the diamond turned grating without diamond tool tilt, the diamond turned grating with diamond tool tilted clockwise from 0° to 5°, and the diamond turned grating with diamond tool tilted counterclockwise from 0° to 5°. Figure 5.14 shows the grating profile of the last two cases above with the tool path proposed in Section 5.1.

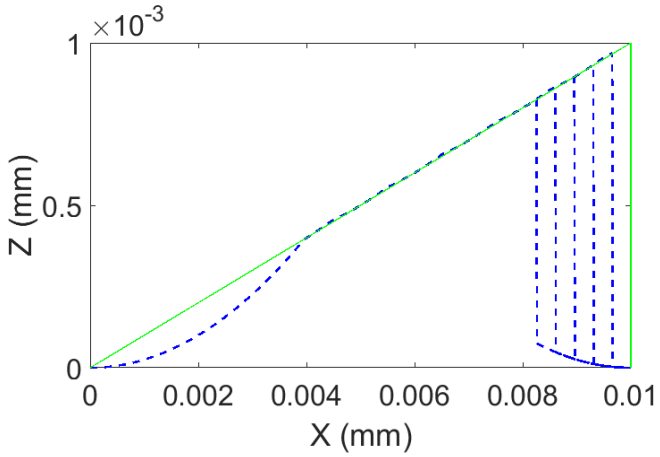

(a)

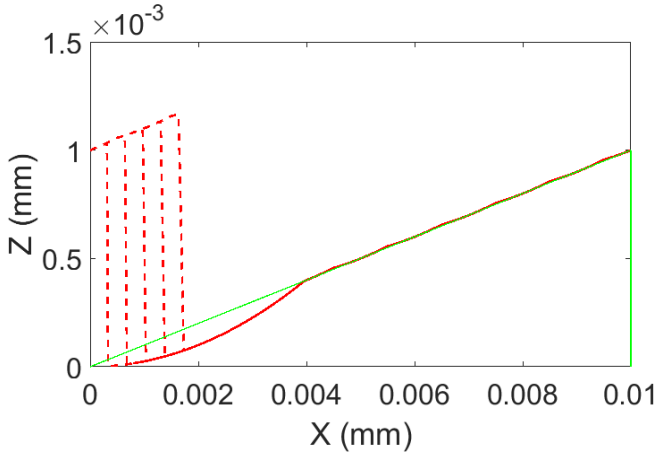

(b)

Figure 5.14 Diamond turned grating with the tool path proposed in Section 5.1 with (a) diamond tool tilted clockwise from 0 to 5°, and (b) with diamond tool tilted counterclockwise from 0 to 5°.

5.3.1 Diffraction efficiency calculation for the proposed gratings

With the grating profiles, we can obtain the diffraction efficiency by applying the Fourier transform to each grating profile and find the Fourier coefficient corresponding to $\mathbf{m = 1}$. Here we tile each grating profile in Figure 5.9 ten times to get the periodic structure. Figure 5.15 shows the diffraction efficiency for each set of the grating profile that is calculated from Equation 5.7. We can see that the diffraction efficiency for an ideal blazed grating reaches 100%, which matches Equation 5.8. On the other hand, the diffraction efficiency for diamond turned grating without any diamond tool tilt also reaches around 94%, which shows that using diamond turning machine to fabricate blazed grating is a promising method with low cost and high performance. Once we have introduced diamond tool tilt into the simulation, we can clearly see the diffraction efficiency decreases with increasing tool tilt angle, especially in the clockwise case. This is shown in Figure 5.15(c). However, this is not the case for the diamond tool tilted counterclockwise, as shown in Figure 5.15(d). In such a situation, because of the compensation effect of the step height as mentioned in Section 5.2 and Equation 5.1, the grating profile is very similar to Figure 5.15(b) where the diamond tool is not tilted. The most noticeable difference is that with the tool tilted counterclockwise, the grating side wall will be slightly tilted. The degree of side wall tilt is proportional to the diamond tool tilt angle.

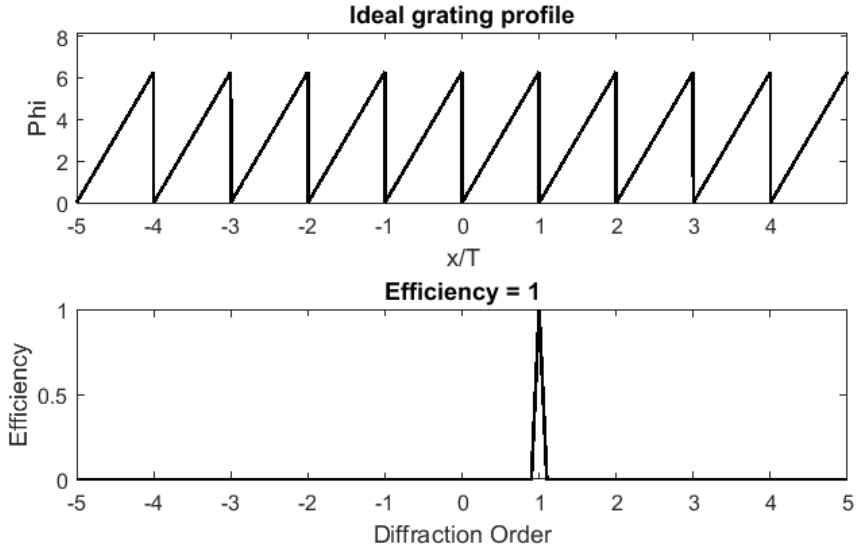
Ideal grating profile
Phi
x/T
Efficiency = 1
Efficiency
Diffraction Order

(a)

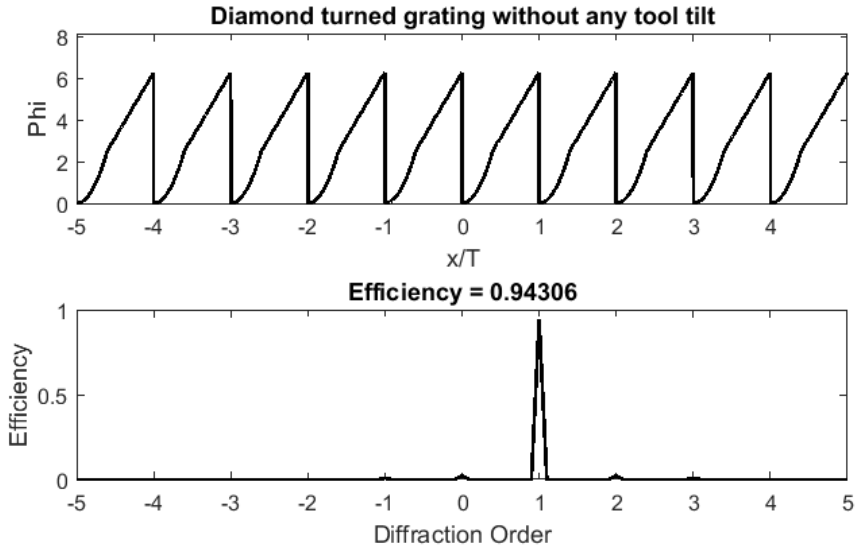
Diamond turned grating without any tool tilt
Phi
x/T
Efficiency = 0.94306
Efficiency
Diffraction Order

(b)

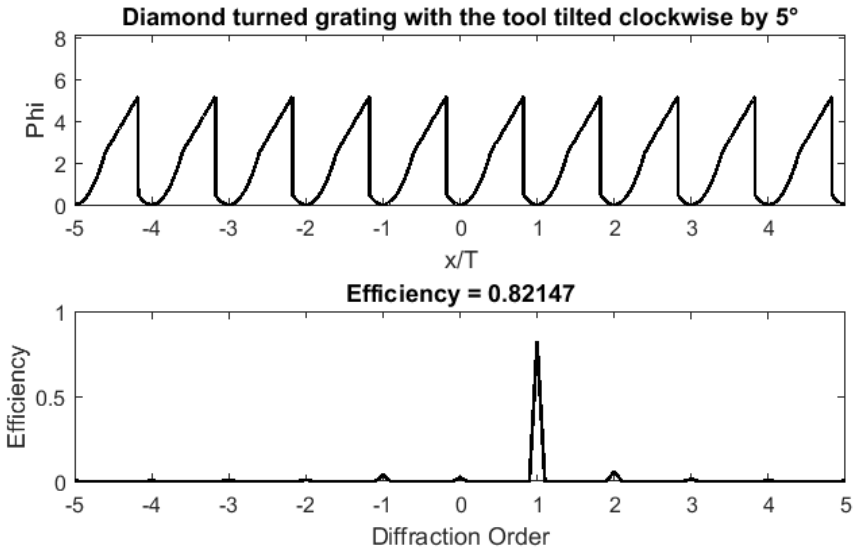

(c)

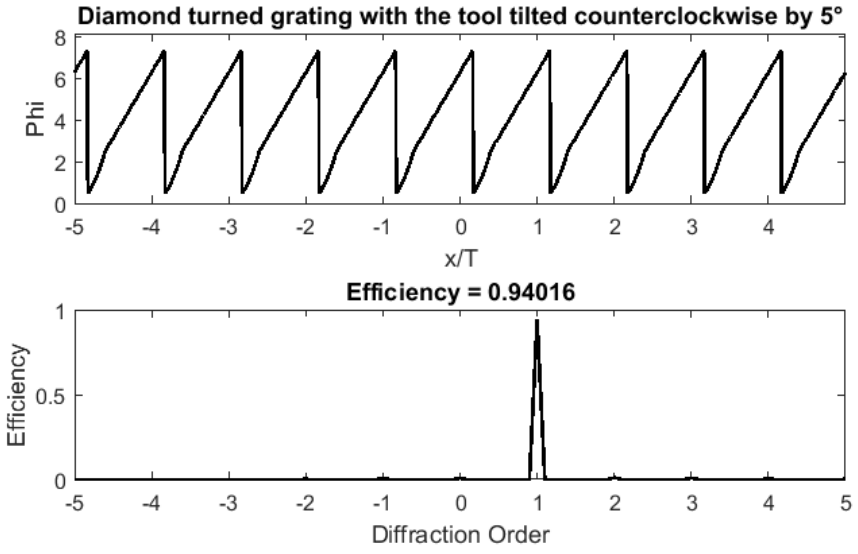

(d)

Figure 5.15 Diffraction efficiency for the proposed grating. (a) The ideal grating profile, (b) the diamond turned grating without any diamond tool tilt, (c) the diamond turned grating with the diamond tool tilted clockwise by 5°, and (d) the diamond turned grating with the diamond tool tilted counterclockwise by 5°.

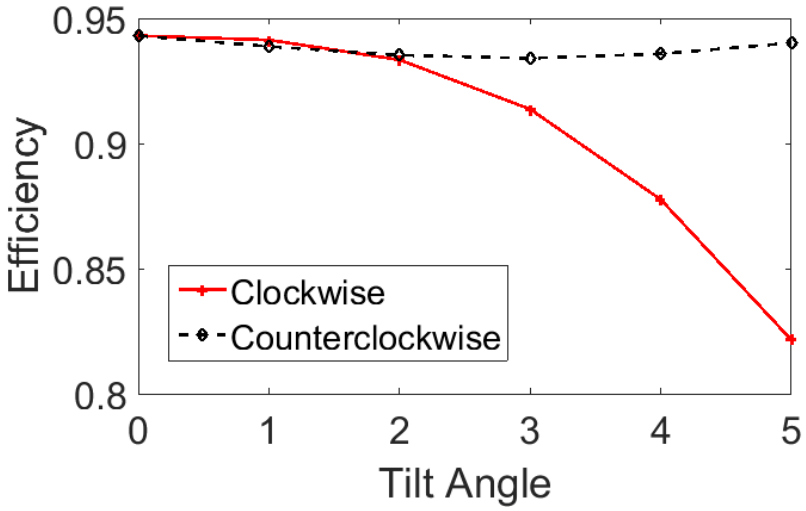

Figure 5.16 Diffraction efficiency of the blazed grating with respect to the diamond tool tilt angle. The red solid curve shows the case that the diamond tool is tilted clockwise, and the black dashed curve shows the case that the diamond tool is tilted counterclockwise.

Figure 5.16 plots the diffraction efficiency of the blazed grating with respect to the diamond tool tilt angle. The red solid curve shows the case that the diamond tool is tilted clockwise, and the black dashed curve shows the case that the diamond tool is tilted counterclockwise. It is clearly seen that the diffraction efficiency almost keeps constant when the diamond tool is tilted counterclockwise by a small angle, but the diffraction efficiency is significantly reduced when the tool is tilted clockwise

This model can provide us with very useful information for tolerancing analysis. It can provide an estimation of the range that the diamond tool is allowed to tilt in each direction during the alignment process before the diamond turning fabrication process. It can also show how different diamond tool radius can affect the surface profile of the blazed grating, and in turn influence the diffraction efficiency.

5.3.2 Diffraction efficiency calculation for the grating generated by NanoCAM2D

In this section, we show the diffraction efficiency of the grating generated by the tool path provided by NanoCAM2D. Figure 5.17 shows the diffraction efficiency for each set of the grating profile that is calculated from Equation 5.7, and Figure 5.18 shows the diffraction efficiency of the blazed grating with respect to the diamond tool tilt angle. When comparing Figure 5.17(b) with Figure 5.15(b), we can find that the tool path provided by NanoCAM2D tends to generate a blazed grating with higher diffraction efficiency than the proposed tool path. This is because the tool path provided by NanoCAM2D can generate a correct grating profile. In addition, when the diamond tool radius is small enough, the undercut issue is also very small and is negligible. On the other hand, although the tool path we proposed can generate a correct step height, it will at the same time create an overcut into the grating and therefore deform the grating profile.

It is interesting to note that, while the performance for the gratings generated by NanoCAM2D is better than that for the proposed tool path, the diffraction efficiency for the gratings generated by the proposed tool path is higher when the diamond tool is tilted clockwise. This can mainly be explained by the differences of the step height for the two cases. When we compare Figure 5.15(c) and Figure 5.17(c), we can see that Figure 5.15(c) has a greater step height due to the plunge cut into the bottom of the grating.

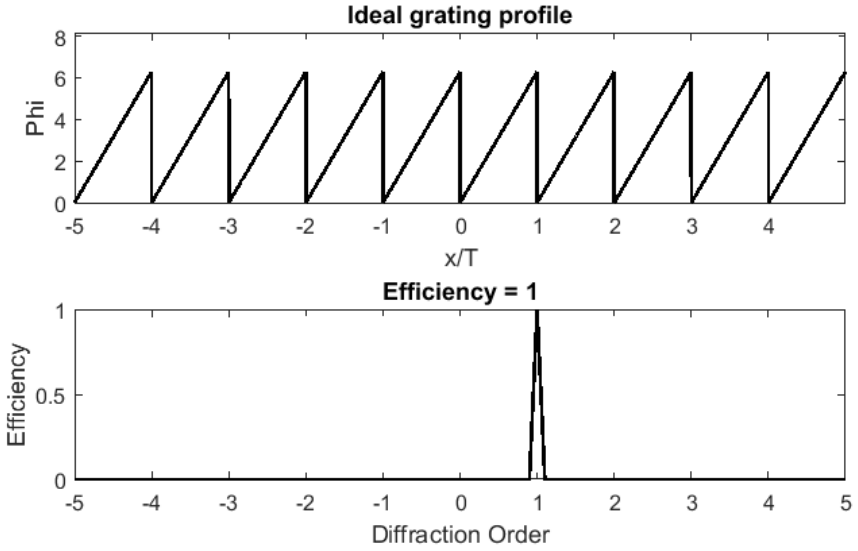
Ideal grating profile
Phi
x/T
Efficiency = 1
Efficiency
Diffraction Order

(a)

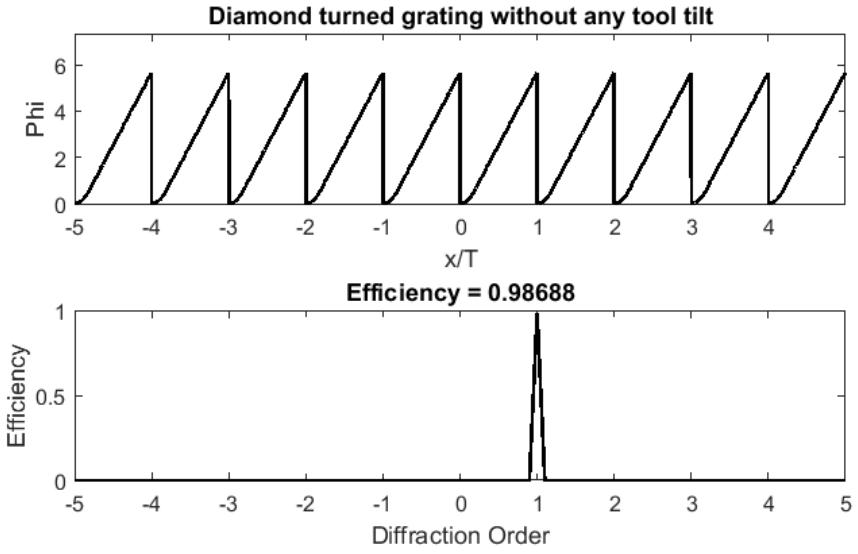
Diamond turned grating without any tool tilt
Phi
x/T
Efficiency = 0.98688
Efficiency
Diffraction Order

(b)

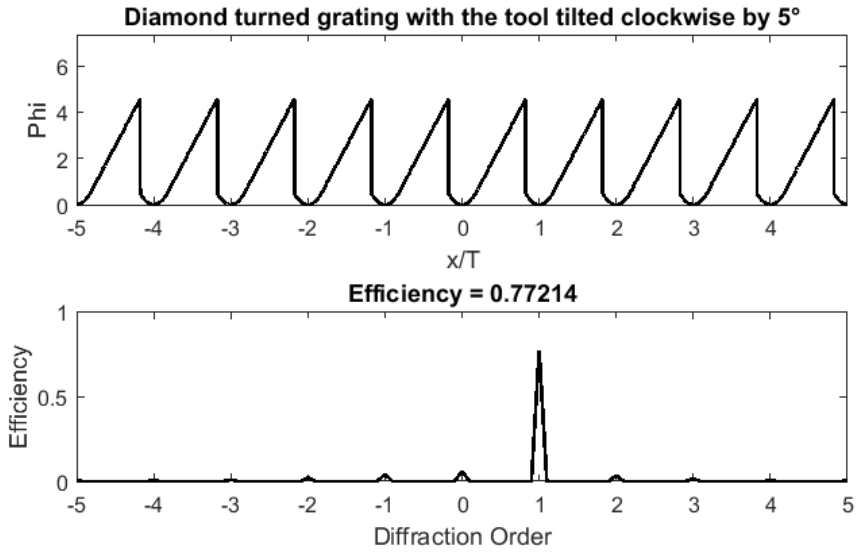

(c)

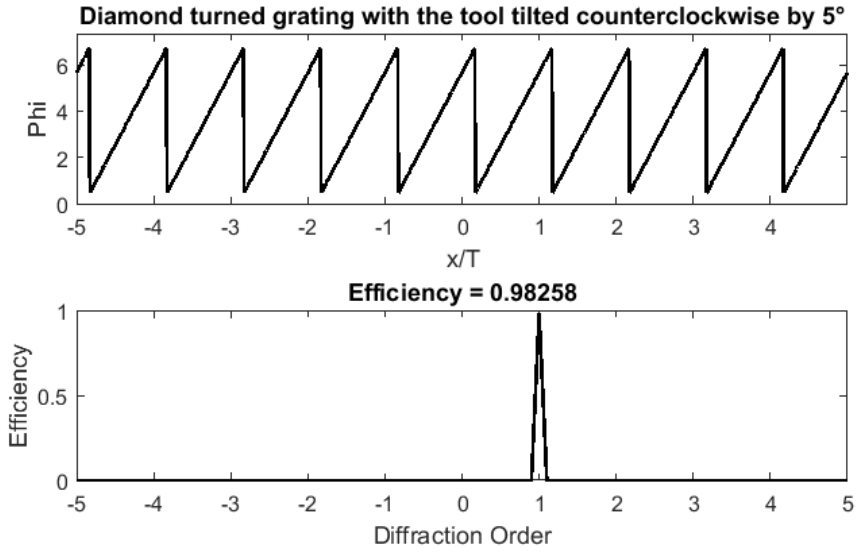

(d)

Figure 5.17 Diffraction efficiency for the gratings generated by NanoCAM2D. (a) The ideal grating profile, (b) the diamond turned grating without any diamond tool tilt, (c) the diamond turned grating with the diamond tool tilted clockwise by 5°, and (d) the diamond turned grating with the diamond tool tilted counterclockwise by 5°.

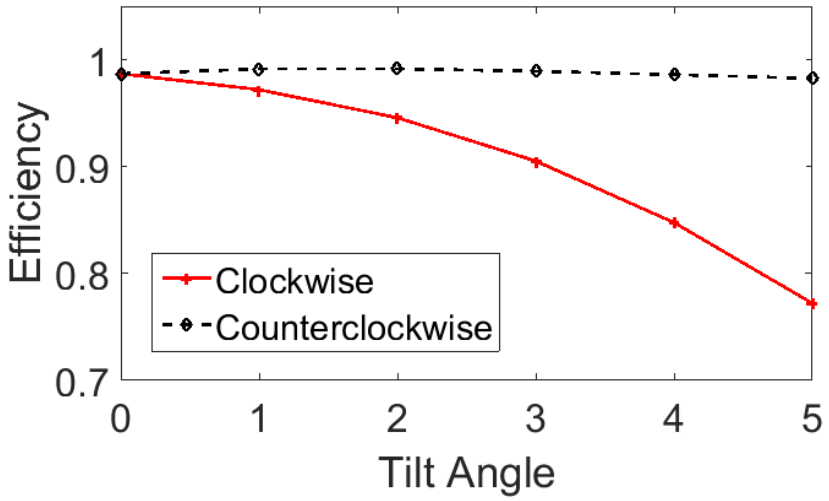

Figure 5.18 Diffraction efficiency of the blazed grating generated by NanoCAM2D with respect to the diamond tool tilt angle. The red solid curve shows the case that the diamond tool is tilted clockwise, and the black dashed curve shows the case that the diamond tool is tilted counterclockwise.

5.4 Experimental verification

In this section, we carry out a series of experiments to verify the model we proposed in Section 5.2. The experiment is divided into two parts. In the first part, we cut an arbitrary blazed grating to verify the grating profile obtained from the proposed model. In the second part, we design, fabricate, and test a circular blazed grating to verify the diffraction efficiency calculated from the model. Table 5.1 summarizes the cutting parameters for the two parts.

Table 5.1 Cutting parameters for the two parts.

Part	Spindle speed (RPM)	Feed rate (mm/min)	Depth of cut (um)	Tool Radius (mm)
I	2000	0.5	2	0.07
II	2000	0.5	2	0.03

5.4.1 Part I: verification of the proposed model

In the first part of the experiment, we diamond turn a blazed grating with the proposed tool path and the tool path generated by NanoCAM2D with the consideration of no tool tilt, tool tilted clockwise by 5°, and tool tilted counterclockwise by 5°, respectively. The groove spacing of the blazed grating is 25 um, and the step height is 2 um. In this cutting test, we use a half radius tool with tool radius of 70 um, and the diamond tool profile is shown in Figure 5.19. It is interesting to note that, although the half radius tool is newly relapped, the tool profile is not perfect. If we compare Figure 5.19 and Figure 5.7, we can see that for a perfect half radius diamond tool as in Figure 5.7, the sweep angle goes from 0° at the tool tip to 60° at the edge of the diamond tool. However, in Figure 5.19, the sweep angle at the tool tip is not 0°. Instead, it is a small negative value. This situation will influence the diamond turned grating profiles. As shown in Figure 5.20, we can view the half radius diamond tool profile as a combination of a perfect half radius tool with sweep angle from 0° to 60° and an extra tool profile from a negative sweep angle to 0°. Because the center of curvature is not changed due to the addition of the extra tool profile, the tool path generated by the proposed method and from NanoCAM2D will be the same as for the case for a perfect diamond tool.

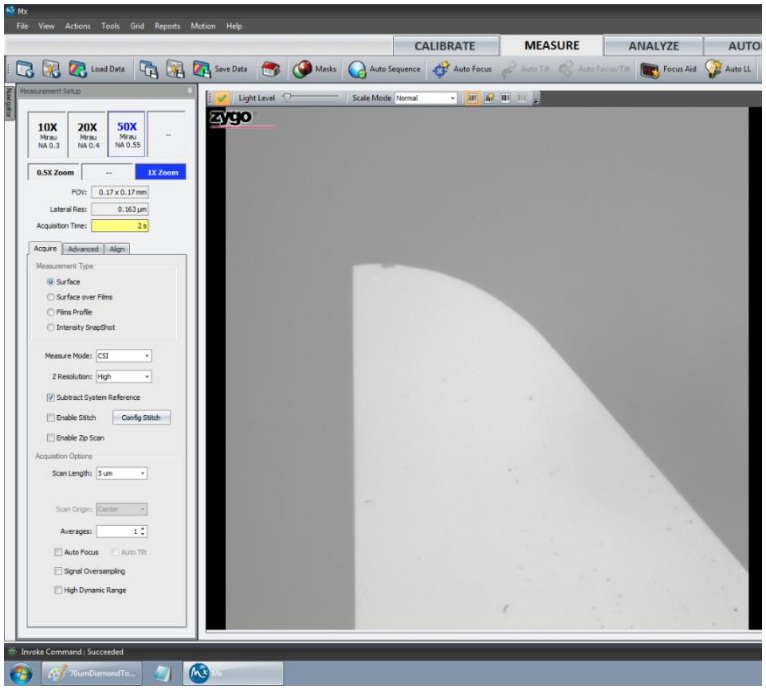

Figure 5.19 Tool profile of the 70 um half radius diamond tool.

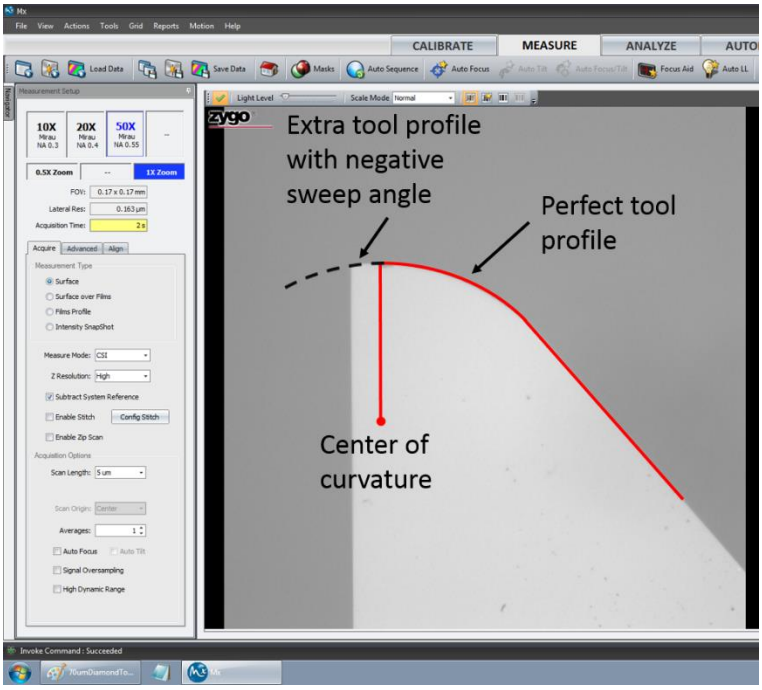

Figure 5.20 Diamond tool profile as a combination of a perfect diamond tool with sweep angle from 0° to 60° and an extra tool profile from a negative sweep angle to 0°.

Figure 5.21 shows the measurement results of the diamond turned blazed gratings generated by the proposed tool path with the consideration of the diamond tool orientation. Due to the extra tool profile with negative sweep angle, it will greatly influence the final grating profiles. In Figure 5.21(a), we can clearly see the overcut of the diamond tool into the grating profile as well as the extra tool profile that lies between the blue line and the red line in the figure. Because of the extra tool profile, a great portion of the grating profile was removed when we do the plunge cut, resulting in a reduced step height. This is verified if we substitute the imperfect diamond tool profile for the perfect one in Figure 5.4, as shown in Figure 5.22. When the tool is tilted clockwise by 5°, the extra tool profile again removed a great portion of the grating profile and significantly deformed the grating shape, as shown in Figure 5.21(b). On the other hand, when the tool is tilted counterclockwise, the extra tool profile with negative sweep angle is also rotated and becomes about 0°. As a result, the effect caused by the extra tool profile with negative sweep angle is greatly suppressed, and the resulting grating profile shown in Figure 5.21(c) is similar to Figure 5.10(b) where the perfect diamond tool is tilted counterclockwise.

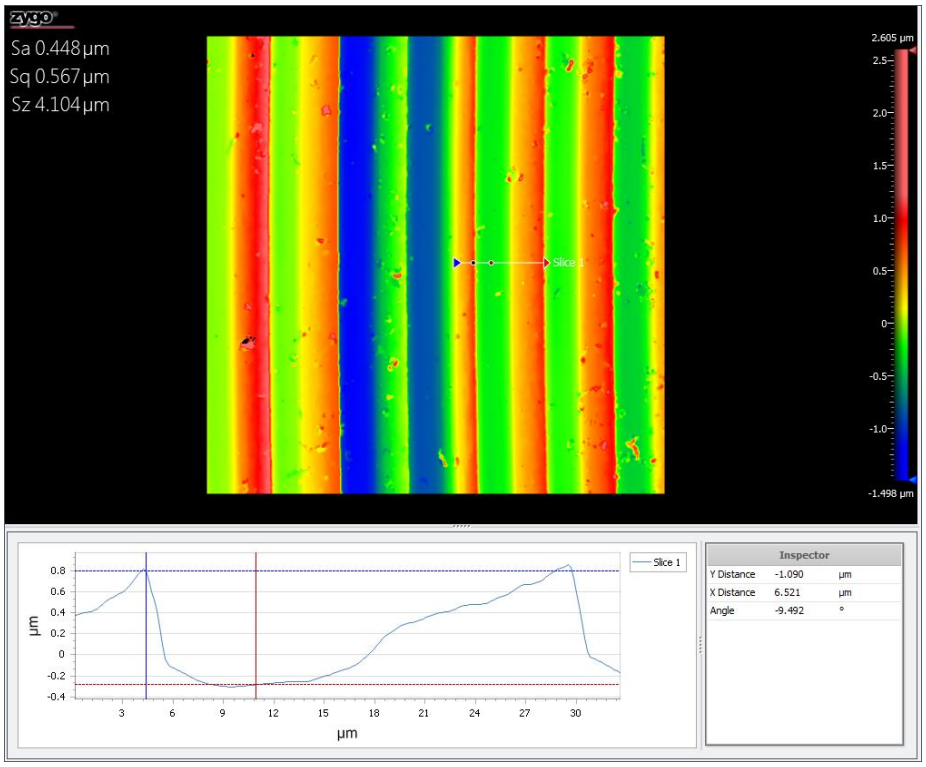
Sa 0.448 µm
Sq 0.567 µm
Sz 4.104 µm
2.605 µm
-1.498 µm
Slice 1
Inspector
Y Distance -1.090 µm
X Distance 6.521 µm
Angle -9.492 °
µm

(a)

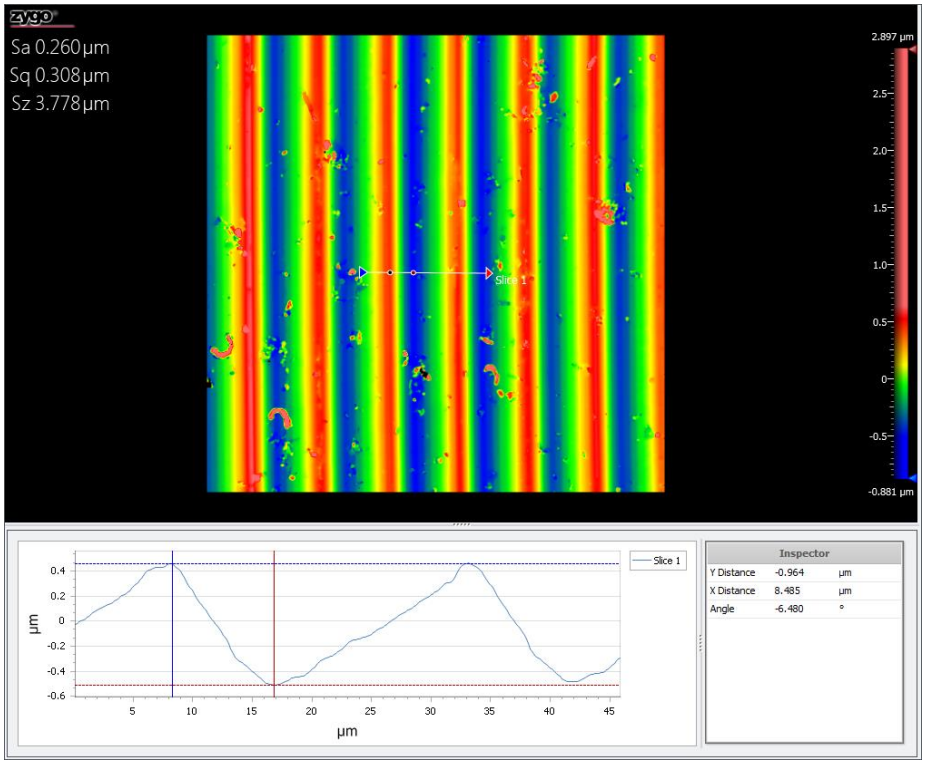
Sa 0.260 µm
Sq 0.308 µm
Sz 3.778 µm
2.897 µm
-0.881 µm
Slice 1
Inspector
Y Distance -0.964 µm
X Distance 8.485 µm
Angle -6.480 °
µm

(b)

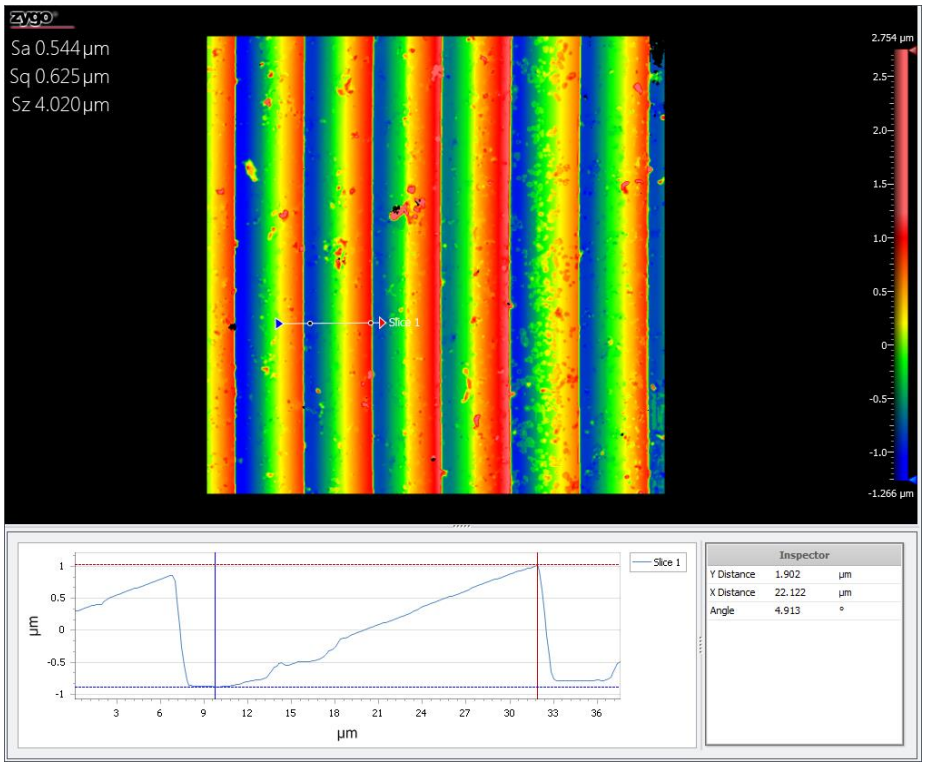

(c)

Figure 5.21 Measured blazed grating profiles generated by the proposed tool path. (a) without tool tilt; (b) tool tilted clockwise by 5°; (c)tool tilted counterclockwise by 5°.

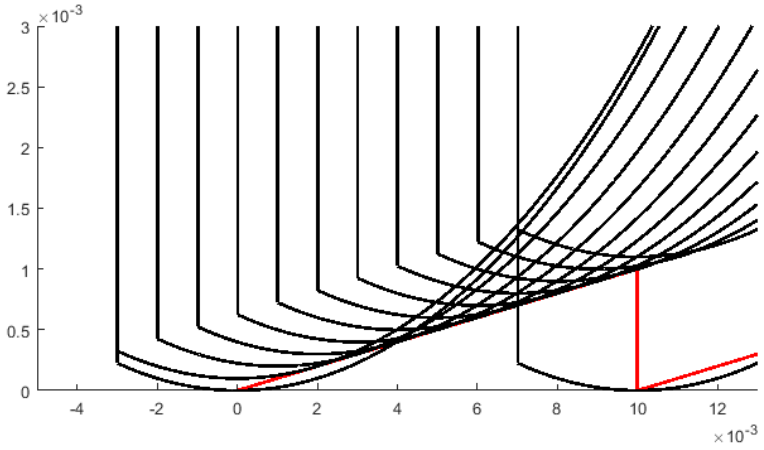

Figure 5.22 The tool path for cutting one period of grating with the consideration of imperfect diamond tool profile as shown in Figure 5.19.

Figure 5.23 shows the measurement results of the diamond turned blazed gratings generated by the tool path from NanoCAM2D with the consideration of the diamond tool orientation. The grating profiles in Figure 5.23 are similar to those in Figure 5.21. However, because of the absence of the plunge cuts to the bottom of the grating, we do not see any overcut issue in Figure 5.23. Without the plunge cut to the bottom of the grating, we would inevitably lose some step height in the grating profile. This is clearly seen in Figure 5.23(b) and (c).

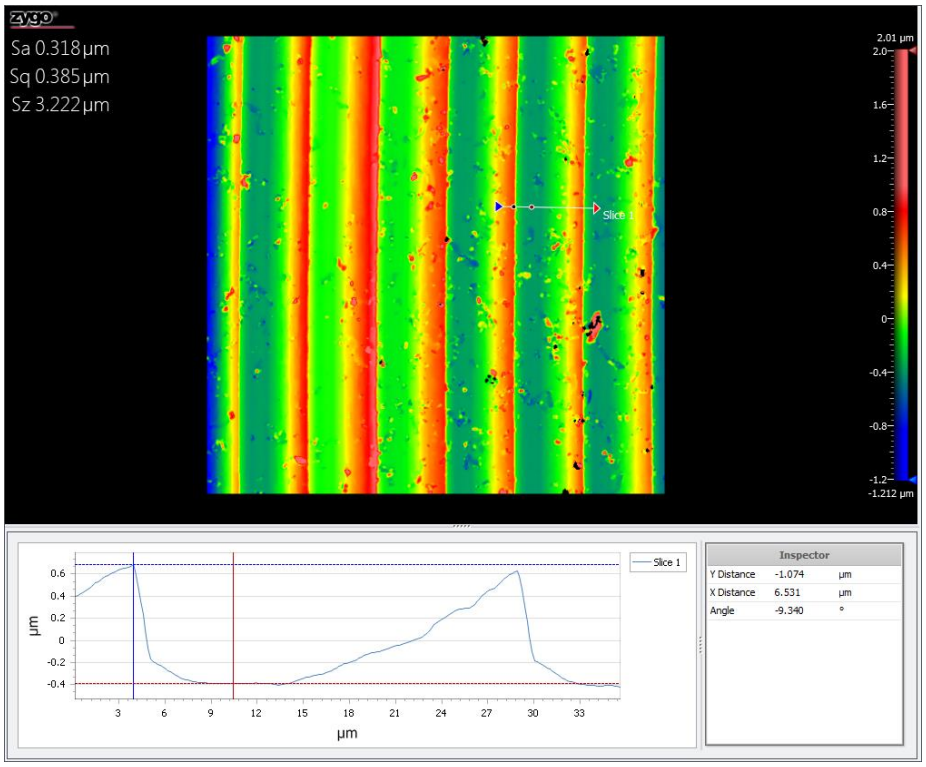
Sa 0.318 µm
Sq 0.385 µm
Sz 3.222 µm
2.01 µm
-1.212 µm
Slice 1
Inspector
Y Distance -1.074 µm
X Distance 6.531 µm
Angle -9.340 °
µm

(a)

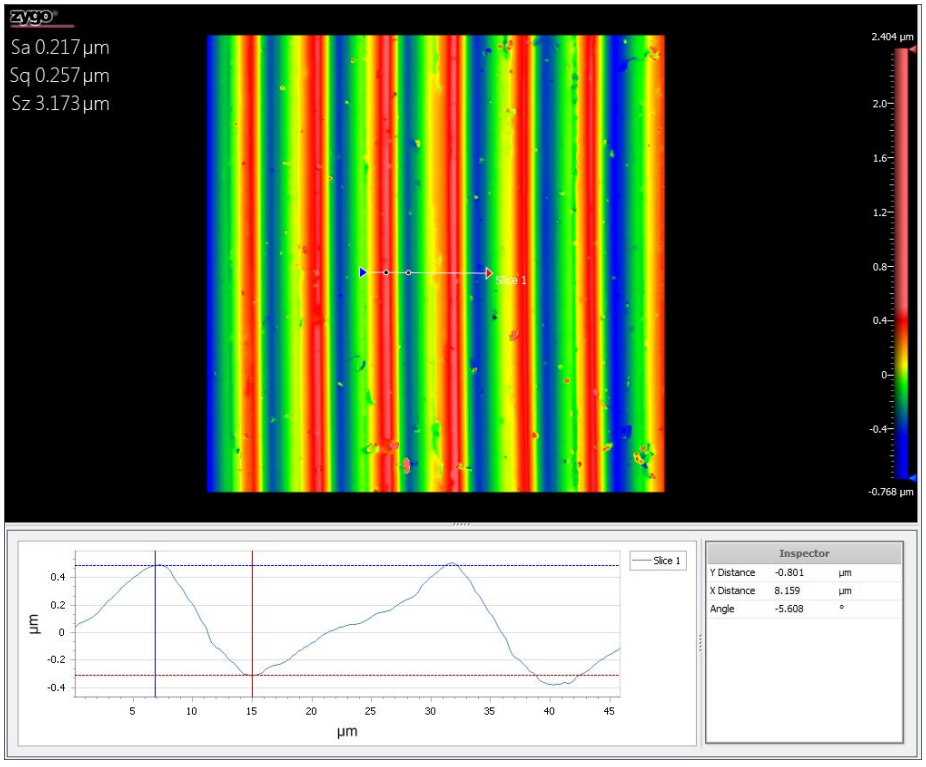
Sa 0.217 µm
Sq 0.257 µm
Sz 3.173 µm
2.404 µm
-0.768 µm
Slice 1
Inspector
Y Distance -0.801 µm
X Distance 8.159 µm
Angle -5.608 °
µm

(b)

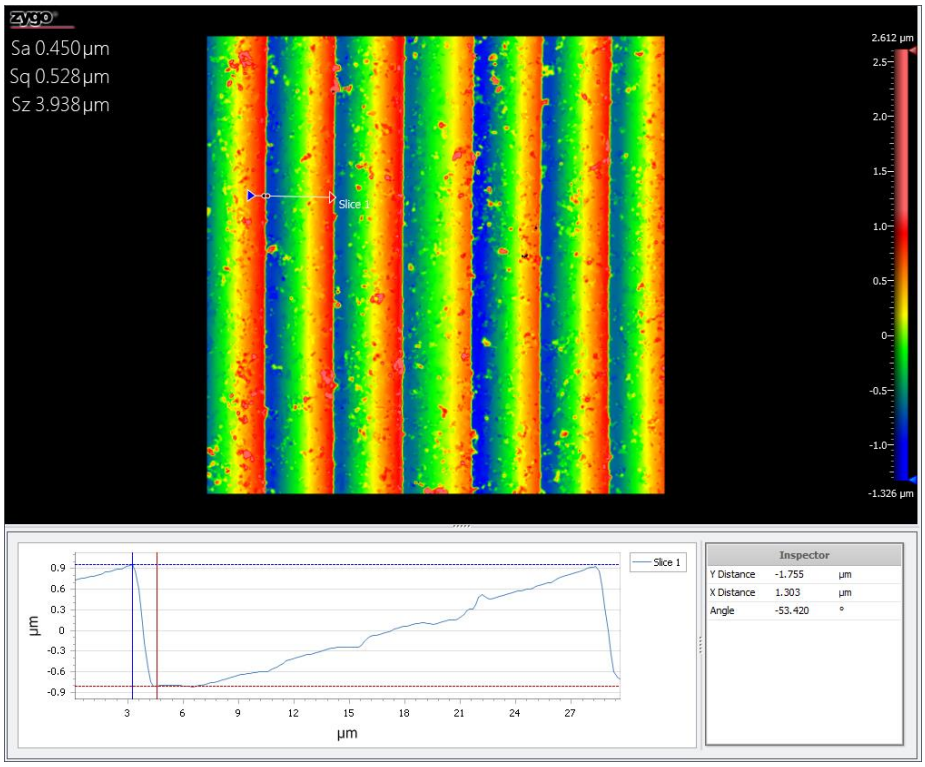

(c)

Figure 5.23 Measured blazed grating profiles generated by the tool path from NanoCAM2D. (a) without tool tilt; (b) tool tilted clockwise by 5°; (c)tool tilted counterclockwise by 5°.

5.4.2 Part II: verification of the diffraction efficiency

For the second part of the experiment, we design, fabricate, and test a circular blazed grating. The blazed grating is designed for the wavelength of 632.8 nm, and the grating material is PMMA. The refractive index of PMMA at the testing wavelength of 632.8 nm is measured to be 1.4892. When we apply these parameters to Equation 5.12, we can calculate the step height to be 1.2935 um. The groove spacing is set to be 12 um. In Part II of the experiment, we use a 30 um half radius diamond tool to cut the blazed gratings. Figure 5.24 shows the tool profile of the 30 um half radius diamond tool.

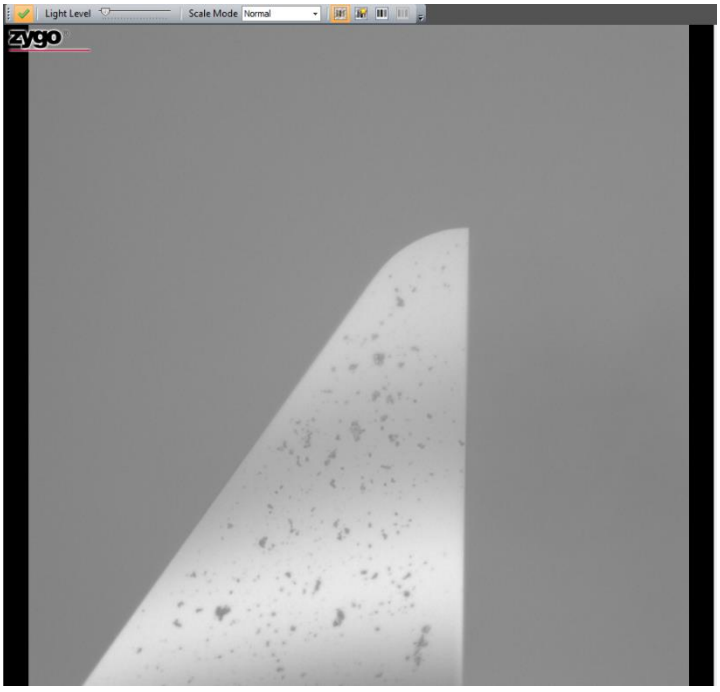

Figure 5.24 Tool profile of the 30 um half radius diamond tool.

With the experiences gained from Part I of the experiment, we know that imperfect diamond tool profile will cause great influences to the finished grating profile and step height. As a result, in order to avoid any unwanted loss of grating profile due to the imperfect diamond tool, we purposely tilt the 30 um half radius tool counterclockwise by a few degrees. Figure 5.25 shows the measurement results of the circular blazed gratings generated by the proposed tool path, and the tool path from NanoCAM2D, respectively. From Figure 5.25(a), we can observe the overcut into the grating profiles, and the resulting step height is 1.292 um, which matches very well with the designed value, 1.2935 um. On the other hand, in Figure 5.25(b), the step height is measured to be 1.124 um. The loss of step height is mainly due to the tool path generated by NanoCAM2D, where the diamond tool undercuts the grating profiles.

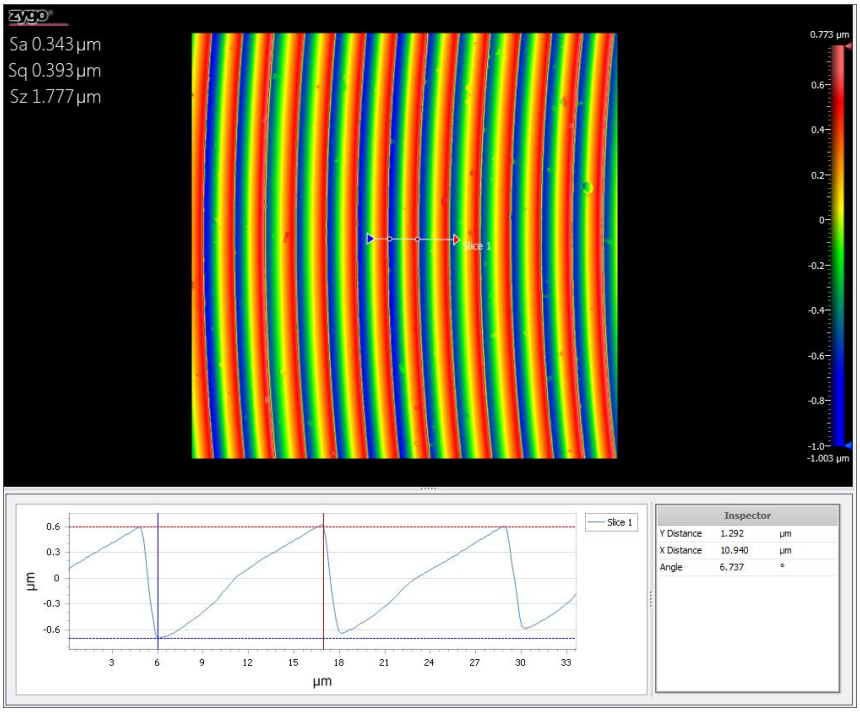

(a)

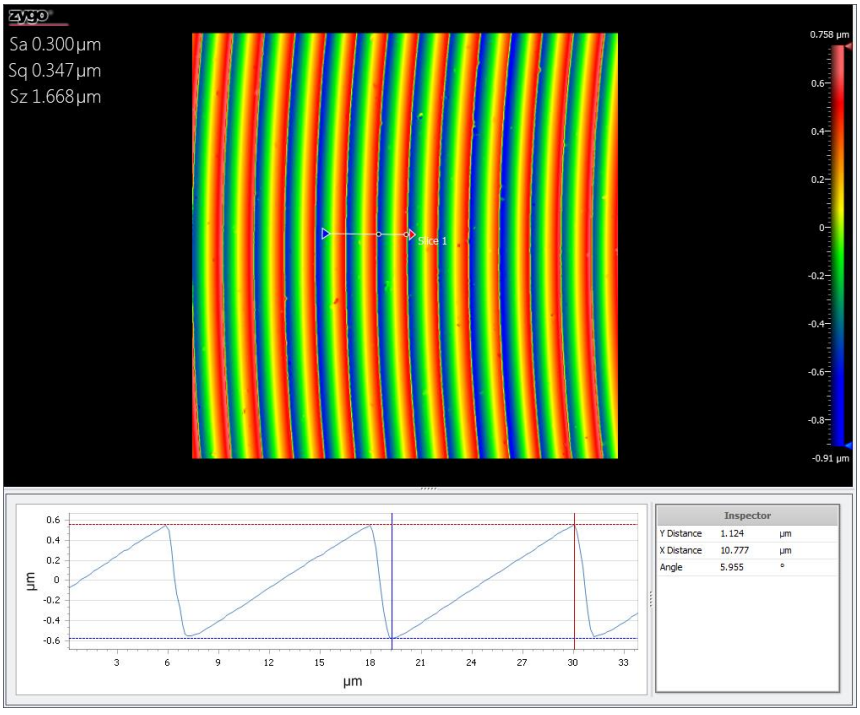

(b)

Figure 5.25 Measured blazed grating profiles generated by (a) the proposed tool path, and (b) tool path from NanoCAM2D. The half radius diamond tool is tilted counterclockwise in both cases.

With the two circular blazed gratings, we can set up a system to test the grating performance. Figure 5.26 shows the experimental setup for the measurement, and Figure 5.27 shows the measurement results for the circular blazed grating generated by the proposed tool path, and the tool path generated by NanoCAM2D, respectively. As a comparison, Figure 5.28 provides the beam profile of the measurement results. In Figure 5.27(a) and Figure 5.28(a), we can clearly observe the strong first order diffraction as well as a very weak zero order diffraction and second order diffraction. This matches very well with the simulation result shown in Figure 5.15(d), where a strong peak at first order and a very weak zero order and second order diffractions are presented. On the other hand, Figure 5.27(b) and Figure 5.28(b) show only a strong peak at the first order diffraction. This again matches very well with the simulation result shown in Figure 5.17(d). As a conclusion of the experimental results in Part II, we find that the grating performance as well as the diffraction efficiency are better for the gratings generated by the tool path that undercuts the grating profile. Although this will cause a loss in step height, the loss is negligible if the diamond tool radius is small enough. On the contrary, the gratings generated by the tool path that overcuts the grating profiles tend to induce different diffraction orders other than the first order diffraction.

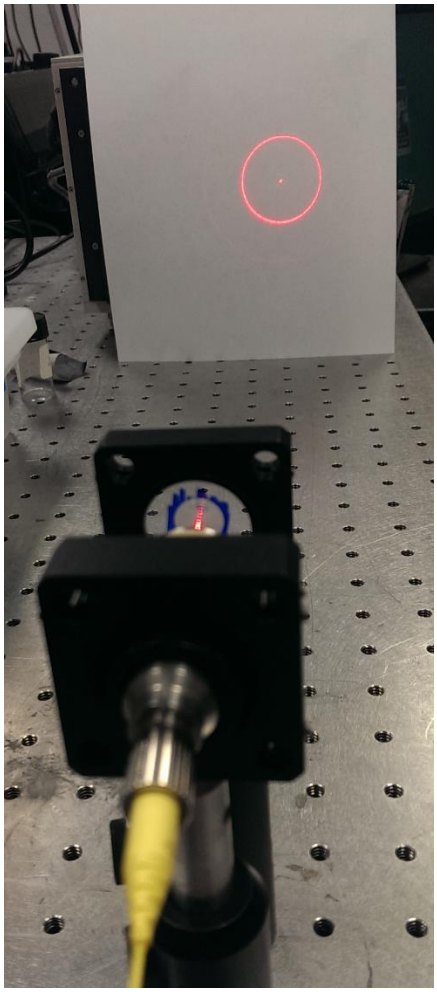

Figure 5.26 Experimental setup for measuring the grating performance.

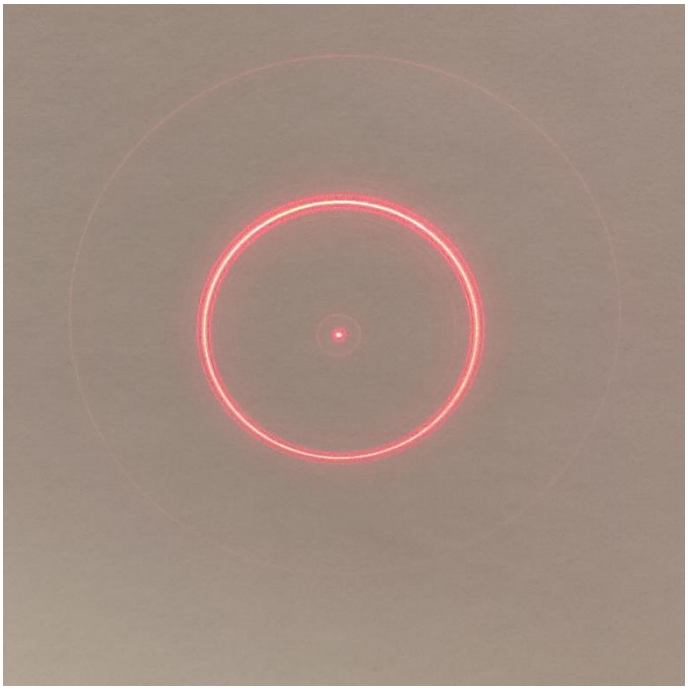

(a)

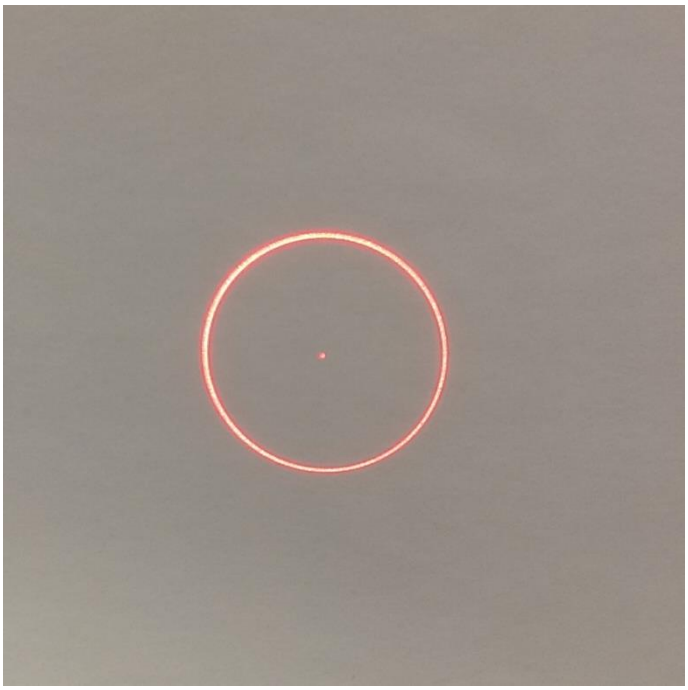

(b)

Figure 5.27 Measurement results for the circular blazed grating generated by (a) the proposed tool path, and (b) the tool path generated by NanoCAM2D.

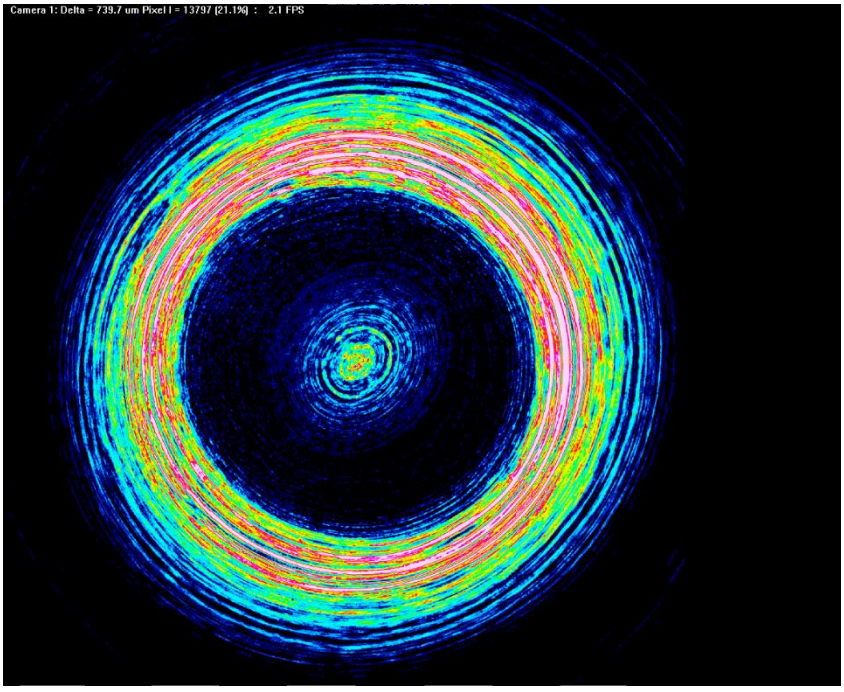

(a)

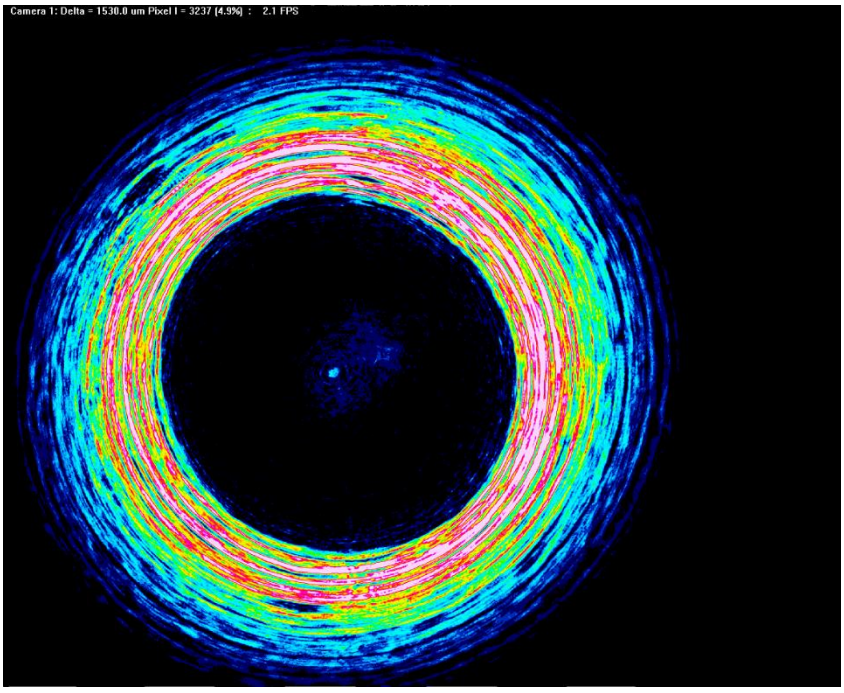

(b)

Figure 5.28 Beam profile of the measured circular blazed grating generated by (a) the proposed tool path, and (b) the tool path generated by NanoCAM2D.

5.5 Conclusion

In this chapter, we present a detailed analysis about the tool path generation, fabrication process, and the modeling of the diamond turned circular blazed gratings. Due to the slope discontinuity and the finite radius of the diamond tool, the tool path generated by NanoCAM2D tends to undercut the blazed grating and create incorrect step height. With the proposed tool path generation method, the correct step height is maintained, but with the cost of overcutting the grating profile. A model on the diamond turned blazed grating profile is developed with the consideration of different fabrication methods, basic cutting parameters, and diamond tool tilt in both the clockwise and counterclockwise directions. We provide a thorough discussion about the formation of the grating profile with respect to the diamond tool orientation. The diffraction efficiency calculation with respect to diamond tool tilt is then presented. From the simulation results, we conclude that the grating profile as well as the diffraction efficiency are only slightly influenced when the diamond tool is tilted counterclockwise. This is mainly due to the self-compensation of the grating profile and step height. However, the grating profile and diffraction efficiency are greatly influenced when the diamond tool is tilted clockwise. Finally, we conduct a series of experiments to verify the model we proposed. The measured grating profiles with the consideration of different fabrication methods and tool orientations match well with the model. However, due to the imperfect tool profile from the actual half radius diamond tool, we tend to get a smaller step height because of the extra removal of the grating profile by the extra tool profile. This issue can be effectively resolved by tilting the diamond tool counterclockwise by a few degrees.

CHAPTER 6 CONCLUSION AND FUTURE WORK

This dissertation provides a comprehensive discussion about the diamond turning fabrication method, modeling of the surface topography on the diamond turned flat and freeform surfaces, new design and fabrication techniques for the self-aligned and self-assembled optical systems, and finally, the analysis of the tool path generation, fabrication process, and performance modeling of the diamond turned circular blazed gratings.

We have proposed a model to simulate the surface topography of the diamond turned flat surfaces. By the consideration of the relative tool-workpiece vibrations in the feeding and infeed directions, this model provides a simulation of the surface roughness that matches well with the experiment results. We can gain useful information from the model in that it suggests the best combination of the basic cutting parameters that results in the smallest surface roughness. This can save a lot of time and money and avoid doing trial and error cutting tests before the actual diamond turning fabrication process.

The model is then extended to describe more general diamond turned spherical and freeform surfaces. It takes into consideration the local slope of the workpiece and the corresponding portions of the diamond tool that cuts the workpiece perpendicularly. Besides, the model also considers multiple dominant relative vibration components between the diamond tool and the workpiece. This can help us acquire a more realistic and accurate model and avoid creating periodic patterns that does not belong to the actual diamond-turned surface. We also show how the diamond tool waviness can be included into the model and how it will influence the surface profile. In future work, we will further extend this current model to describe not only surface roughness but also surface form accuracy provided that we have the information of the actual diamond tool weaviness profile. We observe a great match of the simulated surface topography and the measured result of

the actual diamond turned spherical surfaces on a high precision copper stud. Due to other environmental factors such as thermal variation, air nozzle direction, and cutting fluid that start to dominate the surface topography when the feed rate becomes too slow, we suggest adding a linear term to the current model to compensate for the influences. This linear compensation method can be further verified and improved by conducting a series of face cutting experiments with low feed rate while systematically changing the environmental influences.

In CHAPTER 4, we propose a new technique by integrating mechanical mounts onto the lens element to achieve a compact, lightweight, low cost, easy to assemble system that has high imaging quality. With the integration of the mechanical mounts onto the lens element outside of the clear aperture, the optical system can be assembled by simply clipping each lens into another. As a proof of concept, we designed an ultra-compact endoscope and a microscope objective that adopt this technique. We have also developed and demonstrated a new fixture design that has an extra ring at the outer edge for indication purpose to help to minimize lens decenter during the diamond turning process. Besides, we utilize interferometry to aid in correcting tilt between the two surfaces of the lens element. By observing the interference fringes between the fixture flat surface and the flat portion of the lens surface and trying to null the interference fringes, we are able to minimize the tilt between the lens surfaces. Finally, we show the preliminary assembly and testing results of the two systems and conclude that the technique we proposed is promising in getting a self-aligned and self-assembled lens system with high imaging quality. However, there are stray light issues for both systems that need further analysis. The stray light is mainly due to the multiple reflections and refractions inside the integrated mechanical mounts that are not properly processed for stray light reduction. It is necessary to do a thorough stray light analysis that helps identify the main source of the stray light. Then we would need to find a method to block them. This can be done by either

applying a blackening coating such as permanent marker or black ink outside of the lens clear aperture, or we can re-design the mechanical mounts and find a best structure that can minimize stray light.

Finally, in CHAPTER 5, we provide a thorough discussion and comparison of the two fabrication methods of the circular blazed gratings. The tool path generated by commercial software tends to undercut the grating with an incorrect step height, but with correct grating profile. On the other hand, we propose a tool path that can generate the correct step height of the grating, but with the cost of overcutting the grating profile. In addition to the two fabrication methods, we also consider the diamond tool orientation during the fabrication process. This can be divided into three cases, that is, tool without tilt, tool tilted clockwise, and tool tilted counterclockwise. A model to simulate the diamond turned circular blazed gratings is proposed. It provides us with a detailed grating profile which is used to calculate diffraction efficiency. From the simulation results, we conclude that the grating profile as well as the diffraction efficiency are only slightly influenced when the diamond tool is tilted counterclockwise. This is mainly because of the self-compensation of the grating profile and step height. However, the grating profile and diffraction efficiency are greatly influenced when the diamond tool is tilted clockwise. The model suggests an optimal fabrication method for blazed gratings with highest diffraction efficiency. Finally, we conduct a series of experiments to verify the model we proposed. The measured grating profiles with the consideration of different fabrication methods and tool orientations match well with the model.

REFERENCES

[1] N. Ikawa, R. R. Donaldson, R. Komanduri, W. König, T.H. Aachen, P. A. McKeown, T. Moriwaki, and I. F. Stowers, "Ultraprecision metal cutting — the past, the present and the future," CIRP Ann. Manuf. Techn. **40,** 587-594 (1991)

[2] Moore Nanotechnology Systems (http://www.nanotechsys.com)

[3] Z. Feng, B. D. Froese, C. Huang, D. Ma, and R. Liang, "Creating unconventional geometric beams with large depth of field using double freeform-surface optics," Appl. Opt. **54,** 6277-6281 (2015)

[4] R. Katkam, B. Banerjee, C. Y. Huang, X. Zhu, L. Ocampo, J. Kincade and R. Liang, "Compact dual-view endoscope without field obscuration," J. Biomed. Opt. **20**, 7 (2015)

[5] E. L. Church, and J. M. Zavada, "Residual surface roughness of diamond-turned optics," Appl. Opt. **14,** 1788-1795 (1975)

[6] L. Li, S. A. Collins, and A. Y. Yi, "Optical effects of surface finish by ultraprecision single point diamond machining," J. Manuf. Sci. Eng. **132** (2010)

[7] J. M. Tamkin, and T. D. Milster, "Effects of structured mid-spatial frequency surface errors on image performance," Appl. Opt. **49,** 6522-6536 (2010)

[8] R. J. Noll, "Effect of mid- and high-spatial frequencies on optical performance," Opt. Eng. **18,** 137-142 (1979)

[9] J. C. Stover, "Roughness characterization of smooth machined surfaces by light scattering," Appl. Opt. **14,** 1796-1802 (1975)

[10] D. J. Whitehouse, "Handbook of surface metrology," Institute of Physics Publishing, Bristol, UK (1994)

[11] B. Abouelatta, and J. Mádl, "Surface roughness prediction based on cutting parameters and tool vibrations in turning operations," J. Mater. Process. Tech. **118,** 269-277 (2001)

[12] C. F. Cheung, W. B. Lee, "A theoretical and experimental investigation of surface roughness formation in ultra-precision diamond turning," Int. J. Mach. Tool. Manu. **40,** 979-1002 (2000)

[13] C. F. Cheung and W. B. Lee, "Surface generation in ultra-precision diamond turning: modelling and practices," Professional Engineering Publishing, Wiltshire, UK (2003)

[14] H. Wang, S. To, C. Y. Chan, C. F. Cheung, W. B. Lee, "A theoretical and experimental investigation of the tool-tip vibration and its influence upon surface generation in single-point diamond turning," Int. J. Mach. Tool. Manu. **50,** 241-252 (2010)

[15] S. Takasu, M. Masuda, T. Nishiguchi, and A. Kobayashi, "Influence of study vibration with small amplitude upon surface roughness in diamond machining," CIRP Ann. Manuf. Techn. **34,** 463-467 (1985)

[16] K. A. Risbood, U. S. Dixit, and A. D. Sahasrabudhe, "Prediction of surface roughness and dimensional deviation by measuring cutting forces and vibrations in turning process," J. Mater. Process. Tech. **132,** 203-214 (2003)

[17] S. C. Lin, and M. F. Chang, "A study on the effects of vibrations on the surface finish using a surface topography simulation model for turning," Int. J. Mach. Tool. Manu. **38,** 763-782 (1998)

[18] P. G. Benardos, and G.-C. Vosniakos, "Predicting surface roughness in machining: a review," Int. J. Mach. Tool. Manu. **43,** 833-844 (2003)

[19] A. Mital, and M. Mehta, "Surface finish prediction models for fine turning," Int. J. Prod. Res. **26,** 1861-1876 (1988)

[20] C. F. Cheung, and W. B. Lee, "Study of factors affecting the surface quality in ultra-precision diamond turning," Mater. Manuf. Process. **15,** 481-502 (2000)

[21] C. Huang, and R. Liang, "Modeling of surface topography in single-point diamond turning machine," Appl. Opt. **54,** 6979-6985 (2015)

[22] E. Paul, C. J. Evans, A. Mangamelli, M. L. McGlauflin, and R. S. Polvani, "Chemical aspects of tool wear in single point diamond turning," Precis. Eng. **18,** 4-19 (1996)

[23] M. Seeman, G. Ganesan, R. Karthikeyan, and A. Velayudham, "Study on tool wear and surface roughness in machining of particulate aluminum metal matrix composite-response surface methodology approach," Int. J. Adv. Manuf. Tech. **48,** 613-624 (2010)

[24] D. P. Yu, S. W. Gan, Y. S. Wong, G. S. Hong, M Rahman, and J. Yao, "Optimized tool path generation for fast tool servo diamond turning of micro-structured surfaces," Int. J. Adv. Manuf. Tech. **63,** 1137-1152 (2012)

[25] C. Huang, L. Li and A. Y. Yi, "Design and fabrication of a micro Alvarez lens array with a variable focal length," Microsyst Technol. **15**, 4 (2009)

[26] S. To, T. C. Kwok, C. F. Cheung and W. B. Lee, "Study of ultra-precision diamond turning of a microlens array with a fast tool servo system," Proc. SPIE 6149 (2006)

[27] H. Kim, K. Lee, K. Lee and Y. Bang, "Fabrication of free-form surfaces using a long-stroke fast tool servo and corrective figuring with on-machine measurement," Int. J. Mach. Tools Manuf **49**, 12 (2009)

[28] L. Li and A. Y. Yi, "Design and fabrication of a freeform microlens array for a compact large-field-of-view compound-eye camera," Appl. Opt. **51**, 12 (2012)

[29] Z. Q. Yin, Y. F. Dai, S. Y. Li, C. L. Guan and G. P. Tie, "Fabrication of off-axis aspheric surfaces using a slow tool servo," Int. J. Mach. Tools Manuf **51**, 5 (2011)

[30] L. Li, A. Y. Yi, C. Huang, D. A. Grewell, A. Benatar and Y. Chen, "Fabrication of diffractive optics by use of slow tool servo diamond turning process," Opt. Eng. **45**, 11 (2006)

[31] M. Kyrish, J. Dobbs, S. Jain, X. Wang, D. Yu, R. Richards-Kortum and T. S. Tkaczyk, " Needle-based fluorescence endomicroscopy via structured illumination with a plastic, achromatic objective" J. Biomed. Opt. **18**, 9 (2013)

[32] R. T. Kester, T. Christenson, R. R. Kortum and T. S. Tkaczyk, "Low cost, high performance, self-aligning miniature optical systems," Appl. Opt. **48**, 18 (2009)

[33] F. C. Wippermann, E. Beckert, P. Dannberg, R. Eberhardt, A. Bräuer and B. Messerschmidt, "Low cost video endoscopes with simplified integration," Proc. SPIE 7716 (2010)

[34] http://www.ogc.co.jp/e/products/fluorene/okp.html

[35] E. P. Goodwin and J. C. Wyant, Field Guide to Interferometric Optical Testing (SPIE Press, 2006)

[36] R. G. Jasinevicius, J. G. Duduch, G. A. Cirino, and P. S. Pizani, "Diamond turning of small Fresnel lens array in single crystal InSb, " J. Micromech. Microeng. **23** (2013)

[37] J. Yan, K. Maekawa, J. Tamaki, and T. Kuriyagawa, "Micro grooving on single-crystal germanium for infrared Fresnel lenses, " J. Micromech. Microeng. **15** (2005)

[38] Y. Takeuchi, S. Maeda, T. Kawai, and K. Sawada, "Manufacture of Multiple-focus Micro Fresnel Lenses by Means of Nonrotational Diamond Grooving," Manufacturing Technology **51**, 1 (2002)

[39] M. A. Davies, B. S. Dutterer, T. J. Suleski, J. F. Silny, and E. D. Kim, "Diamond machining of diffraction gratings for imaging spectrometers, " Precis. Eng. **36,** 2 (2012)